QATAR UNIVERSITY

COLLEGE OF ENGINEERING

HIGH-POWER ISOLATED MODULAR DC-DC CONVERTER SYSTEM FOR HEAVY-DUTY FUEL-CELL-BASED ELECTRIC VEHICLES

BY

WALID MAHMOUD AHMED ABOUEATA

A Thesis Submitted to
the College of Engineering
in Partial Fulfillment of the Requirements for the Degree of
Masters of Science in Electrical Engineering

January 2022

COMMITTEE PAGE

The members of the Committee approve the Thesis of
Walid Mahamoud Ahmed Aboueata defended on 22/11/2021.

Prof. Ahmed Massoud
Thesis/Dissertation Supervisor

Dr. Sinan AlObaidi
Thesis/Dissertation Co-Supervisor

Prof. Lazhar Ben Brahim
Committee Member

Prof. Haitham Abu-Rub
Committee Member

Dr. Mohammed Elshafie
Committee Member

Approved:

Khalid Kamal Naji, Dean, College of Engineering

ABSTRACT

ABOUEATA, WALID M., Masters : January : 2022,

Masters of Science in Electrical Engineering

Title: High-Power Isolated Modular DC-DC Converter System for Heavy-Duty Fuel-Cell-Based Electric Vehicles

Supervisor of Thesis: Prof.Ahmed Massoud.

Electric Vehicles (EVs) have attracted researchers' attention to further develop and enhance this strategic area. Compared with fuel-based vehicles, EVs are more demanded nowadays due to their high performance and new modern features. Integrating renewable energy sources such as PV and fuel cells (FCs) to EVs expand this technology's research area to increase system reliability. In addition, it enables an on-board charging feature, which can extend the mileage range of EVs. FC electric vehicles (FCEVs) introduce more challenges to the researchers to integrate this type of renewable energy source to charge the EV battery while driving. This work addresses and evaluates an isolated DC-DC converter for FCEV, where a high-power modular power converter is developed for such applications. Since the FC produces a relatively low voltage, a high gain DC-DC converter is required to step up the voltage to meet the battery's rated voltage. This is achieved through an input-parallel output-series Cuk-based DC-DC converter. The system's small-signal model is obtained to implement battery charger control using the constant current control method. Furthermore, equal power-sharing between the converters through power balancing control is presented to ensure equal current sharing at the input side and maintain equal output voltage with a mismatch in the system modules. Fractional-order PI (FOPI) controllers are utilized to further enhance the system and overcome the drawbacks of conventional PI controllers.

Then, the proposed topology was examined through different performance indices such as gain, efficiency, power density, sensitivity, and FC current ripple content analysis. The presented concept has been elucidated through simulation using Matlab/Simulink platform.

DEDICATION

This thesis is dedicated to my parents, siblings, and who continuously prayed for my success.

ACKNOWLEDGMENTS

Special thanks to my family and friends for their continuous support throughout my masters' journey. Sincere gratitude to my supervisors Prof. Ahmed Massoud and Dr. Sinan AlObaidi, for their continuous support, patients, guidance, and being always there to support.

Also, I would like to thank the Departments of Electrical Engineering and General Engineering for providing me with the technical knowledge required to achieve this success and for their continuous help.

This thesis was made possible by Graduate Sponsorship Research Award (GSRA) GSRA6-2-0523-19039, from the Qatar National Research Fund (a member of Qatar Foundation).

TABLE OF CONTENTS

LIST OF TABLES

LIST OF FIGURES

CHAPTER 1: INTRODUCTION

1.1 Background

Fuel Cells (FCs) are considered one of the most efficient and clean power sources. The FC produces potential energy from an electrochemical reaction between hydrogen and oxygen; however, the observed potential is low. Therefore, a stack of FCs is used as a power source. By cascading multiple cells, higher potential can be obtained [1]. In addition, water is produced as a by-product of this chemical reaction. The hydrogen used in the FC is available everywhere and can be produced using different methods (e.g., electrolysis, biomass gasification, photo-biological processes, etc.).

There are several reasons to use FCs compared to conventional power sources. FCs are considered one of the most efficient power sources. Also, the power produced by the FC is generated without causing any noise or any other mechanical disturbance such as vibration and CO2 emissions like the conventional combustion engine [2]. This helps eliminate greenhouse gas emissions, and hence, it is considered ultra-low/zero emissions fuels [3]. Moreover, the FC enhances the energy security for the user nation. Some studies show that the FC's amount of energy per weight produced is 2.8 times greater than the energy per weight produced by gasoline, and the energy per volume produced via FC is four times less than gasoline [1]. Furthermore, hydrogen fuel properties add an advantage to FCs since it can be stored as gas or liquid, which helps in the refueling process. The result of the chemical reaction done in the FC can be used in other processes, or it can be reused to produce hydrogen fuel again.

The global FC market was valued at USD 4.1 billion in 2020, and it is expected to further increase at an annual growth rate of 23.2% from 2020 to 2028. The increase of unconventional energy sources is a key factor driving the FC market growth [4]. Also, governments worldwide are supplementing the development of FC by funding different research activities. As a matter of fact, the global industry has experienced growth in the FC market since 2010. The following figure shows the exponential revenue growth of the FC market between 2016 and 2020 [5]:

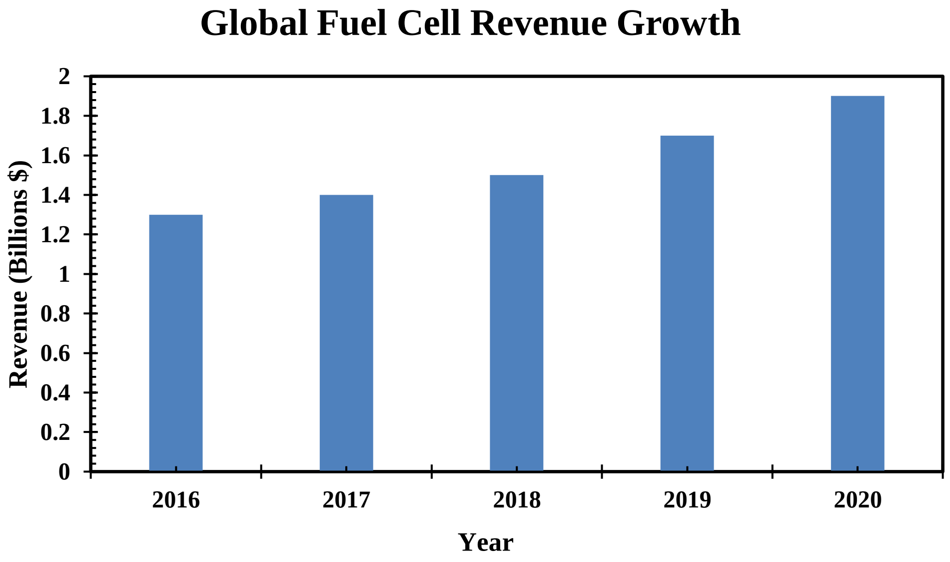

Figure 1: Global Fuel cell industry growth

Many applications deploy FCs as a power source. One of the typical applications is FCs in EVs. The fuel cell-based electric vehicle (FCEV) is a purely electrical engine composed of the power control unit, electric motor, and compressor. The main advantages of the FCEV compared to the hybrid vehicle are that it can sustain longer distances, and the hydrogen refueling time is shorter than the charging time in EVs [6]. The FCEV structure replaces the gasoline tanks with hydrogen tanks compared to the conventional combustion vehicles. The tanks' location is based on the vehicle type, whether light-duty, medium-duty, or heavy-duty. The vehicles are classified based on their gross weight, where vehicles below 3800 kg are considered light-duty, vehicles between 3800 kg and 4500 kg are medium-duty, and vehicles above 4500 kg are heavy-duty. In buses and trucks, the hydrogen storage is usually located at the enclosure of the bus roof, and for the passenger vehicles, the tanks are located instead of gasoline tanks. Figure 2 clearly shows the structure of FCEV for light-duty vehicles and heavy-duty vehicles.

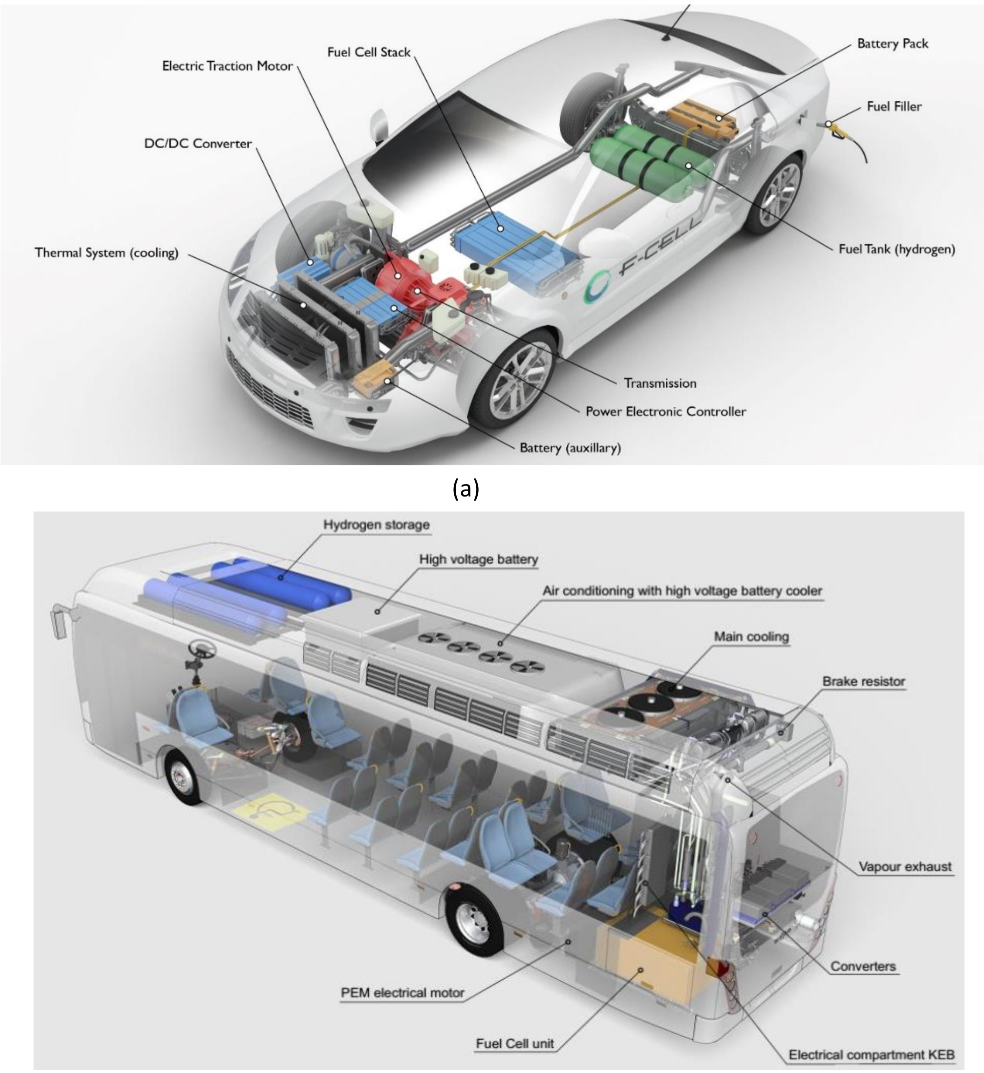

(a)

(b)

Figure 2: FCEV structure (a) light-duty vehicles (passenger cars), (b) heavy-duty vehicles (buses) [7],[8]

Figure 3 shows the projection study done by BMW of how the FCEV production in Europe will increase in 2050 [9]. Several architectures are used in FCEVs. For example, some applications utilize FC as the main power supply to drive the train directly [10]. On the other hand, other applications are using the FC as a secondary power supply in conjunction with batteries to extend the mileage of the EVs [11]. The direct FC connection architecture is commonly used in normal vehicles with a limited range. However, the second architecture is commonly used in vehicles that require high power, and they are considered heavy-duty EVs such as buses and military trucks [1].

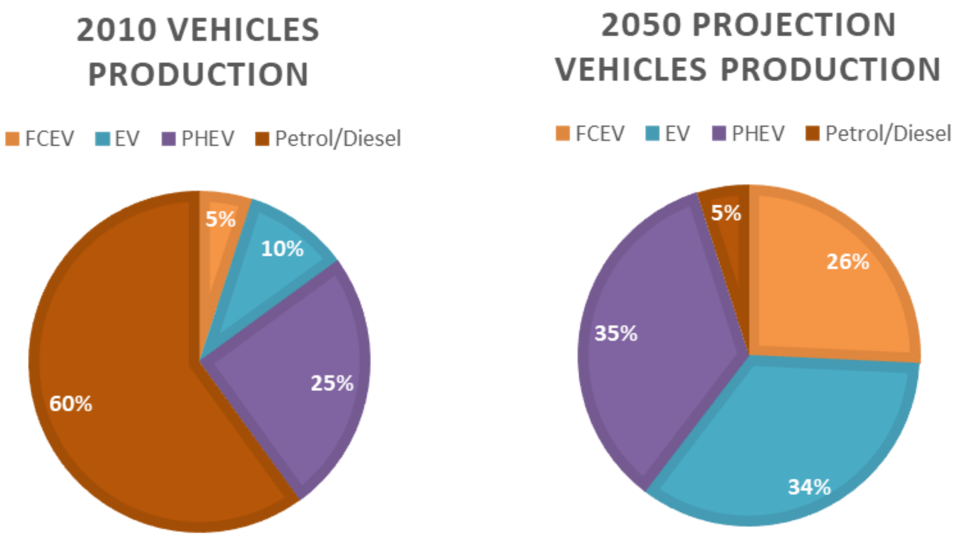

Figure 3: BMW vehicles production projection by 2050

The largest challenge of FCEV is the lack of hydrogen infrastructure. However, there are more than 150 hydrogen refueling stations around the world. Figure 4 shows the number of hydrogen stations around the world.

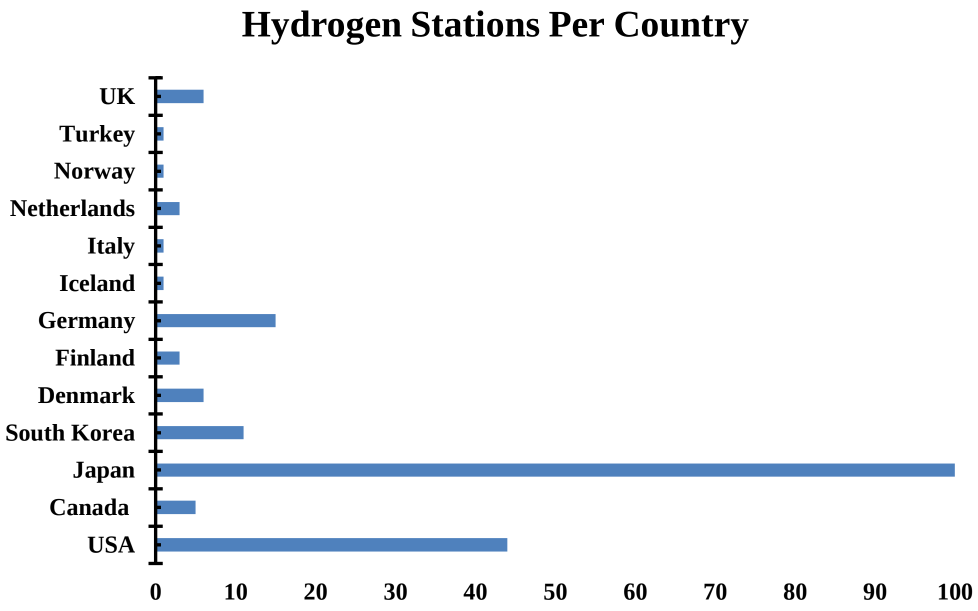

Figure 4: Hydrogen Stations in each country in 2020 [12]

Until 2020 Japan leads the countries with 100 stations distributed in the country, followed by the USA with 44 stations in different states [12]. Hydrogen produced from natural gas can be cheaper than conventional gasoline. Moreover, since Qatar is one of the top countries that produce natural gas, hydrogen production does not represent a challenge for such application.

The output power of a single FC is low, where the nominal voltage of a single cell is 0.7V and power of ~ 50W[13]. Therefore, a multi-stack FC technique is used to overcome this issue and increase FC power by cascading multiple FCs. The architecture of the multi-stack FC can improve efficiency, enhance reliability, and reduce cost [14]. Although the discovery of the FC was 150 years back, the multi-stack FC is still recent [15]. Several architectures can be made to build a multi-stack system. For example, the FC can be cascaded in parallel, series, or a combination of series-parallel connections. In series connection, more power is produced to reduce the hydrogen fuel [14]. However, high power can be obtained from the parallel connection with more hydrogen fuel consumption [16]. From an electrical point of view, in a series connection, the voltage of cascade FCs is summed up where higher voltage can be achieved with a lower current. On the other hand, the parallel connection ensures a higher amount of current with a lower voltage, making the design of the DC-DC converter challenging to achieve higher gains [17].

FC systems can be constructed in different chemical reactions, and they vary based on their operating temperature, efficiency, cost, and application [18]. Depending on the fuel and electrolyte, the FC is classified into 6 major groups, alkaline FC (AFC), phosphoric acid FC (PAFC), solid oxide FC (SOFC), molten carbonate FC, proton exchange membrane FC (PEMFC), and direct methanol FC (DMFC). Table 1.1 illustrates the difference between those types of FCs.

Table 1.1: FC types comparison [18]

FC Type	Operating Temperature (C)	Output Power (kW)	Electrical Efficiency (%)	Application
AFC	90-100	<100	60	Military Space
PAFC	150-200	<1000	>40	Distributed generation
SOFC	600-1000	<3000	35-43	Electric utility
MCFC	600-700	<1000	45-47	Electric utility
PEMFC	50-100	<250	53-58	Backup power Portable power
DEMFC	60-200	<100	40	Portable devices

The Proton Exchange Membrane (PEM) FC is commonly used in EV applications due to its high power ratings that can run such applications. Since the FC equivalent circuit values vary based on the chemical reactions, this model is used to obtain the Voltage-Current characteristic. The V-I characteristic of the PEMFC operates at a temperature of $65C^o$ with a stack efficiency of 55% that produces 430V and 280A at maximum operating point is shown in the following figure:

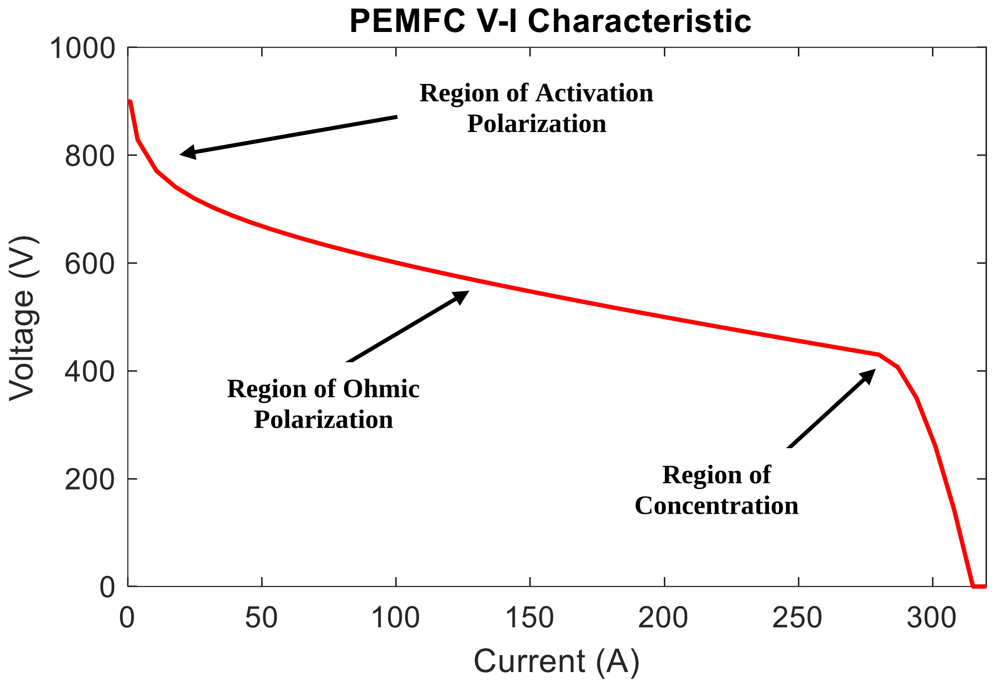

Figure 5.V-I Characteristic of PEMFC

As illustrated in Figure 5, the FC has a nonlinear V-I characteristic. Hence, to achieve the required amount of power, power electronics should be used with FC technology [19]. A power control unit is used to generate the desired load voltage level. Based on previous studies and designs developed for FC applications, some converters can provide a wide voltage gain but with some drawbacks. In FCEV, some necessary points need to be pinned. These points are FC power variation, dynamic load, and energy management systems. Several reasons cause the output power of the FC to vary [20]. Knowing that the FC is a multi-physics system, consequently, the degradation and physical fluctuation will affect the performance of the FC. In addition, the operating conditions (temperature, humidity, gas stoichiometry, pressure) have a significant impact on FC power output [21]. Therefore, an energy storage system needs to be integrated with the FC, such as a battery or ultracapacitor, to compensate for load variations. The stored energy plays an essential role in different scenarios. For example, when the electric motor requires more power, this storage could provide this power to the load [22]. Also, while decelerating, the electric energy can be stored in the batteries to ensure no wasted energy and enhance the system efficiency [21].

1.2 Problem Statement

In typical EVs, the power is mainly taken from the batteries to run the drive train and other systems such as cooling units or any other electrical entertainment devices. However, in gulf countries, especially in summer, cooling systems consume more power to cool down the vehicle and keep the vehicle temperature within the operable limits. This drains the battery and reduces the mileage range of the EV. Therefore, an external power supply can be integrated with the system to compensate for the power consumed in the cooling system to increase the EV's mileage range. FCs are one of the recommended power supplies due to the advantage of the hydrogen refueling option using liquid hydrogen stored in small hydrogen cylinders within the vehicle. Moreover, the by-product of the FC is water, where it can be used in the cooling system, which helps reduce the amount of electric power consumed in running a fan to cool down the EV.

FC power supplies can be used in military applications where the by-product can be used to provide drinking water for the soldiers and the vehicle cooling process. Furthermore, military electric trucks require high torque to move the track due to their high weight, increasing the rated power of the EV. Thus, adding an extra power supply to provide an on-board charging option to the battery will help extend the mileage range and operating hours in such applications. The on-board charging option should be designed to provide the maximum power of the FC to assure continuous battery charging to avoid power outages that can cause any system interruption and breakdown of the vehicle.

This thesis proposes the FC as an additional power supply to the EV to provide the on-board charging for the vehicle. The proposed system integrates the FC power supply with a battery connected through a power conditioning unit that extracts the maximum power of the FC to charge the battery while driving to avoid system interruption. Moreover, due to high power conversion through the power conditioning unit, a modular design reduces the voltage and current stresses by connecting several modules to share the power between the modules and provide ride-through capability if one or more power modules are faulty. The primary objective is to use a proper connection compatible with FC specifications to ensure smooth battery charging, considering FC requirements such as ripple current, low output voltage, and maximum power extraction.

1.3 Thesis Objectives

This thesis aims to integrate the FC power supply to provide on-board charging for the battery through a modular DC-DC power conversion unit using isolated converter topology. This can be achieved through the following objectives:

1- Conduct an extensive literature review on FCEVs application to identify the gaps.

2- Compare different converters topologies that have been used in FCEV applications.

3- Develop multi-module connections that fulfill FC requirements.

4- Model the DC-DC converter using small-signal modeling to examine system behavior and provide proper control to the system.

5- Investigate different control techniques to ensure robust control of the system.

6- Assess the performance of the presented system.

This thesis focuses on the device level in FCEV, the power conditioning unit control, and design considered the main core of this study. The following diagram briefly describes the scope of the thesis in an FCEV system layout.

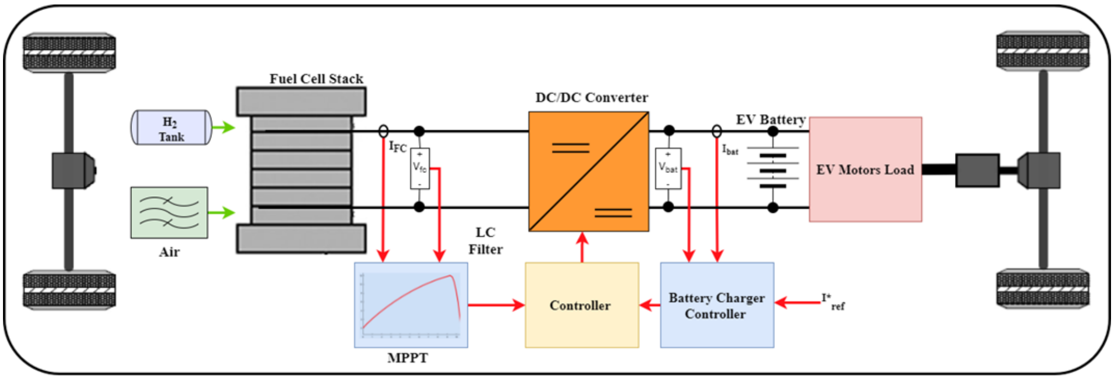

Figure 6. The typical configuration of fuel-cell based electric vehicle

1.4 Thesis Contribution

This thesis studies and evaluates an isolated DC-DC converter for FCEV and develops a modular power converter with maximum power point tracking for a constant-current battery charging controller. The modular converter is based on an isolated Cuk converter, using input-parallel output-series connection of *n*-converters to make the power conditioning stage modular and assure a high efficiency for the overall power conditioning system. The main contributions of this thesis are listed in the following points:

1- The modular converter is based on a Cuk converter, ensuring low input and output current ripple with reduced capacitances. Therefore, it will extend the lifetime of the power conditioning unit, making the system reliable by reducing the capacitance, which helps avoid electrolyte capacitors. In addition, the advantage of low input ripple current in the Cuk converter helps reduce FC temperature and increase the FC efficiency.

2- A multi-module topology makes the system modular by connecting several converters to increase the system's reliability. Furthermore, due to the FC's low output voltage, such a connection ensures enough gain to reach the battery voltage in driving mode. An FC in such an application requires a high input current with low voltage capability and high voltage at the battery side. Therefore, input-parallel output-series is preferred to achieve FC requirements. The isolated Cuk converter topology is used where a high-frequency transformer (HFT) is integrated into each converter. The ratings of the selected HFTs are reduced, reflecting the prices of the used HFTs compared to a single high power HFT, where the relation of HFT and its cost is not linear for with power rating increase.

3- Equal power-sharing among the connected converters is achieved by ensuring two main conditions in input-parallel output-series connection: input current sharing (ICS) and output voltage sharing (OVS). To do so, a feedback controller is used to achieve these conditions. A fractional PI controller is utilized in the control to increase the system stability and make it more reliable. The FOPI controller overcomes the drawbacks of the conventional PI by reducing the noise level with lower-order derivatives. It also makes the system robust against plant variations, considered one of the main concerns in such applications when there is any variation in internal converter parameters.

1.5 Thesis structure

The breakdown of the thesis chapters are presented as follows:

Chapter 1 briefly introduces a general background of the addressed topic, defining the problem statement, objectives and the main contributions, and the general outline.

Chapter 2 An extensive literature review is presented in this chapter. It explains different topologies of power modules used with FC power supplies. Isolated and non-isolated topologies are presented, highlighting the main constraints when they are integrated with FC power supplies. Afterward, high gain high power topology highlights each configuration and how they can be connected to meet the application requirement. Then different methods of MPPT that can be used in different applications are presented. According to the constraints defined by the previous authors related to the converter design and control, a proper selection of converter type and system configuration is made to meet the system requirements such as voltage level, input current, and power ratings.

Chapter 3 A mathematical model of isolated Cuk converter is presented using the small-signal modeling. The obtained model is used to analyze the system and design the controller, as well as the model is used in the assessment of the proposed topology. Parasitic resistances are considered in modeling the converter to obtain an accurate model.

Chapter 4 In this chapter, the overall system is simulated using Matlab/Simulink, and the simulation results are elucidated. Different control techniques are presented, such as voltage and current control, and the integration between such controls with MPPT is tested and presented. Furthermore, equal power-sharing is presented considering the converter's input current and output voltage. In addition, a comparison between the conventional PI and FOPI controllers is presented to show the advantage of using FOPI controllers. Also, Z-domain analysis is explored to show the effect of discretizing the system.

Chapter 5 shows performance assessment is described and presented in this chapter. Several performance indices are presented to assess the overall system, such as gain vs. duty cycle, system efficiency based on the output power and duty cycle, sensitivity analysis, and power density.

Chapter 6 presents the conclusion obtained from the previous chapters. Also, the work can be expanded for future work, explaining different ideas that can be integrated into the work to enhance the overall system.

The following figure shows the sequence diagrams to highlight thesis chapters.

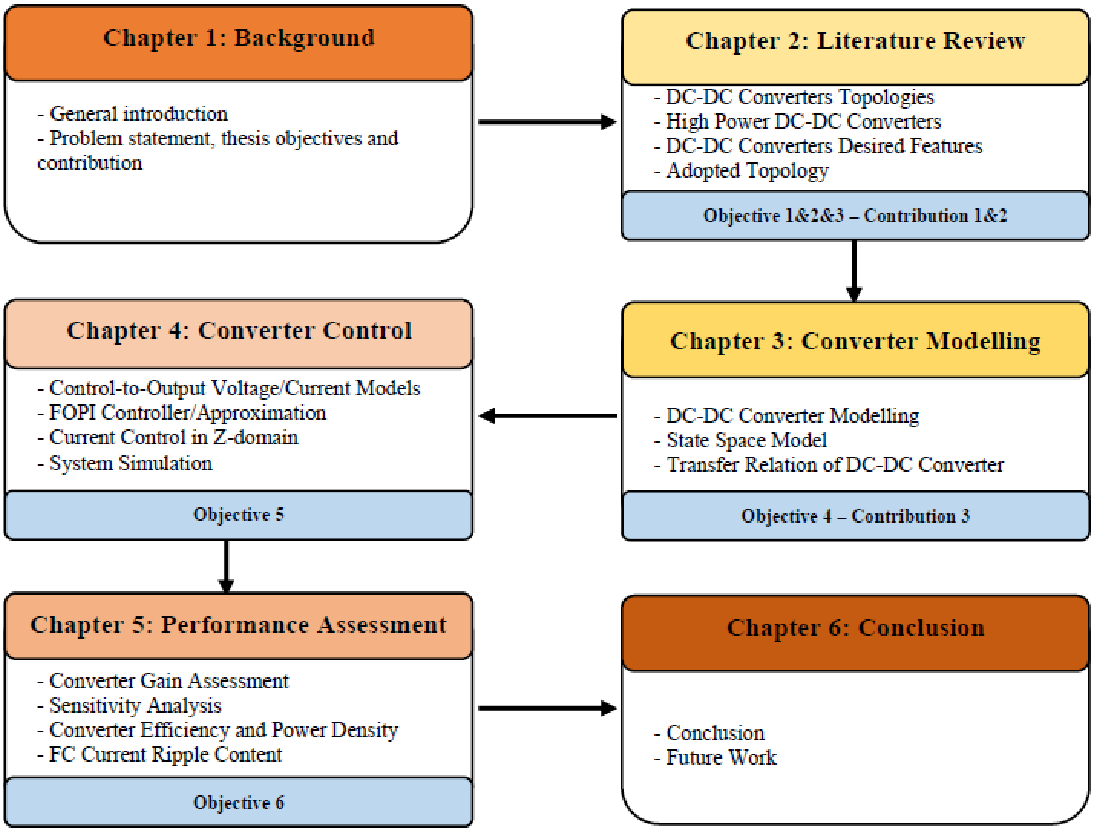

Figure 7. Thesis sequence diagram

Chapter 2: Literature Review

This chapter gives a detailed review of DC-DC converters used in EVs and FCEVs. Non-isolated DC-DC converters are presented, which are divided into two types conventional and high step-up converters. Also, the isolated converters are addressed considering bridge type and single switch type converters. Afterward, the high-power isolated and non-isolated converters consider different methods to achieve high-power capability.

2.1 DC-DC Converter for FCEV.

The power converter used in the FC application should handle the rated power of the FC. The FC current is high, while the FC voltage is relatively low [23]. Besides, the converter output voltage has to be controlled to manage charging the battery regardless of the FC voltage variations. One of the mandatory factors in selecting the power converter for such an application is to minimize the FC current ripple to extend the FC lifetime [24]. Accordingly, the power converter design should consider some specifications such as high efficiency, low input ripple current, modularity, and reliability. Literature on the FC DC-DC converter is presented in this part. Non-isolated and isolated converters for both high gain and low gain used for FCEVs are presented. Also, the techniques used to achieve high-gain high-power considering isolated and non-isolated topologies make the overall design reliable and efficient. Then by comparing the overall performance and efficiency, criteria will be established to select a suitable topology that meets thesis objectives.

2.2 Isolated and Non-Isolated DC-DC Converters.

The following figures show the overall system using non-isolated and isolated converters in FC-powered EVs.

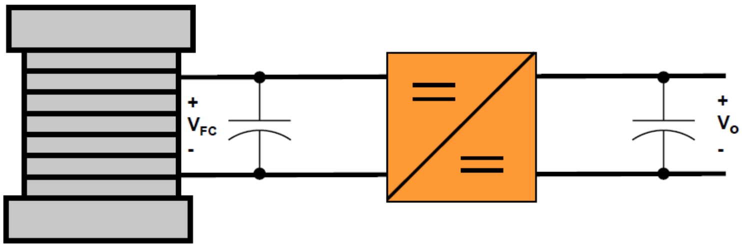

Figure 8. Non-isolated topology

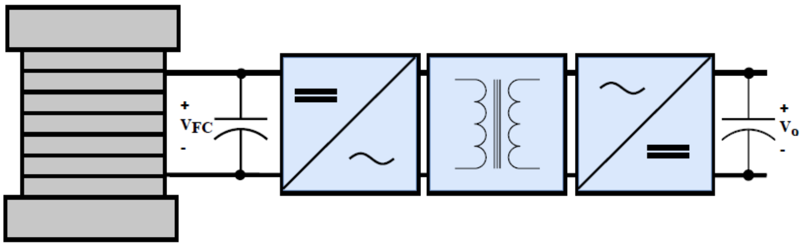

Figure 9. Isolated topology

DC-DC converters used to charge the EV batteries are divided into isolated and non-isolated converters [23]. Both types can be used in EVs since several technologies and innovations exist for EVs. The non-isolated converters are usually utilized in medium-power and high-power EVs [25]. Such converters can sustain high power with some limitations on frequency. However, isolated converters are commonly employed in medium power applications, and they are isolated using a high-frequency transformer. The following tree diagram shows the most common converters used in charging EV batteries:

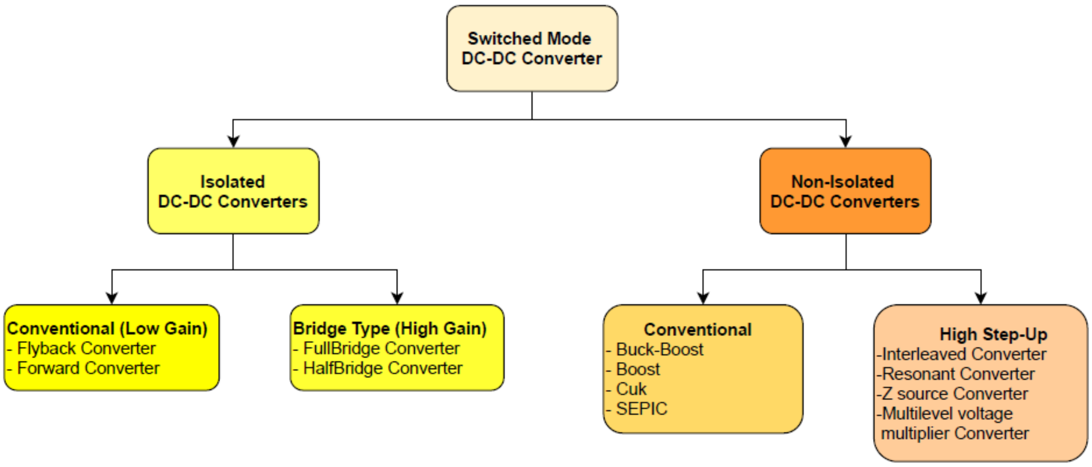

Figure 10:DC-DC converter classification

Figure 10 shows basic types of conventional non-isolated DC-DC converters in EVs. The modified interleaved converters of these basic converters are used in higher power applications to meet the high gain requirement. The isolated converters are derived from the conventional converters by integrating high-frequency transformers. These converters can operate in wide power ranges and provide the required galvanic isolation for high-power applications.

2.2.1 Non-Isolated Conventional DC-DC Converters.

Typical conventional DC-DC converters such as boost, buck-boost, Cuk, or single-ended primary inductor converter (SEPIC) shown in Figure 11 can fulfill the basic FCEV system’s requirements [26]. Such converters have high gain limitations due to the converter elements' parasitic resistances (inductor, capacitor, switches, and diodes) [27]. The main effect of these elements is significant when the converter operates at a high duty cycle to achieve high gain that results in higher losses, and the overall effect is a dramatic drop in the converter efficiency and a significant disturbance on the gains at high duty cycles [25]. Other methods, such as cascading converters, ensure high voltage gain in conventional DC-DC converters. Such converters are preferred in low-power FC applications where they are used in low-power modes.

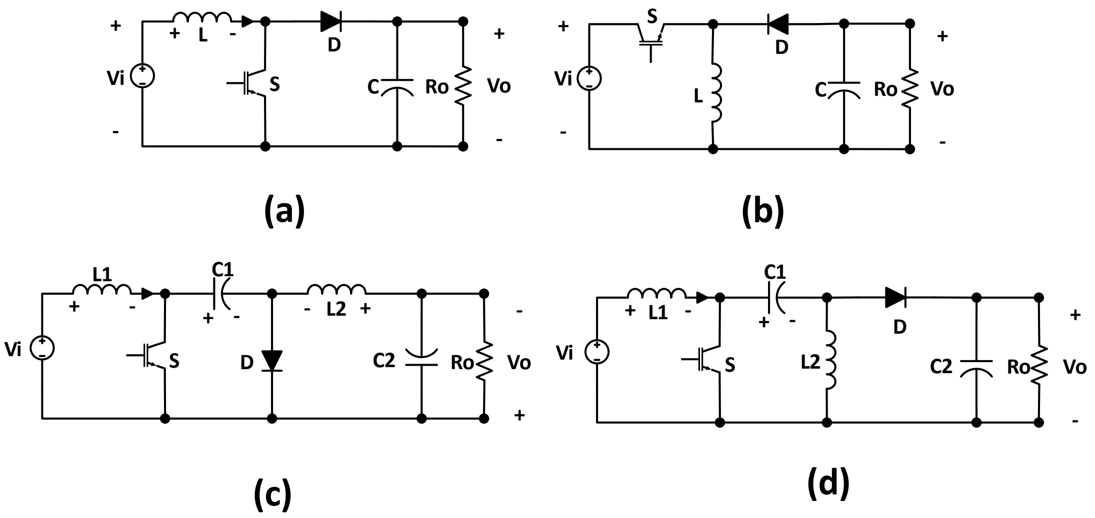

(a) (b) (c) (d)

Figure 11: Basic non-isolated DC-DC Converters (a) Boost converter, (b) Buck-Boost converter, (c) Cuk converter, (d) SEPIC converter.

2.2.2 Non-Isolated High Step-Up DC-DC Converters.

Compared to the conventional non-isolated converters, high step-up converters are utilized in high voltage DC HVDC applications. These converters are modified types of the front-end part of the conventional converters that assure the required high gain with higher efficiencies. The interleaved boost converter (IBC) shown in Figure 12 (c) is also commonly used in EVs since it has a high gain compared to the conventional boost converter [28]. The conventional boost converter research aims to increase the voltage gain through multi-level/stage techniques, switched inductors or capacitors, and coupled inductor converters [29]. However, most of the studies of the non-isolated converter select the IBC converters due to their high efficiency and low input current. In [30], a coupled inductor was used to achieve high gain, but the cost of this design was a high input ripple current as well as it requires a large capacitor at the output of the converter. Another study showed that the coupled-inductor with diode-capacitor converter increased the voltage gain, but this is at the expense of high voltage stress on the diodes [31]. One study presented an IBC design based on the conventional boost converter [28]. The converter showed a low input current and low switching losses. Nonetheless, the inductor needs to be well designed concerning the switching frequency to ensure the minimal input current ripples [32]. However, the overall efficiency drops significantly when the converter operates at the maximum and heavy loads. Also, the low DC output voltage of the proposed converter appears, which is one of the most common issues of the EVs DC-DC converters [23]. This problem was tackled in [33]. The authors proposed integrating a voltage multiplier to increase the converter voltage gain. The problem of discontinuous output current appears on this model due to the lack of inductors on the output stage [34]. Another DC-DC converter design in [34] utilizes a switched-inductor with a switched-capacitor to obtain high gain. The main advantage of this converter is that it reduces voltage stress on the power elements. However, it has a limited operating range, and such design increases the number of switches and capacitors, reducing system reliability. A Z-source DC-DC converter is designed using the same passive components as shown in Figure 12 (a). This converter has the feature of stepping up and stepping down the voltage. Such a converter is mainly used in medium/high power applications, especially renewable energy [35]. In [36], the authors justified this design's low input current ripple content. However, having lower ripples in such converter results in a larger passive elements size. Moreover, this converter's developed control-to-output transfer function considering parasitic elements has a right-hand pole-zero, complicating the controller design [36]. The study showed that the converter at high power would suffer from the parasitic elements as the efficiency drops below 90% [35]. Another study showed a modified topology of the conventional converters that utilize a diode capacitor multiplier to increase the gain and make the system modular. Such design provides the choice to select the front-end of the converter to meet the application requirement, then a suitable connection for the multiplier is configured to achieve the required gain. The main drawback of this design is that it utilizes a vast number of capacitors that affect the design's reliability [34]. To overcome the switching losses problem in a conventional boost converter, soft-switching topology is introduced by switching at zero voltage or current instants. Accordingly, the power loss at this instant is zero. The resonant converter in [37] utilizes this technique by adding an auxiliary switch to the converter. A resonant tank circuit is added in conjunction with the switch to perform this operation. By setting the duty cycle of the auxiliary switch lower than the main switch, soft switching can be achieved. The zero voltage switching is ensured by turning on the main switch [23]. However, the auxiliary switch assures zero current switching. Ensuring soft-switching reduces the weight and size of the converter. On the other hand, the main drawback of this type of converters is that they can operate at a low power only with low output gains. Also, a proper design should be done to operate at the resonant frequency, otherwise operating at other frequencies attenuates the output voltage and reduces the gain. This design is unreliable since the resonant frequency changes if one of the passive elements changes due to time factors such as material degradation or insulation failures[38],[39].

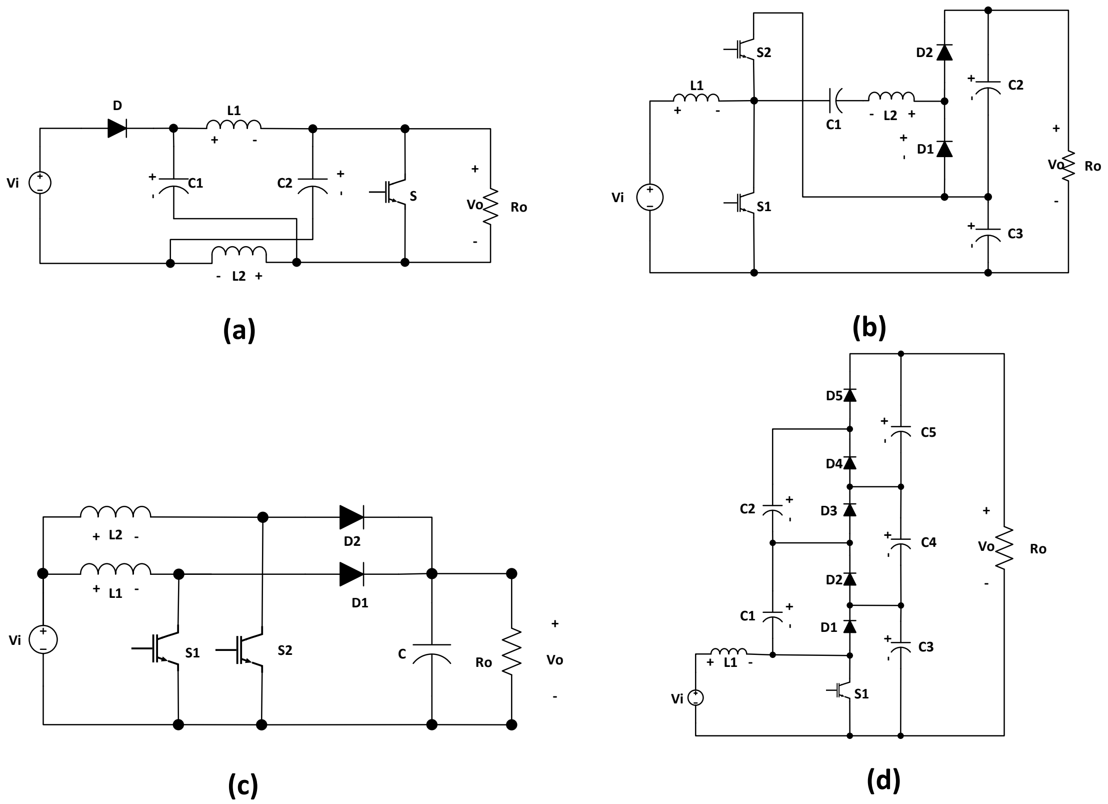

(a) (b) (c) (d)

Figure 12: Non-Isolated high step-up converters (a) Z source DC-DC converter, (b) Resonant DC-DC Converter, (C)Interleaved DC-DC Converter, (d) Multilevel voltage multiplier DC-DC Converter

2.2.3 Isolated Single-Switch Conventional DC-DC Converters.

For the isolated DC-DC converters, conventional converters are mainly employed in low-power and medium-power EVs applications. Using an HFT, the voltage can be stepped up or down. Hence, the converter can be used in increasing the voltage, which helps in charging the battery in FC applications. Deploying a high-frequency transformer affords galvanic isolation with a high voltage gain, which is considered the main concern of EVs [23]. This isolation is required in the FCEV application since it fully isolates the FC from the battery to avoid any reflected current from the battery to the FC. Conventional low gain isolated power converters are demonstrated in Figure 13. The flyback converters are used in low-power applications. The benefit of this converter is that it has low cost, and it consists of a single switch which makes it easy to control. Due to high current ripple contents, such converters require a large capacitor at the input and output sides. Due to this fact, these converters have poor transformer utilization. For the forward converters, they are mainly utilized in medium power applications. This converter suffers from the same issue of transformer utilization since it is considered a single-ended converter, compared to the bridge-type with double-ended merits [40].

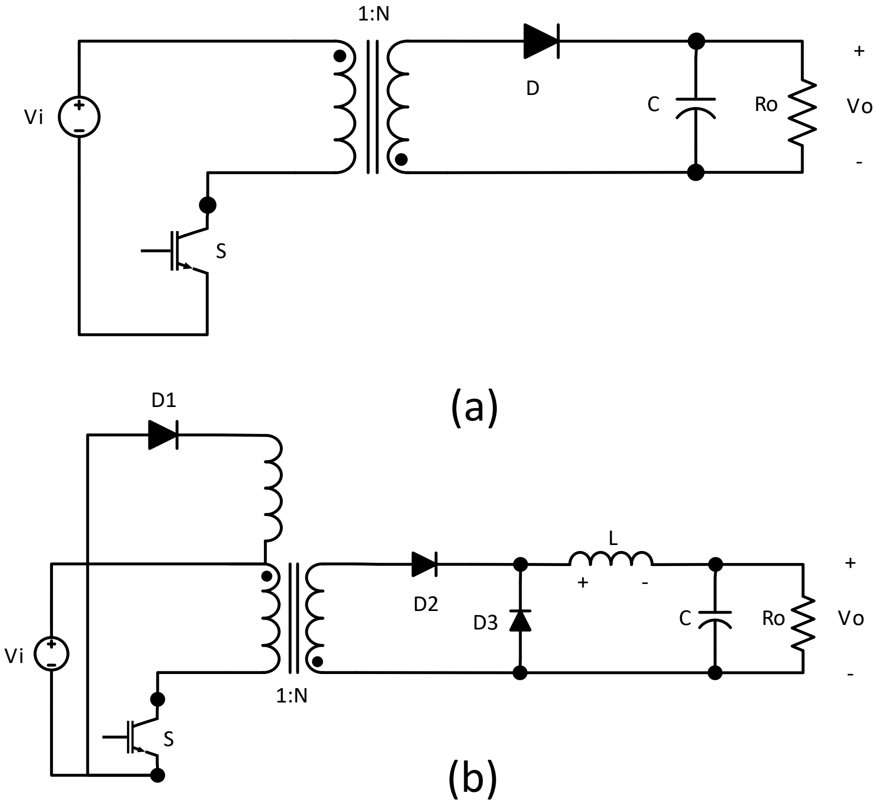

Figure 13: Conventional Isolated DC-DC Converters (a) flyback DC-DC converter, (b) forward DC-DC Converter

2.2.4 Isolated High Gain DC-DC Converters.

Bridge type isolated converters are classified as high power converters where a high gain can be achieved using the duty cycle and the high-frequency transformer ratio. They are used in high power applications due to the full utilization of the transformer and the large range of the duty cycle; transformer optimization can be achieved [41].In addition, using the double-ended topology in bridge-type converters reduces the transformer's size since the full range of the duty cycle can be used. The state-of-the-art FC stacks application highlights that the full-bridge and half-bridge DC-DC converter shown in Figure 14 as the most used topologies [23]. This is since the voltage stress is reduced significantly in bridge converters compared to push-pull converters. Both half-bridge and full-bridge have a single primary winding which helps in transformer utilization. However, in terms of complexity, such converters are complex in terms of control, and they are high in cost because of the number of power switches used and the HFT cost[42].

The authors in [43] justified that the half-bridge and full-bridge topology are suitable with low voltage high current input power supplies. An active-clamped configuration is deployed in isolated topologies in [44] to achieve soft-switching and absorb turn-off voltage spikes. Nonetheless, an active clamped reduces the overall efficiency since it dissipates 1% of the output power, and it adds a circulating current that leads to an increase in the current stress on the converter switches [43]. Besides, it increases the number of components used in the converter design, increasing the converter design and control complexity [44],[43]. Soft switching can be achieved by ensuring zero voltage switching using the pulse width modulation (PWM) technique [45],[46]. By controlling the phase difference between the primary and secondary power switch soft switching is ensured [47]–[49].

Furthermore, conventional non-isolated DC-DC converters can be used as isolated converters by integrating a high-frequency transformer [50]. Isolated topology can be achieved by modifying the design of the converter in a manner to make it suitable to operate the induction principle of the high-frequency transformer. Several converters are converted from their original design to newly isolated topology such as boost, buck-boost, and Cuk converters[51]. Such types of isolated converters are considered low voltage multistage power converters. Due to their duty cycle limitations and low voltage range, a multistage technique is introduced to comply with the power conditioning application [52]. Cuk converter is widely used in applications that require a low input ripple current. This advantage is due to the nature of the built-in low-pass filter of the Cuk converter. This low pass filter eliminates the high-frequency ripple current. This can be done using the parasitic elements of the transformer, such as leakage inductance and magnetizing inductance [53]. These elements can be tuned to modify the converter to a resonant converter which helps to eliminate more harmonics [54]. The isolated Cuk converter has more advantages than other isolated converters, such as full-bridge and half-bridge converters. Compared to the Bridge type converters, the range of duty cycle in the Cuk converter is wider than the bridge-type converters since bridge converters are limited to the duty cycle of 0.5. However, the Cuk converter can operate as a buck from 0-0.5 and boost from 0.5-1, where 0.5 is a unity gain. Also, reducing the number of switches increases the converter's power density by reducing its volume.

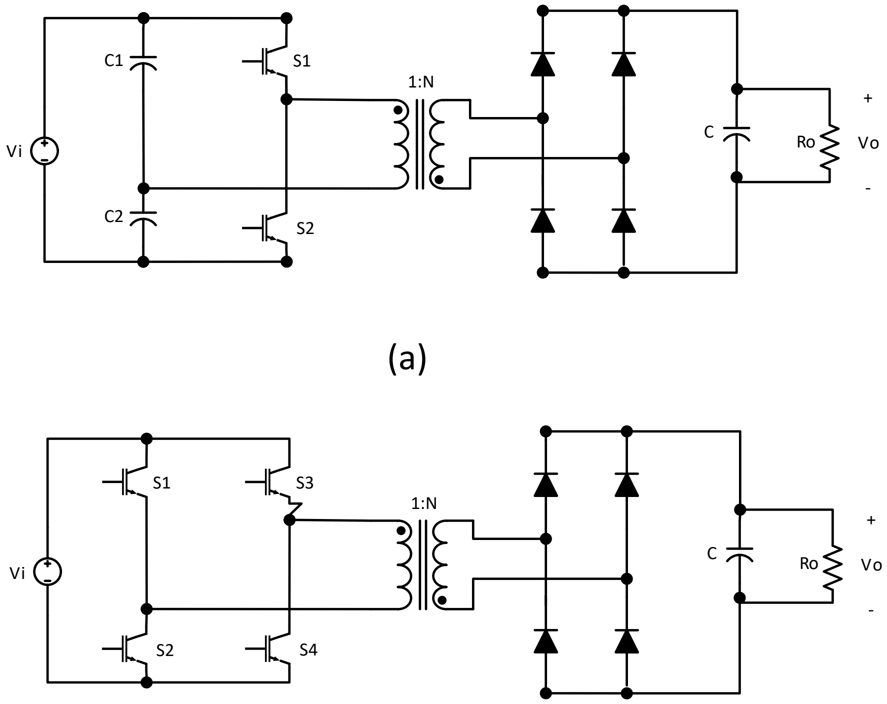

(a)

(b)

Figure 14: High gain isolated DC-DC Converters (a) half-bridge converter, (b) full-bridge converter.

2.3 High-power High-gain DC-DC Converters.

As mentioned earlier, the designed system is considered a high-gain and high-power system. There are several approaches to achieve the required level of power conversion and voltage gain. One of them is integrating high voltage and high-current semiconductor devices into multiple level converters such as parallel/series connections. Such designs result in unequal power-sharing and the unsymmetrical voltage across the semiconductor devices due to the switching delays and converter elements' parasitic resistances. Consequently, a voltage balancing method must be used to avoid system failure if any connected converters fail [55].

Talking about other methods used in HVDC applications where modularity is introduced to the system. Modular design in HVDC application is achieved by connecting several converters to withstand the system requirements with a cost-effective solution. Furthermore, modular design modules can compensate in case of any other converter failure. This introduces the concept of redundancy to the system due to using more modules [56]. In other words, connecting several converters allows power-sharing among the converters, ensuring that each module consistently contributes to handling the total system power. Accordingly, introducing such topologies in a system enhances the overall system performance and reduces the size of the converter [41]. This is due to the fact of using lower voltage rating switches, higher switching frequency that results in reducing the size of the converter elements. Also, it gives the ability to utilize low-power converters in high-power applications.

Several configurations that apply the modular design structure are used in isolated and non-isolated converters. Figure 15 shows the classification of high-power high-gain modular DC-DC converter designs, where both isolated and non-isolated topologies are used with different configurations.

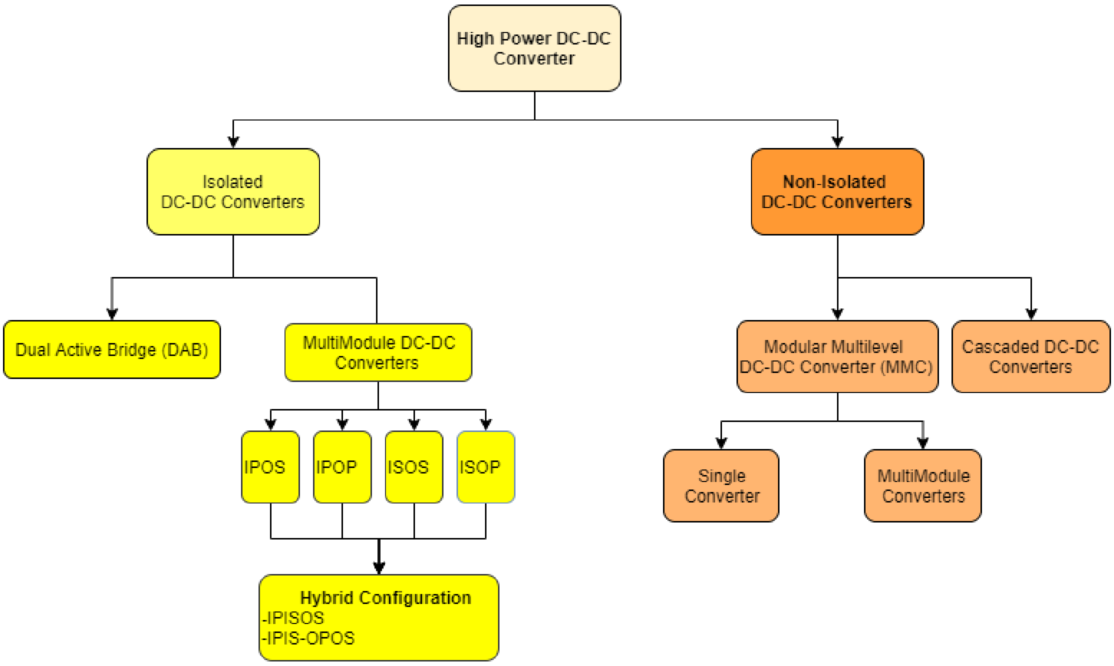

Figure 15: High power DC-DC converters classification

Based on Figure 15, the following sections will cover some of the mentioned topologies for high-gain high-power applications such as FCEV, focusing on multimodule DC-DC converters and highlighting the use of each configuration.

2.4 High-power High-gain Isolated DC-DC Converters.

The following subsections present the high-power high-voltage gain isolated DC-DC converters proposed in previous studies.

2.4.1 Dual Active Bridge (DAB) DC-DC Converter.

DAB converter is one of the most used converters in high-power applications [41]. The converter consists of two active bridges connected via an HFT. The main idea of the DAB topology is that the FB on the primary side converts the input DC voltage to a high frequency squared AC voltage, and the secondary FB rectifies the square wave to a DC output voltage [57]. The intermediate transformer leakage inductance is used as the energy conversion element in this converter [58]. The advantage of this topology is that the power flow is controlled by controlling the bridges' phase, which assures bidirectional power flow. As well as ZVS and ZCS can be achieved using several control techniques [57].

Utilizing efficient control techniques helps in increasing the range of soft switching and reduces transformer current. This ensures a high conversion ratio by selecting a better transformer turns ratio. The disadvantage of using such a converter is that it utilizes eight switches that increase the size and cost of the converter. Also, the bridge switches and HFT should be capable of handling the high amount of power of the application. These problems can be avoided by introducing a modular multi-module topology to ensure that the power is distributed among different converters. The generic multi-module topology will be discussed in the following section to be generalized for other converters.

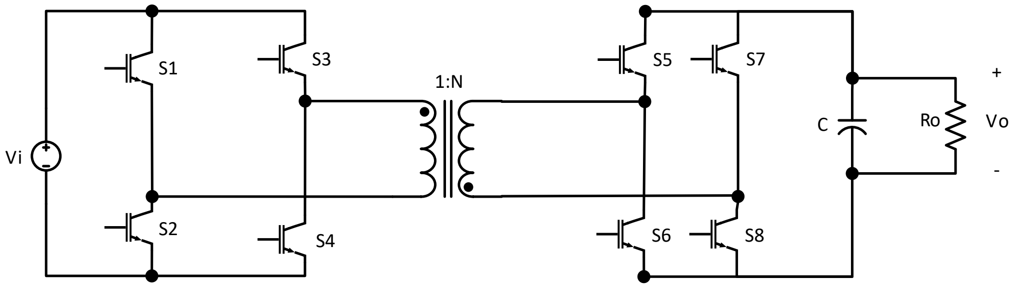

Figure 16: DAB converter

2.5 High-power High-gain Non-Isolated DC-DC Converters.

The following subsections present the high-power high-gain isolated DC-DC converters topologies proposed in previous studies.

2.5.1 Modular Multilevel DC-DC Converter (MMC).

One of the standard non-isolated converters used in HVDC systems is the MMCs. The converter connection is demonstrated in Figure 17. The power exchange in this converter is done using the orthogonal power flow principle at different frequencies between the primary and secondary loops of the converter. Such a converter requires a large filter, making it not promising for DC-DC power conversion[59],[60]. Moreover, the cost of this converter is considered high when it is compared with other topologies. This is due to the large number of semiconductor switching devices used in the MMC DC-DC converter [61]. The study in [62] stated that the MMC is not applicable in high-voltage ratios due to the circulating current in the converter that reduces the efficiency. Such converters are preferred in low voltage ratio applications where galvanic isolation is not required.

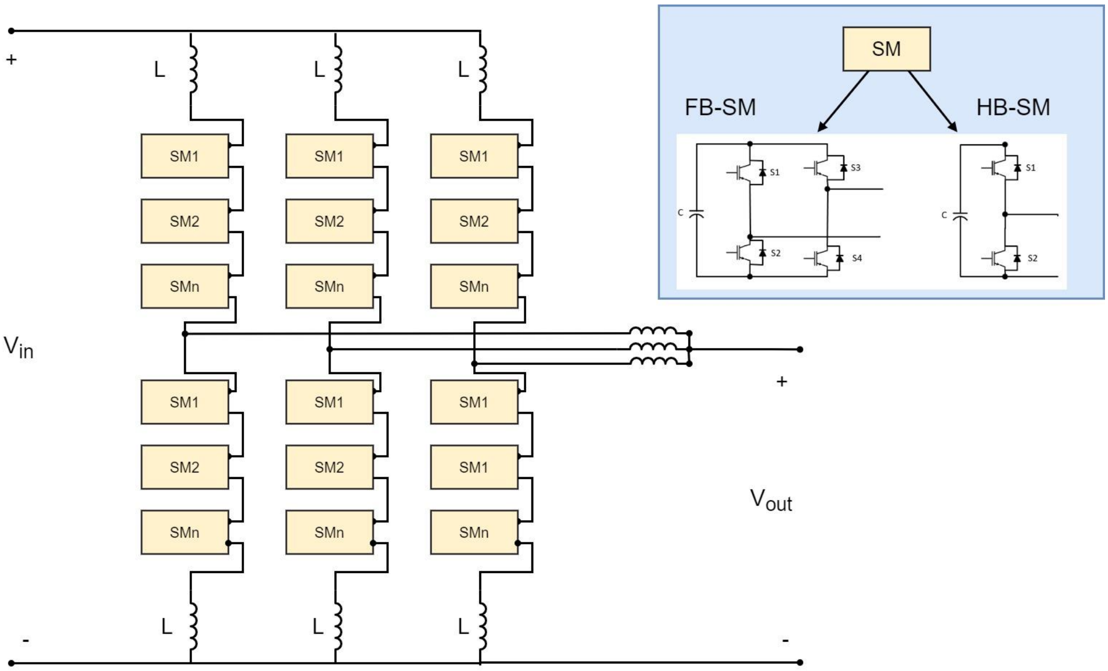

Figure 17:MMC DC-DC Converter diagram

2.5.2 Cascaded DC-DC Converter (MMC).

Cascaded topologies were proposed in several high-power DC-DC converter designs. Compared to the switched capacitor and coupled inductor designs, such topology provides a high voltage gain with minimal stresses and high-power conversion. One way of increasing the gain of the power conditioning unit is by cascading multiple converters in series, as shown in Figure 18. The voltage is boosted at each stage until it reaches the desired level. Such design reduces the stress on the power elements of the converter. However, this design lacks redundancy since the whole system fails if one of the converters is damaged. Also, the sizes of the converters are not consistent since the voltage, and current requirements vary at each stage, and the efficiency is affected since it is the multiplication of the overall stages.

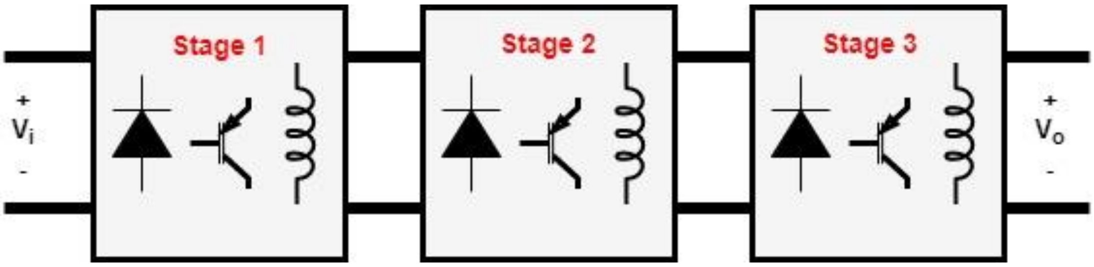

Figure 18: Multi-stage DC-DC converter cascading topology

Another study [63] proposed a hybrid cascaded DC-DC converter. The proposed converter consists of power converters and a stack of sub-modules. The proposed converter is presented in Figure 19. The system operates as a multiphase system, where each stage consists of a converter with an energy storage device. The purpose of using multiple phases is to avoid system interruption, as mentioned earlier. These converters require many semiconductor switching devices to be connected in series to withstand the system requirements. Also, this results in higher conduction losses, affecting the converter's overall efficiency [64].

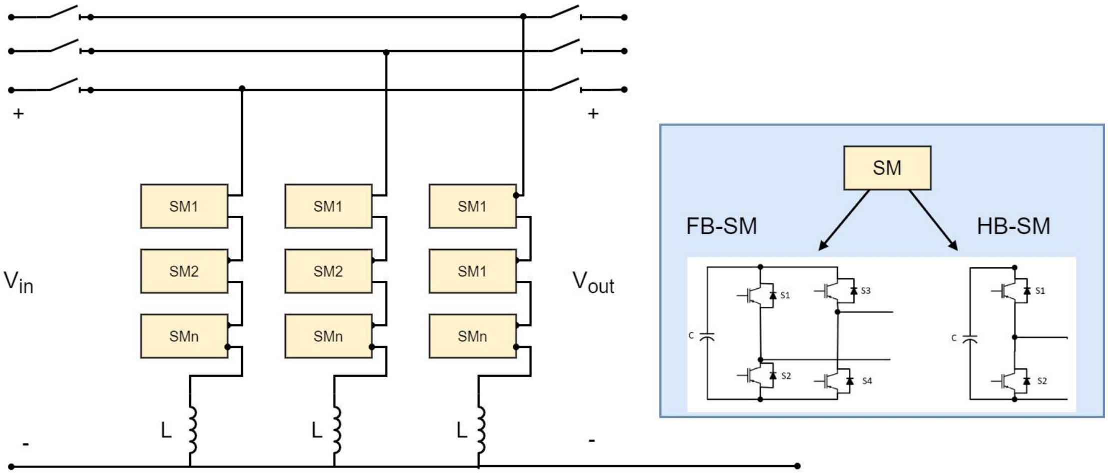

Figure 19: Hybrid MMC converter diagram

2.6 Multi-Module DC-DC Converter.

A multi-module system configuration is one of the most attractive areas where the concept of modularity, reliability, and redundancy is achieved. The main idea of these topologies is to connect the converters to suit the application requirements, whether to achieve high gain or to transfer high power, or both. The authors in [41] presented several topologies that can be used in designing a modular DC-DC converter such as input-parallel-output-series (IPOS), input-series-output-series (ISOS), input-parallel-output-parallel (IPOP) and input-series-output-parallel (ISOP). The main idea of these topologies is to connect the ports in a manner that suits the application. For instance, in FC applications, the output current of the FC is high, and the voltage of the FC is low. An input-parallel topology is considered a convenient method since the current is divided into multiple paths, and the power is shared among all the converters. The description of multi-module topologies and where they can be used to meet the system requirements are discussed in the following subsections:

A. Input Series Output Series ISOS

An ISOS connection is presented in Figure 20, where the input and output terminals of the modules are connected in series, which reduces the voltage stress on the switching devices and reduces the power level for each converter. This configuration is utilized in high input-output voltage applications [65]. The ISOS is usually implemented in high input high output voltages where the semiconductor switches cannot withstand system voltage. Such configuration enables low voltage ratings for power switches used in the converter. Using a proper control technique assures input voltage sharing (IVS) and output voltage sharing (OVS). The voltages at the input and the output of each converter are $\frac{V_{in}}{n},\frac{V_o}{n}$ where n is the number of modules.

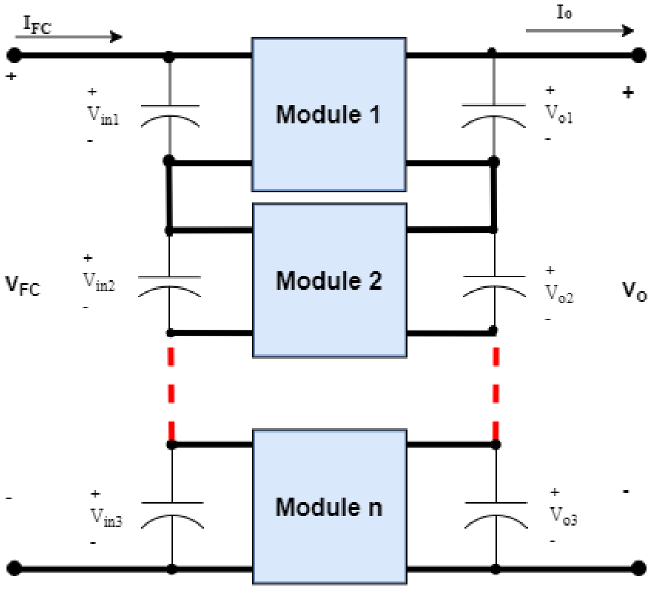

Figure 20: Input series Output series ISOS circuit diagram

B. Input Series Output Parallel ISOP

This connection is preferable in high input voltage and high output current systems [65]. Figure 21 shows the configuration of several DC-DC converters where the modules' inputs and outputs are connected in series and parallel, respectively. Such connection is used in high step down, where a high current flows at the output side of the converters and the input voltage is not within the semiconductor switches voltage rating. Using a proper control that ensures IVS and outputs current sharing OCS, the input voltage of each module is reduced to $\frac{V_{in}}{n}$ and the output current of each module is reduced to $\frac{I_o}{n}$, where n is the number of connected modules.

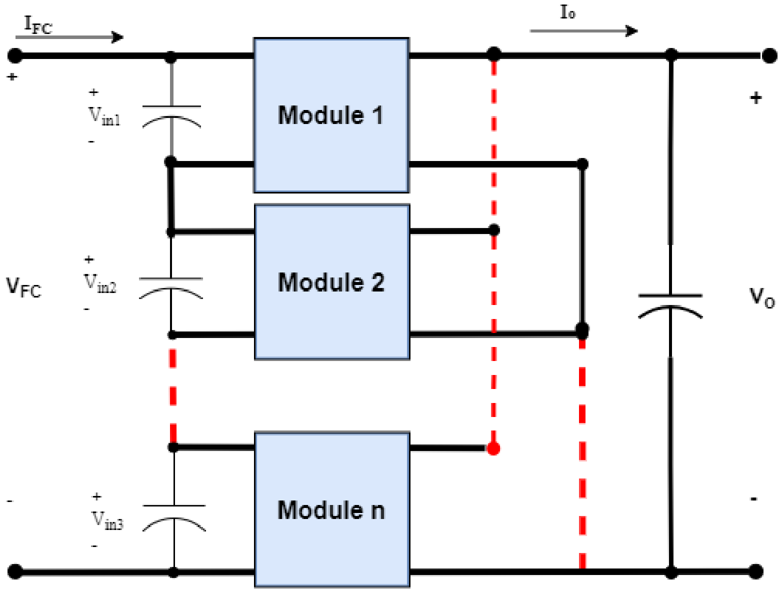

Figure 21: ISOP circuit diagram

C. Input Parallel Output Parallel IPOP

The IPOP configuration is utilized in applications with high input high output current [66]. Figure 22 shows the converters connections, where the input and output sides are connected in parallel. The connection is used when the semiconductor switching devices' current rating is below the input and output current of the application. By ensuring input current sharing ICS and OCS, the current is reduced to $\frac{I_{in}}{n}$ and $\frac{I_o}{n}$ at input and output sides where n is the number of converters used.

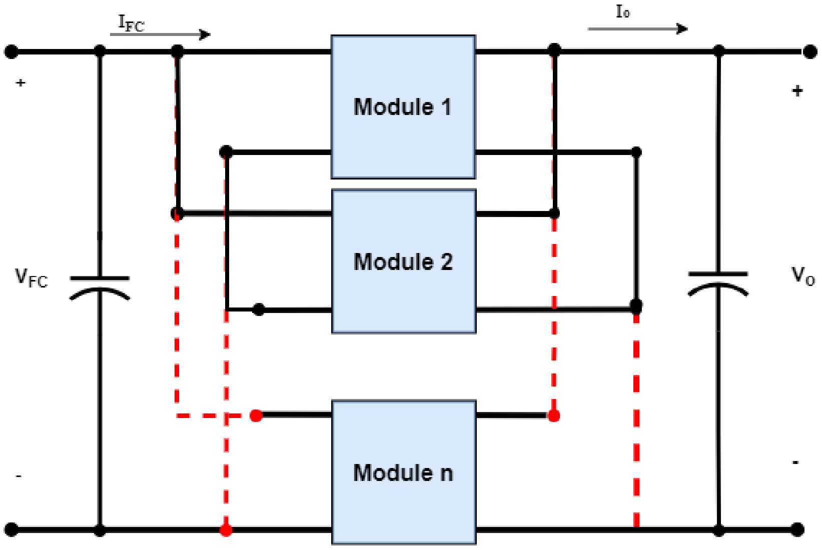

Figure 22: Input Parallel Output Parallel circuit diagram

D. Input Parallel Output series ISOP

IPOS DC-DC converter configuration is shown in Figure 23. This connection is used high input current and high output voltage applications [67]. The input side of the converter is connected in parallel to ensure that the high current drawn from the supply is shared between the connected modules. However, the output side is connected in series to step up the voltage to the desired level. This connection is used when the input semiconductor switching devices cannot withstand the high input current. And by ensuring ICS and OVS, the input current is reduced to $\frac{I_{in}}{n}$ and output voltage is reduced to $\frac{V_O}{n}$ where n is the number of modules.

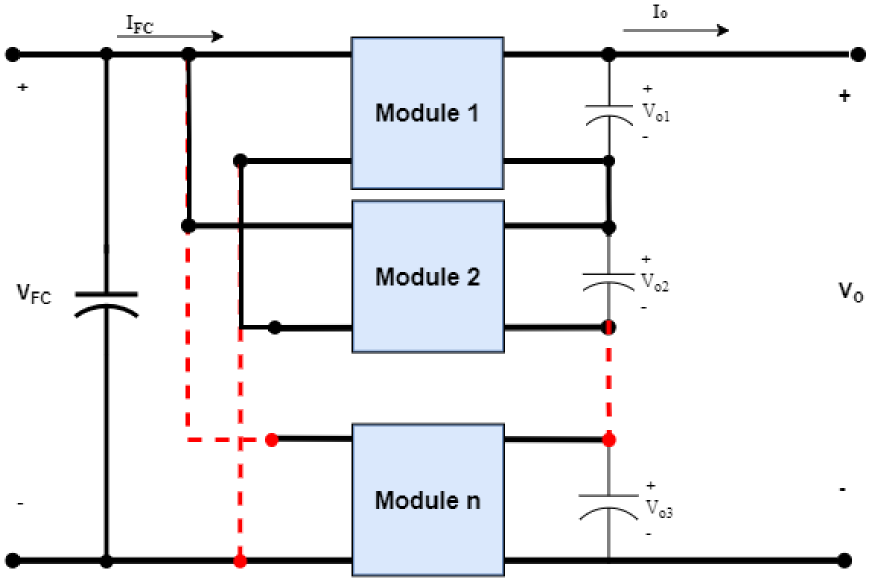

Figure 23: Input Parallel Output Series circuit diagram

E. Hybrid Input-Output Series/Parallel Connection

IPIS-OPOS is a general hybrid configuration of the presented topologies. A hybrid connection connects several modules terminals in series and parallel. Figure 24 shows modules configuration. Using a proper control, the IVS and ICS is assured, which reduces the current and voltage at the input side to $\frac{V_{in}}{a}, \frac{I_{in}}{b}$ where a and b the connected modules series and parallel, respectively. And by ensuring OVS and OCS, the voltage and current at the output side are reduced to $\frac{V_o}{c}, \frac{I_o}{d}$ where c is the connected modules in series and *d* is the connected modules in parallel. Such design increases the system modularity and operates with high input-output voltage and current systems. However, the complexity of controlling the overall system is the cost since the control should ensure proper power-sharing between the converters to avoid voltage and power mismatch [41].

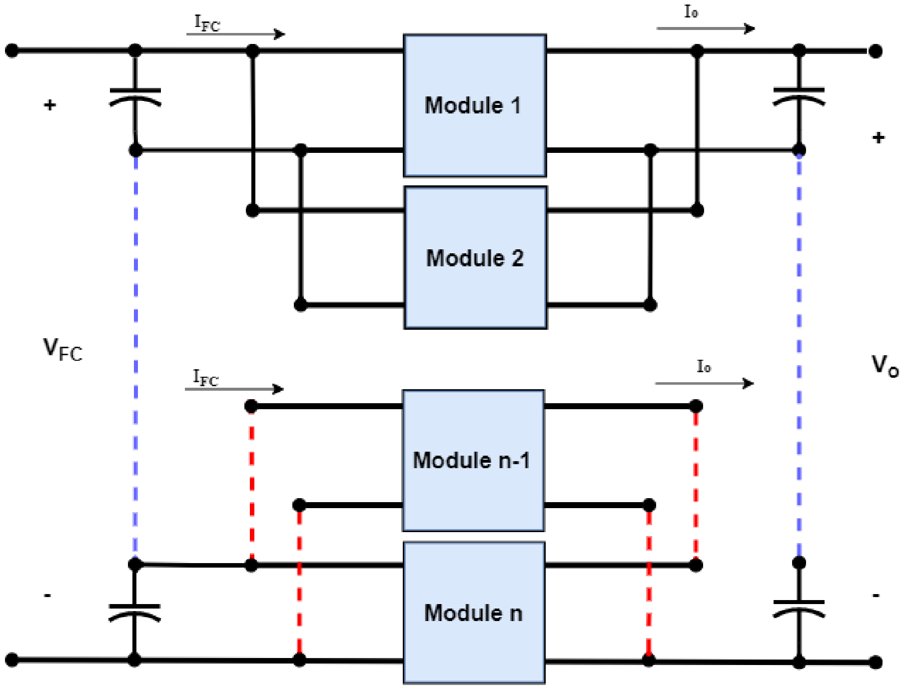

Figure 24: Hybrid IPIS-OPOS circuit diagram

All in all, the multi-module system specification can be summarized in the following table:

Table 2.2: Multi-module system specifications

Connection	**Input Voltage**	**Output Voltage**	**Input Current**	**Output Current**
IPOS	V_{in}	$\frac{V_o}{n}$	$\frac{I_i}{n}$	I_o
IPOP	V_{in}	V_o	$\frac{I_i}{n}$	$\frac{I_o}{n}$
ISOP	$\frac{V_{in}}{n}$	V_o	I_i	$\frac{I_o}{n}$
ISOS	$\frac{V_{in}}{n}$	$\frac{V_o}{n}$	I_i	I_o
Hybrid	$\frac{V_{in}}{a}$	$\frac{V_o}{c}$	$\frac{I_i}{b}$	$\frac{I_o}{d}$

2.7 Adopted topology and system parameters

Based on the aforementioned information in the literature, Table 2.3 is obtained to compare different topologies of high gain high power converters. The Cuk converter was selected considering the isolated topology, which provides galvanic isolation between the FC and the battery. Besides, it has a low input ripple current which is considered an advantage of the Cuk converter with such applications. The adopted modular topology is IPOS. The FC current is divided into three different converters, ensuring a high voltage gain. Figure 25 presents the adopted topology with the converter in their ideal conditions.

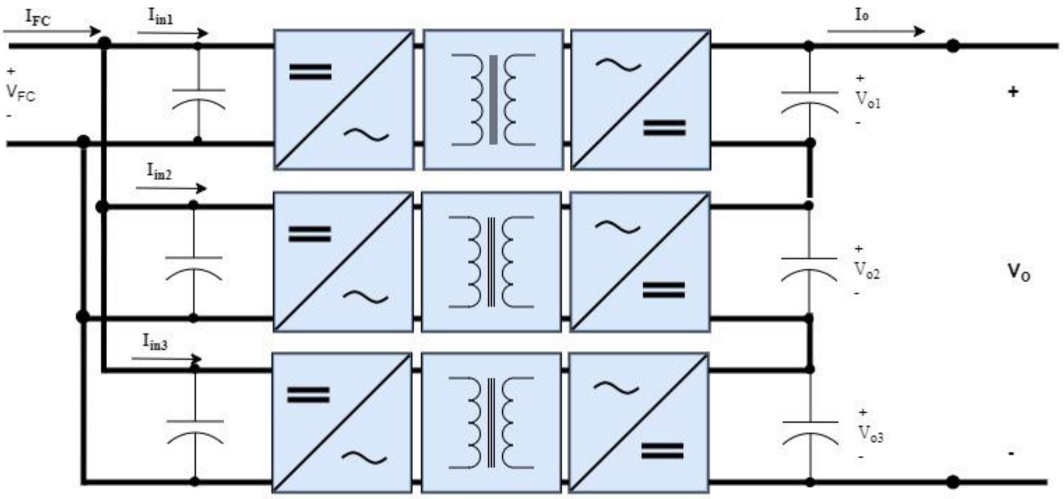

Figure 25: IPOS topology

Table 2.3:High power DC-DC Converters comparison [23],[24],[68]

Features	MMC	IBC	Z-Source	HBC	FBC	DAB	Isolated Cuk
Single Polarity Output Voltage	Present	Present	Present	Not Present	Not Present	Not Present	Not Present
Complexity of control circuit	Complex	Moderate	Simple	Moderate	Moderate	Moderate	Simple
Transformer Utilization	-	-	-	Double-ended	Double-ended	Double-ended	Single-ended
Current/Voltage ripple	High	High	High	High	High	High	Low
Number of elements	Depends on how many SMs used	2 switches 2 inductors 1 capacitor 2 diodes	1 switch 2 inductors 2 capacitors 1 diode	2 Switches 2 capacitors 4 Didoes 1 HFT	4 switches 1 capacitor 4 Diodes 1 HFT	8 switches 2 capacitors 1 HFT	1 switch 2 inductors 4 capacitors 1 HFT 1 diode

Chapter 3: DC-DC Converter Modeling

There are several modeling methods used to understand and analyze the converter's behavior. In this chapter, isolated-Cuk is modeled ing is presented. The isolated Cuk converter is modeled using the state-space model (SSM), considering the converter non-idealities presented in [69] with the small ac dynamic model used in [70] to obtain the control to output current and voltage transfer functions. This model represents the converter using the following equations:

$$\dot{x} = Ax + Bu \tag{3.1}$$

$$y = Cx + Du \tag{3.2}$$

An average model can be obtained by finding each switching state separately, when the switch is on and when the switch is off. This average model is obtained considering the weight of each mode with respect to the duty cycle (d). The following equation presents a general form of the averaged SSM:

$$X_{avg} = dX_{on} + (1-d)X_{off} \tag{3.3}$$

The following assumptions are made to obtain the model of isolated Cuk converter shown in Figure 26:

- Parasitic resistances are taken into account such as:
    - Inductor resistances r_L
    - Equivalent Series Resistance (ESR) of the capacitor r_c
    - On-state switch resistance r_s
    - On-State diode resistance r_D
- Ideal lossless HFT transformer is considered with a turns-ratio of $1{:}N$
- Cuk converter is operating in continuous conduction mode (CCM)

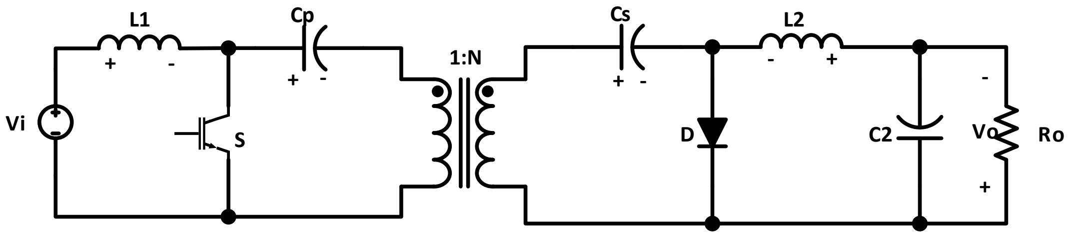

Figure 26:Isolated Cuk converter circuit

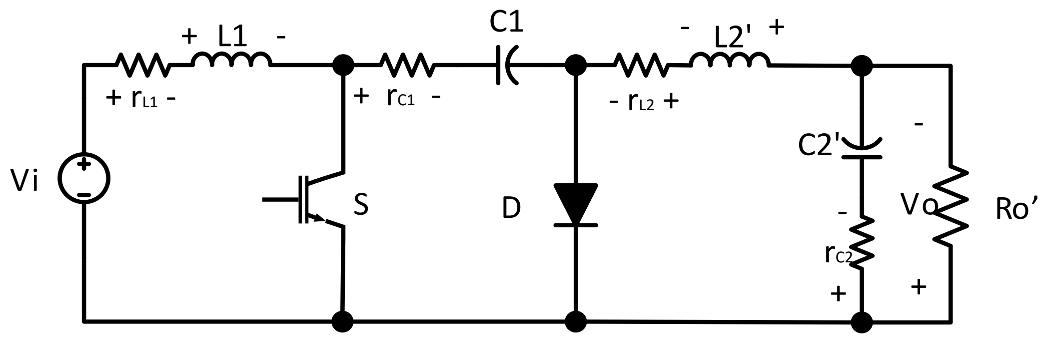

Figure 27: Non-Isolated Cuk converter circuit

The transformation from the isolated model to the non-isolated model is done by referring the converter elements to the primary side of the HFT. The transformation equations are as follow:

$$C_1 = \frac{C_P C_S N^2}{C_P + N^2 C_S} \tag{3.4}$$

$$L'_2 = \frac{L_2}{N^2} \tag{3.5}$$

$$C'_2 = C_2 N^2 \tag{3.6}$$

$$R'_o = \frac{V_o^2}{N^2 P_o} \tag{3.7}$$

Where C_p, C_s are the primary and secondary capacitors used in the isolated model, C_1, C'_2, L'_2 are the equivalent input, output capacitors, and output inductor referred to the primary side of HFT, respectively. While N is the turns ratio of the HFT and R'_o is the output load referred to the primary side.

Figure 28 shows the converter with the parasitic elements.

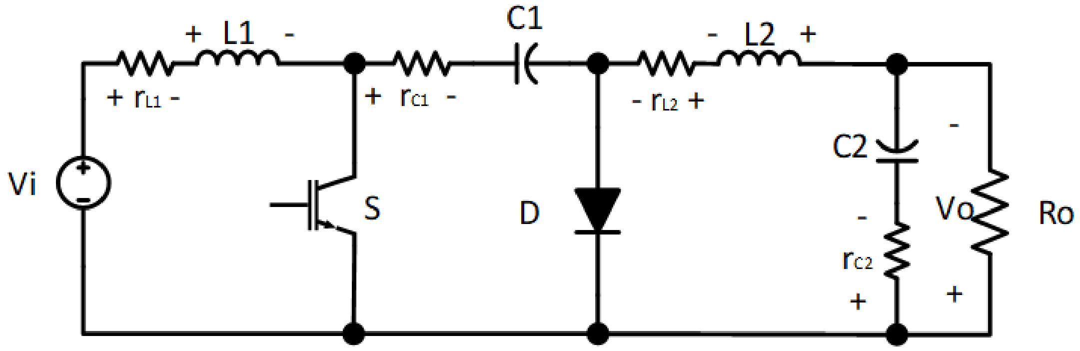

Figure 28: Non-ideal Cuk converter circuit

Moreover, in ideal conditions, the voltage gain is defined as follows:

$$\frac{V_o}{V_i} = \frac{d}{1-d} \tag{3.8}$$

This formula is not valid when considering parasitic elements in the converter. The voltage gain considering non-ideal conditions can be derived using state-space equations. The transfer function of the converters is obtained using state-space equations. However, when the system operates in steady-state conditions, the state variables change is neglected. Thus, equation (3.1) can be equated to zero. Hence, the following equations can be obtained:

$$0 = Ax + Bu \tag{3.9}$$

$$\frac{V_o}{V_i} = \frac{y}{u} = -CA^{-1}B \tag{3.10}$$

A linear model is obtained through this technique to design current-mode and voltage-mode control for the converter. Small signal models are based on studying the effects of small input perturbations on the overall converter performance and stability. The small variations are usually considered for the input voltage and the duty cycle [71].

3.1 State-Space Model (SSM) of a Single Cuk Converter

As mentioned earlier, the parasitic elements are considered to obtain an accurate transfer function. The switch is replaced with r_s which represents the internal resistance of the switch when the switch is on. Also, the diode, in this case, operates on the reverse bias mode, and no current flows through it. The state-space representations when the switch is on can be obtained using (3.11) to (3.15):

$$L_1 \frac{di_{L1}}{dt} = V_i + (-r_s - r_{L1}) i_{L1} - r_s i_{L2} \tag{3.11}$$

$$L_2 \frac{di_{L2}}{dt} = \left(\frac{-R_o}{r_{c2} + R_o}\right) V_{c2} + V_{c1} - r_s i_{L1} - \left(r_s + r_{c1} + r_{L2} + \frac{R_o r_{c2}}{R_o + r_{c2}}\right) i_{L2} \tag{3.12}$$

$$C_1 \frac{dV_{c1}}{dt} = -i_{L2} \tag{3.13}$$

$$C_2 \frac{dV_{c2}}{dt} = \left(\frac{R_o}{R_o + r_{c2}}\right) i_{L2} + \left(\frac{-1}{R_o + r_{c2}}\right) V_{c2} \tag{3.14}$$

$$V_o = \left(\frac{R_o r_{c2}}{R_o + r_{c2}}\right) i_{L2} + \left(\frac{R_o}{R_o + r_{c2}}\right) V_{c2} \tag{3.15}$$

Thus, the state space representation of the converter when the switch is turned on using (3.1) and (3.2):

$$x = \begin{bmatrix} i_{L1} \\ i_{L2} \\ V_{c1} \\ V_{c2} \end{bmatrix}, u = [V_i] \tag{3.16}$$

$$A_1 = \begin{bmatrix} \frac{-r_s - r_{L1}}{L_1} & -\frac{r_s}{L_1} & 0 & 0 \\ -\frac{r_s}{L_2} & -\frac{1}{L_2}\left(r_s + r_{c1} + r_{L2} + \frac{R_o r_{c2}}{R_o + r_{c2}}\right) & \frac{1}{L_2} & \frac{1}{L_2}(\frac{-R_o}{r_{c2} + R_o}) \\ 0 & -\frac{1}{C_1} & 0 & 0 \\ 0 & \frac{1}{C_2}\left(\frac{R_o}{R_o + r_{c2}}\right) & 0 & \frac{1}{C_2}\left(\frac{-1}{R_o + r_{c2}}\right) \end{bmatrix} \tag{3.17}$$

$$B_1 = \begin{bmatrix} \frac{1}{L_1} \\ 0 \\ 0 \\ 0 \end{bmatrix} \tag{3.18}$$

$$C_1 = \begin{bmatrix} 0 & \left(\frac{R_o r_{c2}}{R_o + r_{c2}}\right) & 0 & \left(\frac{R_o}{R_o + r_{c2}}\right) \end{bmatrix} \tag{3.19}$$

$$\begin{bmatrix} \frac{di_{L1}}{dt} \\ \frac{di_{L2}}{dt} \\ \frac{dV_{c1}}{dt} \\ \frac{dV_{c2}}{dt} \end{bmatrix} = \begin{bmatrix} \frac{-r_s - r_{L1}}{L_1} & -\frac{r_s}{L_1} & 0 & 0 \\ -\frac{r_s}{L_2} & -\frac{1}{L_2}\left(r_s + r_{c1} + r_{L2} + \frac{R_o r_{c2}}{R_o + r_{c2}}\right) & \frac{1}{L_2} & \frac{1}{L_2}\left(\frac{-R_o}{r_{c2} + R_o}\right) \\ 0 & -\frac{1}{C_1} & 0 & 0 \\ 0 & \frac{1}{C_2}\left(\frac{R_o}{R_o + r_{c2}}\right) & 0 & \frac{1}{C_2}\left(\frac{-1}{R_o + r_{c2}}\right) \end{bmatrix} \begin{bmatrix} i_{L1} \\ i_{L2} \\ V_{c1} \\ V_{c2} \end{bmatrix} + \begin{bmatrix} \frac{1}{L_1} \\ 0 \\ 0 \\ 0 \end{bmatrix} [V_i] \tag{3.20}$$

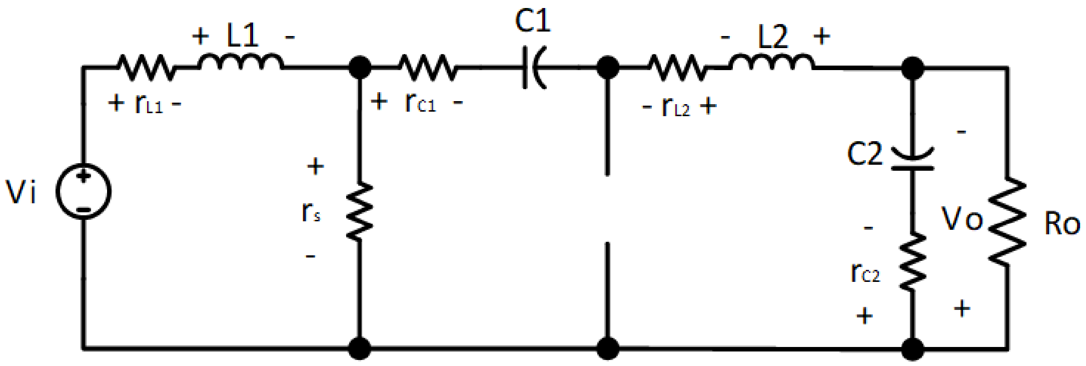

Figure 29: Cuk converter model when the switch state is on

Afterward, when the switch is off is obtained using the same steps. However, in this case, the switch is replaced with an open circuit, and the diode is replaced with the internal resistance of the diode r_D.

$$L_1 \frac{di_{L1}}{dt} = V_i - V_{c1} + (-r_{L1} - r_{c1} - r_D)i_{L1} - r_D i_{L2} \tag{3.21}$$

$$L_2 \frac{di_{L2}}{dt} = \left(\frac{-R_o}{r_{c2} + R_o}\right) V_{c2} - r_D i_{L1} - \left(r_D + r_{L2} + \frac{R_o r_{c2}}{R_o + r_{c2}}\right) i_{L2} \tag{3.22}$$

$$C_1 \frac{dV_{c1}}{dt} = i_{L1} \tag{3.23}$$

$$C_2 \frac{dV_{c2}}{dt} = \left(\frac{R_o}{R_o + r_{c2}}\right) i_{L2} + \left(\frac{-1}{R_o + r_{c2}}\right) V_{c2} \tag{3.24}$$

$$V_o = \left(\frac{R_o r_{c2}}{R_o + r_{c2}}\right) i_{L2} + \left(\frac{R_o}{R_o + r_{c2}}\right) V_{c2} \tag{3.25}$$

The state-space representation of the converter when the switch is turned off:

$$A_2 = \begin{bmatrix} \frac{(-r_{L1} - r_{c1} - r_D)}{L_1} & -\frac{r_D}{L_1} & -\frac{1}{L_1} & 0 \\ -\frac{r_D}{L_2} & -\frac{1}{L_2}\left(r_D + r_{L2} + \frac{R_o r_{c2}}{R_o + r_{c2}}\right) & 0 & \frac{1}{L_2}(\frac{-R_o}{r_{c2} + R_o}) \\ \frac{1}{C_1} & 0 & 0 & 0 \\ 0 & \frac{1}{C_2}\left(\frac{R_o}{R_o + r_{c2}}\right) & 0 & \frac{1}{C_2}\left(\frac{-1}{R_o + r_{c2}}\right) \end{bmatrix} \tag{3.26}$$

$$B_2 = \begin{bmatrix} \frac{1}{L_1} \\ 0 \\ 0 \\ 0 \end{bmatrix} \tag{3.27}$$

$$C_2 = \begin{bmatrix} 0 & \left(\dfrac{R_o r_{c2}}{R_o + r_{c2}}\right) & 0 & \left(\dfrac{R_o}{R_o + r_{c2}}\right) \end{bmatrix} \tag{3.28}$$

Then substituting in (3.1) and (3.3):

$$\begin{bmatrix} \dfrac{di_{L1}}{dt} \\ \dfrac{di_{L2}}{dt} \\ \dfrac{dV_{c1}}{dt} \\ \dfrac{dV_{c2}}{dt} \end{bmatrix}$$

$$= \begin{bmatrix} \dfrac{(-r_{L1} - r_{c1} - r_D)}{L_1} & -\dfrac{r_D}{L_1} & -\dfrac{1}{L_1} & 0 \\ -\dfrac{r_D}{L_2} & -\dfrac{1}{L_2}\left(r_D + r_{L2} + \dfrac{R_o r_{c2}}{R_o + r_{c2}}\right) & 0 & \dfrac{1}{L_2}\left(\dfrac{-R_o}{r_{c2} + R_o}\right) \\ \dfrac{1}{C_1} & 0 & 0 & 0 \\ 0 & \dfrac{1}{C_2}\left(\dfrac{R_o}{R_o + r_{c2}}\right) & 0 & \dfrac{1}{C_2}\left(\dfrac{-1}{R_o + r_{c2}}\right) \end{bmatrix} \begin{bmatrix} i_{L1} \\ i_{L2} \\ V_{c1} \\ V_{c2} \end{bmatrix} \tag{3.29}$$

$$+ \begin{bmatrix} \dfrac{1}{L_1} \\ 0 \\ 0 \\ 0 \end{bmatrix} [V_i]$$

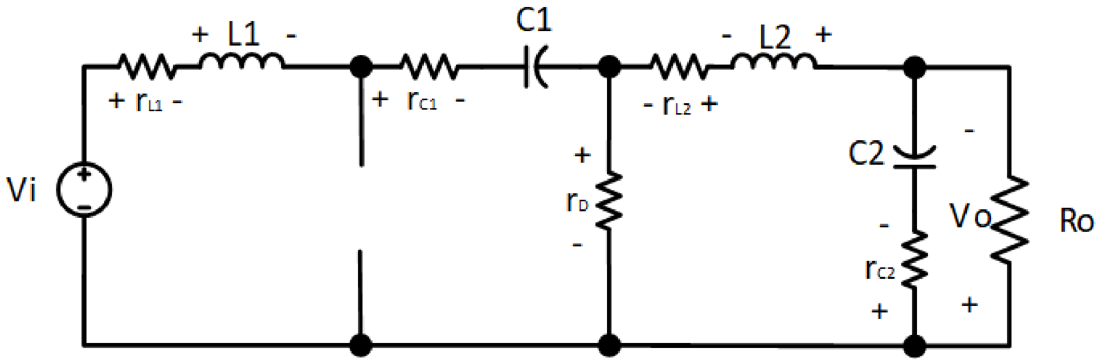

Figure 30: Cuk converter when the switch state is off

Using (3.3), the averaged SSM can be observed:

$$A_{avg} =$$

$$\begin{bmatrix} \frac{d(-r_s + r_{c1} + r_D) + (-r_{L1} - r_{c1} - r_D)}{L_1} & \frac{d(r_D - r_s) - r_D}{L_1} & -\frac{(1-d)}{L_1} & 0 \\ \frac{d(r_D - r_s) - r_D}{L_2} & \frac{d(-r_s - r_{c1} + r_D) - (r_D + r_{L2} + \frac{R_o r_{c2}}{R_o + r_{c2}})}{L_2} & 0 & \frac{1}{L_2}\left(\frac{-R_o}{r_{c2} + R_o}\right) \\ -\frac{1-d}{C_1} & -\frac{d}{C_1} & 0 & 0 \\ 0 & \frac{1}{C_2}\left(\frac{R_o}{R_o + r_{c2}}\right) & 0 & \frac{1}{C_2}\left(\frac{-1}{R_o + r_{c2}}\right) \end{bmatrix} \tag{3.30}$$

$$B_{avg} = \begin{bmatrix} \frac{1}{L_1} \\ 0 \\ 0 \\ 0 \end{bmatrix} \tag{3.31}$$

$$C_{avg} = \left[0 \quad \left(\frac{R_o r_{c2}}{R_o + r_{c2}}\right) \quad 0 \quad \left(\frac{R_o}{R_o + r_{c2}}\right)\right] \tag{3.32}$$

3.2 ac Small Signal Analysis

The averaged model obtained from (3.30) to (3.32) becomes linear after being averaged but time variant since the matrices (A, B, and C) depend on the duty ratio. Hence, the system model is analyzed at the neighborhoods of the operating point. This can be done by introducing deviations from the averaged state space through the small-signal where it can be written as follow:

$$d = D + \hat{d} \tag{3.33}$$

$$\dot{x} = X + \hat{x} \tag{3.34}$$

$$v_{in} = V_{in} + \widehat{v_{\iota n}} \tag{3.35}$$

Where $\hat{d}$, $\hat{x}$, and $\widehat{v_{\iota n}}$ are the small dynamic variations value, and the capital letters D, X and V_{in} are the steady-state values. Then by substituting them in the averaged model. The state-space equations become:

$$\hat{\dot{x}} = \big(A_1 D + A_2(1 - D)\big)\hat{x} + \dot{\big(}(A_1 - A_2)X + (B_1 - B_2)V_{\iota n}\big)\hat{d} \tag{3.36}$$

$$\hat{y} = \left(C_1 D + C_2(1 - D)\right)\hat{x} \tag{3.37}$$

The Laplace transform of the above equations is:

$$\hat{x}(s) = (sI - A)^{-1}\left((A_1 - A_2)X + (B_1 - B_2)V_{in}\right)\hat{d}(s) \tag{3.38}$$

$$\frac{\widehat{V_o}(s)}{\hat{d}(s)} = C(sI - A)^{-1}(A_1 - A_2)X \tag{3.39}$$

Or

$$\frac{\widehat{I_o}(s)}{\hat{d}(s)} = C(sI - A)^{-1}(A_1 - A_2)X \tag{3.40}$$

Where matrix C differs based on the output, either current or voltage. Afterward, based on the derived models, the control-to-output transfer functions of the Cuk converter can be obtained by substituting the value of the designed converter. The transfer functions of control-to-output voltage and control-to-output current are obtained in the next chapter.

Chapter 4: DC-DC Converter Control

In this chapter, the control of the presented DC-DC converter is addressed. The constant current control of the modeled Cuk converter is presented. Moreover, the control-to-output voltage and control-to-output current models are obtained using the averaged model derived in the previous chapter. The design of the PI controller is then discussed. Also, the FOPI controller and its approximated model are presented and compared with the conventional PI controller. Afterward, the digital control of the derived models is obtained and verified. Then the overall system verification through simulation using a transient model in Simulink is presented.

4.1 Control-to-Output Voltage of Cuk Converter

The linearized model of the Cuk converter obtained in Chapter 3 using the state-space model is utilized to derive the converter's control-to-output voltage transfer function. Table 4.1 and Table 4.2 show the parameters used to design Cuk converter and its parasitic elements to obtain the system transfer function. These parameters are selected based on overall system requirements. The resulting control-to-output voltage transfer function is shown in (4.1).

Table 4.1: Control-to-output voltage design parameters

Parameters	**Specifications**
Input Voltage $\boldsymbol{V_{in}}$	430V
Output Current $\boldsymbol{I_o}$	111.1A
Output Power $\boldsymbol{P_o}$	40kW
Switching frequency	20kHz

Table 4.2 Converter elemnts with parasitic resistances

Component Type	**Part Number**	**Value**	**~ Parasitic R (Ω)**
Inductor 1&2	Hammond 195C100	1mH	0.0036 **Ω**
Capacitor 1	B32778Z8906	90 μF	0.0035 **Ω**
Capacitor 2	B32778Z8756	50 μF	0.0043 **Ω**
Diode	APT10SCD120B	1200V	0.05 **Ω**
Switch	5SN0750G650300	1200V	0.012 **Ω**

$$\frac{\hat{V}_o}{\hat{d}} = \frac{a_3 s^3 + a_2 s^2 + a_1 s + a_0}{b_4 s^4 + b_3 s^3 + b_2 s^2 + b_1 s + b_0} \tag{4.1}$$

Table 4.3: Control-to-output voltage transfer function coefficient

Coefficient	**Value**
a_3	6217
a_2	$2.891 * 10^{10}$
a_1	$-3.922 * 10^{13}$
a_0	$1.858 * 10^{17}$
b_4	1
b_3	8996
b_2	$4.856 * 10^{7}$
b_1	$6.995 * 10^{10}$
b_0	$1.66 * 10^{14}$

The output voltage control of the converter can be achieved with a proportional-integral (PI) controller. To control the output voltage, the PI controller is used to achieve the required system step response. The system's step response and bode plot are obtained to see the system's behavior and to compare the system's step response before and after using the controller.

Several control techniques are used to tune the designed controller to improve system transient response. For example, the Ziegler-Nichols, Tyreus Luyben, and pole placement methods [72] are used to obtain a proper gain for the designed controller to achieve the desired step response within a proper gain margin that keeps the closed-loop system stable. To get the desired closed-loop response, the overall system should satisfy the following frequency domain design specifications [73]:

The equation that defines system phase margin is:

$$Arg\left(G_c(j\omega_{gc})G_p(j\omega_{gc})\right) + \pi - \phi_m = 0 \tag{4.2}$$

Where G_c, G_p are the controller and plant transfer functions.

Gain crossover frequency specification:

$$\left|G_c(j\omega_{gc})G_p(j\omega_{gc})\right| - 1 = 0 \tag{4.3}$$

Robustness to overall system gain fluctuation the phase of the open-loop system is described as follow:

$$\frac{d}{d\omega} Arg\left(G_c(j\omega_{gc})G_p(j\omega_{gc})\right)\Big|_{\omega=\omega_{cg}} \tag{4.4}$$

To dismiss high-frequency noise, a closed-loop system should contain a small magnitude at high frequencies:

$$\left|T(j\omega) = \frac{G_c(j\omega)G_p(j\omega)}{1 + G_c(j\omega)G_p(j\omega)}\right| \leq A\ dB\ \forall\ \omega \geq \omega_t \tag{4.5}$$

Where A is the desired noise attenuation for frequencies $\omega \geq \omega_t$

Furthermore, to eliminate output disturbances:

$$\left|S(j\omega) = \frac{1}{1 + G_c(j\omega)G_p(j\omega)}\right| \leq B\ dB\ \forall\ \omega \leq \omega_s \tag{4.6}$$

However, the proposed system controller is tuned using pole placement through MATLAB to achieve the above-mentioned frequency-domain requirements. A MATLAB tool uses the system transfer function to obtain the Root Locus of the system. Then the controller pole and zero are located on the LHP in Root Locus, enhancing the overall system response until the desired step response is achieved. The controller is designed to achieve a critically damped step response without overshoot and a maximum settling time of 0.02s.

Figure 31 shows the step response of the open loop transfer function. However, Figure 32 illustrates the MATLAB tool used to specify the gains of the controllers and the closed-loop system step response along with the bode plot.

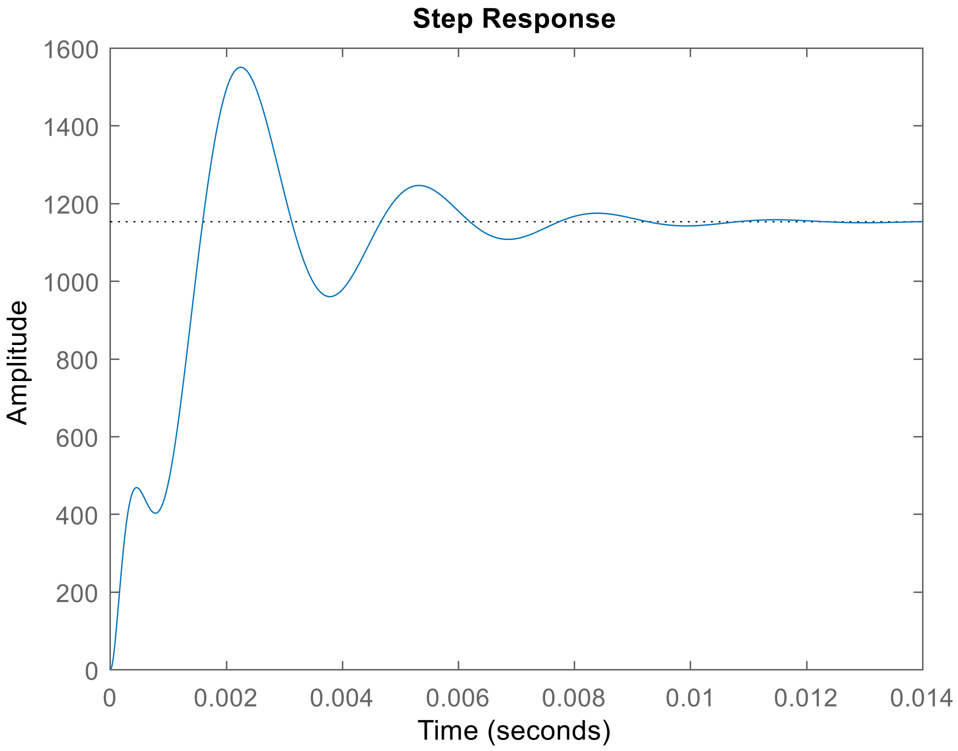

Figure 31: Step response of open loop control-to-output voltage transfer function.

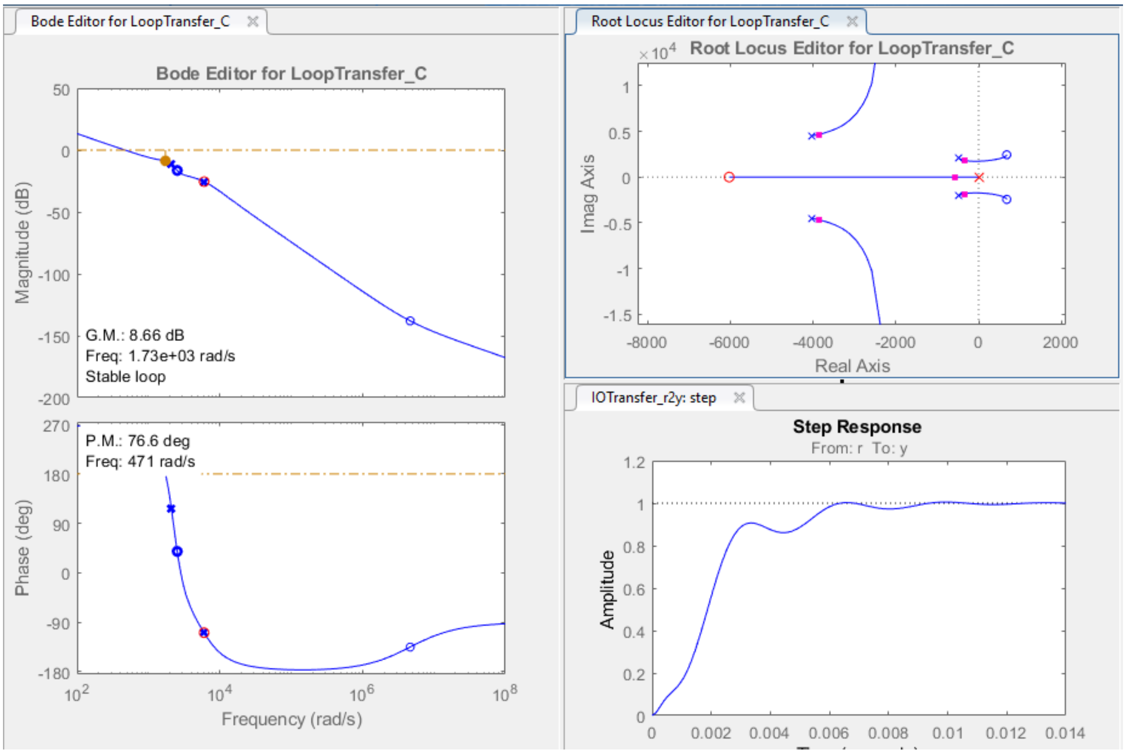

Figure 32: Closed-loop control-to-output voltage system step response, bode plot, and root locus

Table 4.4: Closed loop control-to-output voltage step response parameters

Parameters	**Specifications**
Overshoot	0%
Settling time	$0.018\ s$
Rise Time	$0.006\ s$
Proportional Gain	$6.8 * 10^{-5}$
Integral Gain	0.41
Bandwidth	275 Hz

It can be seen from Figure 32 and Table 4.4 that the closed-loop system step response has a rise time of 0.006s, settling time of 0.018s, and a bandwidth of 275 Hz. In addition, the obtained gain margin of the closed-loop is 8.66dB which keeps the system stable.

This can be increased by decreasing the integral gain that increases the settling time of the closed-loop response. Therefore, using the PI controller with the specified gains to control the output voltage satisfies the design requirement.

4.2 Control-to-Output Current of Cuk Converter

In control-to-output current, the linearized model of the Cuk converter is obtained using the state-space model with slight modifications in the output matrix of the model shown in (4.7).

$$C_{avg} = \left[0 \quad \frac{1}{R_o}\left(\frac{R_o r_{c2}}{R_o + r_{c2}}\right) \quad 0 \quad \frac{1}{R_o}\left(\frac{R_o}{R_o + r_{c2}}\right)\right] \tag{4.7}$$

The resulting control-to-output current transfer function is shown in (4.8).

$$\frac{\hat{I}_o}{\hat{d}} = \frac{a_3 s^3 + a_2 s^2 + a_1 s + a_0}{b_4 s^4 + b_3 s^3 + b_2 s^2 + b_1 s + b_0} \tag{4.8}$$

Table 4.5: Control-to-output Current transfer function coefficients

Coefficient	**Value**
a_3	2578
a_2	$1.199 * 10^{10}$
a_1	$-1.213 * 10^{13}$
a_0	$8.302 * 10^{16}$
b_4	1
b_3	9001
b_2	$4.844 * 10^{7}$
b_1	$6.863 * 10^{10}$
b_0	$1.849 * 10^{14}$

In control-to-output current, the closed-loop system is designed to ensure that the system delivers a certain amount of current to the load. In battery charging applications, several methods are used to control battery charging through current, such as negative pulse charging pulsed current charger, and constant current control. The constant current charging method ensures stable onboard battery charging. The same parameters used in Table 4.1 and Table 4.2 are used to design the control-to-output current closed-loop system. The amount of output current is calculated based on market products. Tesla and Porsche are now producing 100kWh battery packs with a rated voltage of 900V [74]. Therefore, based on these numbers, the amount of current that needs to charge the battery is set to 111.1A.

As done in the control-to-output voltage, a linear PI controller is used to stabilize the system step response and make it critically damped with a maximum settling time of 0.02s.

Figure 33 shows the step response of the open loop control-to-output current transfer function. However, Figure 34 shows the closed-loop system step response, bode plot, and the specified controller gains through pole placement in Root Locus.

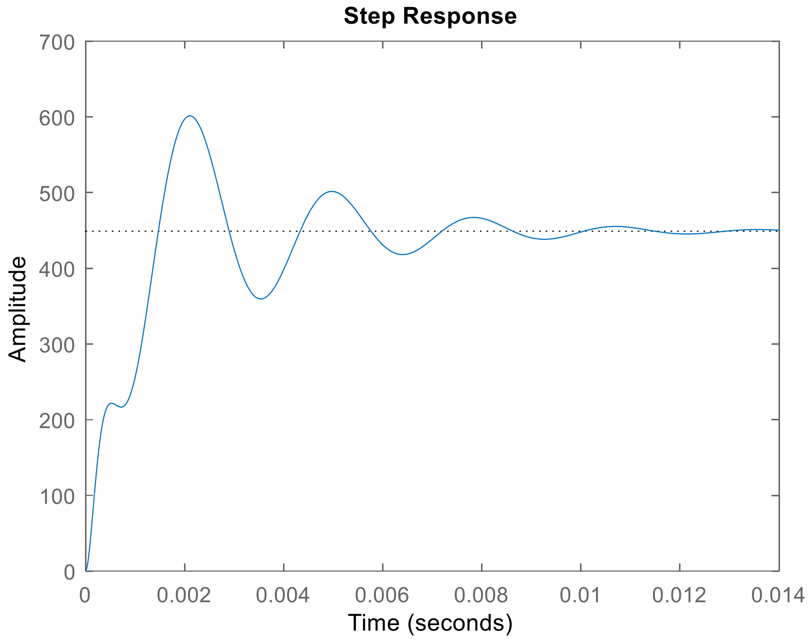

Figure 33: Step response of open loop control-to-output current transfer function

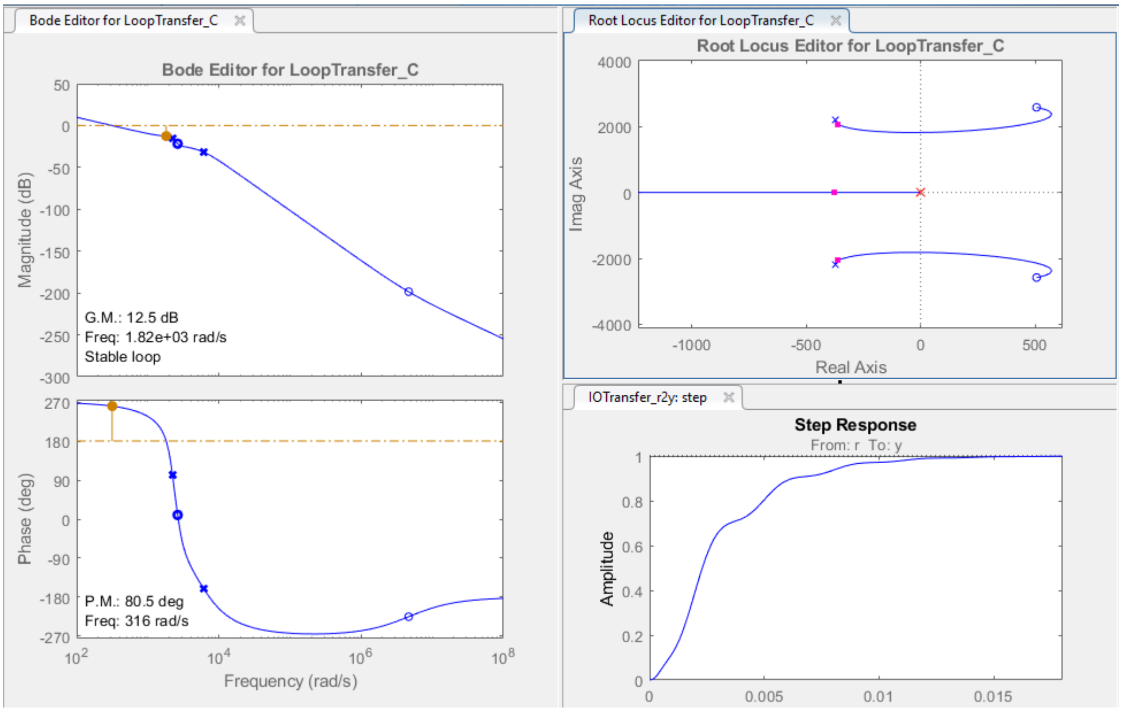

Figure 34: Closed-Loop control-to-output current system step response, bode plot, and root locus.

Table 4.6: Closed loop control-to-output current step response parameters

Parameters	**Specifications**
Overshoot	0%
Settling time	$0.015\ s$
Rise Time	$0.005\ s$
Proportional Gain	$1.68 * 10^{-12}$
Integral Gain	0.7
Bandwidth	$290\ Hz$

It is clear from Figure 34 and Table 4.6 that the closed-loop system has a bandwidth of 290 Hz, as well as the step response of the output-to-current control closed-loop system has almost the same rise time and settling time of the control-to-output voltage system. Also, from the bode plot using the specified PI gains, it can be seen that the closed-loop gain margin is 12.5 dB. However, this margin can be increased at the cost of increasing the settling time of the step response. Thus, using the PI controller with the specified gains, the output current control satisfies the design requirement.

Considering that the proposed system could vary based on the operating condition on how many modules are running, the controller should be robust against these variations that might result in plant variation. Therefore, The FO controllers have the advantage of being robust against plant variation over the conventional order controllers [75], [76]. The FO controllers are discussed and tested in the upcoming sections.

4.3 Fractional Order Calculus

In the last decades, fractional calculus has been used widely in control systems. It ensures system stability due to their robustness towards plant gain variations and uncertainties [77]. Design specifications such as gain and phase margin in fractional-order systems have more flexibility than integer order systems.

Recently, much researches have been done on fractional order controller for DC-DC converters. In [78], a fractional-order controller was designed for a boost converter for PEMFC application. The study [78] compares integer-order and fractional-order PID controllers. Using a fractional-order controller, the start-up voltage shows a smaller overshoot and fewer oscillations than integer-order controllers. Moreover, the noise is reduced in the fractional-order controller as well as it has a faster compensation time when the load is changing. Using fractional-order shows better performance when power has a step change compared with integer-order controllers. Another study [79] used the fractional-order sliding mode control in PV closed loop system emulator. The study showed that the fractional-order controllers have a closer model of an actual PV compared to the conventional sliding mode controller. The model was based on different parameters such as P-I, P-V, and I-V characteristics. The error in the classical model of sliding mode control is almost double when compared to the fractional-order method.

Fractional calculus generalizes differentiation and integration to new non-integer order fundamental operator using an int denoted by ${}_aD_t^r$ [76]. Equation (4.9) can define the operator:

$$ {}_aD_t^r = \begin{cases} \dfrac{d^q}{dt^q} & q > 0 \\ 1 & q = 0 \\ \displaystyle\int_a^t (d\tau)^{-q} & q < 0 \end{cases} \tag{4.9} $$

Where a and t are the lower and upper limit of integrations, respectively, and q is the order of fractional integration or differentiation. The commonly used definitions of fractional calculus are Riemann-Liouville, Grunwald-Lentnikov, and Caputo [76].

Riemann-Liouville defined fractional calculus in (4.10):

$$ {}_aD_t^r f(t) = \frac{d^q f(t)}{d(t-a)^q} = \frac{1}{\Gamma(n-q)}\frac{d^n}{dt^n}\int_0^t (t-\tau)^{n-q-1} f(\tau)d\tau \tag{4.10} $$

Where n is the first integer $n-1 \leq q \leq n$, and the gamma function is given by :

$$ \Gamma(z) = \int_0^\infty t^{z-1}e^{-t}dt \tag{4.11} $$

Where the Grunwald-Lentnikov definition is given as follow:

$$ {}_aD_t^r f(t) = \frac{d^q f(t)}{d(t-a)^q} = \lim_{h\to 0}[\frac{t-a}{N}]^{q}\sum_{j=0}^{N-1}(-1)^j\binom{q}{j} f(t-j[\frac{t-a}{N}]) \tag{4.12} $$

The Laplace transform of Riemann-Liouville is given by:

$$ LT\left\{{}_0D_t^r f(t)\right\} = s^q F(s) - \sum_{k=0}^{n-1} s^k \, {}_0D_t^{q-k-1} f(0) \tag{4.13} $$

$$ n-1 < q \leq n \in N $$

4.3.1 Fractional Order Controller

Control systems have been widely explored and redesigned using fractional calculus to improve the control methods, system modeling, and dynamic response. The advantage of using fractional order controller over integer order controller can be summarized in the following points [75], [76]:

- Robust control system against plant variations such as elements parameters and temperature variations.
- Extra degree of freedom as it allows to have fractional and integer order of the integral and derivatives.

The general transfer function of fractional order PID controller in Laplace domain is:

$$ G_c(s) = K_p + K_i\frac{1}{s^\lambda} + K_d\, s^\mu \tag{4.14} $$

Where K_p, K_i, K_d are proportional, integration and differentiation gains, and λ, μ are arbitrary real numbers. Due to this diversity of controller parameters, control performance can be enhanced [80].

It is essential to ensure a high-performance robust, and stable plant by adequately designing the controller. An FOPI controller for the Cuk converter is tuned in the proposed system by changing the integral order to enhance the overall system response compared to the classical PI controller designed previously. The tuned parameters of the controller are presented in Table 4.7:

Table 4.7: Designed controllers parameters

Controller	Kp	Ki	λ
PI	$1.68 * 10^{-12}$	0.7	1
FOPI	$1.68 * 10^{-12}$	0.7	0.98

Theoretically, the FOPI controller has a shorter rise and settling time when it is compared to the conventional PI controller. This is verified using the mathematical model in Simulink when simulating both controllers with the same gains but with different integral and differential orders. The simulated blocks in Simulink and step response are presented in Figure 35 and Figure 36, which indicates that the FOPI has a faster response with 0.001s when it is compared to the conventional PI.

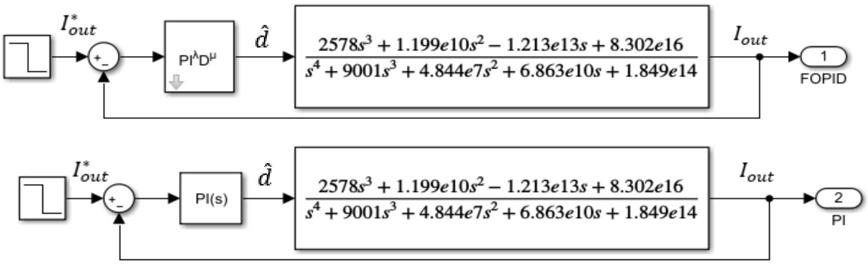

Figure 35: Closed-loop system simulation using FOPI and PI controllers

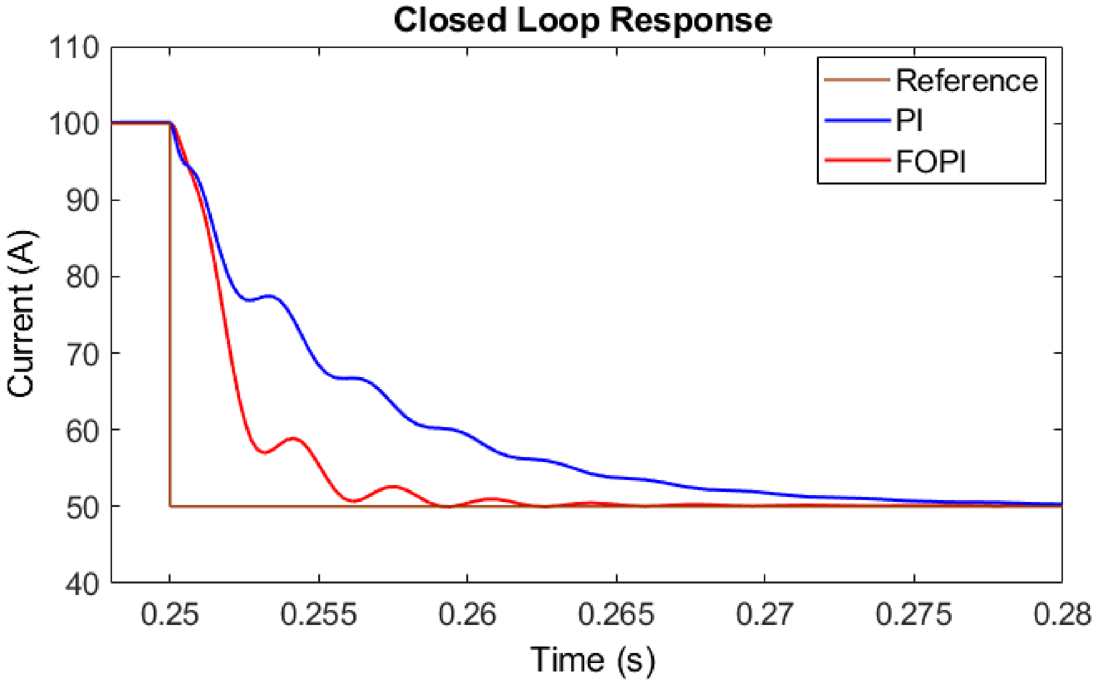

Figure 36: Closed loop system step response comparison FOPI vs PI

4.3.2 Fractional Order Approximation:

Since the fractional-order inverse Laplace transform does not exist, it is not possible to estimate the exact time response of such systems [81]. Therefore, many researchers attempted to obtain other forms of rational approximation to the fractional-order Laplacian integro-differential operators. For example, the FOPID controller can be transferred into an equivalent integer order system that emulates the same behavior of the fractional-order controller [82], [83]. Such approximation can translate the system into an integer order transfer function within a limited frequency band.

4.3.3 Integro-Differential Approximation:

Several methods are used to translate the fractional order controller into the integer-order controller, such as Oustaloup, Matsuda, and biquadratic [84], where realizing the fractional elements depends only on the order of the integrator or differentiator [84]. For example, El-Khazali approximation utilizes biquadratic models considering flat phase response at its center frequency to approximate the integral-differential operators $s^{\pm\alpha}$

where $0 < \alpha < 1$, within a narrower bandwidth. Considering several 2nd-order approximation, biquadratic transfer functions are cascaded [85].

$$\left(\frac{s}{\omega_g}\right)^{\alpha} = \prod_{i=1}^{n} H_i(s/\,\omega_i) = \prod_{i=1}^{n} \frac{N_i(\frac{s}{\omega_i/\omega_g})}{D_i(\frac{s}{\omega_i/\omega_g})} \tag{4.15}$$

Using (4.19), El-Khazali fractional derivative operator can be approximated as [85]:

$$s^{\alpha} \approx T\left(\frac{s}{\omega_c}\right) = \frac{a_0\left(\frac{s}{\omega_c}\right)^2 + a_1\left(\frac{s}{\omega_c}\right) + a_2}{a_2\left(\frac{s}{\omega_c}\right)^2 + a_1\left(\frac{s}{\omega_c}\right) + a_0} \tag{4.16}$$

Where ω_c is the center frequency and a_n are constants calculated using:

$$a_0 = \alpha^{\alpha} + 3\alpha + 2$$

$$a_2 = \alpha^{\alpha} - 3\alpha + 2$$

$$a_1 = (\mathrm{a}_2 - a_0)\tan\left(\frac{(2+\alpha)\pi}{4}\right) = 6\alpha\tan\left(\frac{(2-\alpha)\pi}{4}\right) \tag{4.17}$$

Using the above approximation method, a MATLAB code in appendix A approximates the FOPI controller. The approximated transfer function of the FOPI controller is shown in Table 4.7 and

Table 4.8:

Table 4.8: Fractional-order approximated transfer function

Fractional-Order Transfer Function	**Approximated Transfer Function**
$\frac{1}{s^{\alpha}}$	$\frac{a_6s^6 + a_5s^5 + a_4s^4 + a_3s^3 + a_2s^2 + a_1s + a_0}{b_6s^6 + b_5s^5 + b_4s^4 + b_4s^4 + b_3s^3 + b_2s^2 + b_1s + b_0}$

Table 4.9: Control-to-output Current transfer function coefficient for $\alpha = 0.98$

Coefficient	$\mathbf{\frac{1}{s^{0.98}}}$
a_6	$8.45 * 10^{-6}$
a_5	69.72
a_4	$2.828 * 10^{6}$
a_3	$5.581 * 10^{8}$
a_2	$5.463 * 10^{8}$
a_1	$2.602 * 10^{6}$
a_0	61.18
b_6	61.18
b_5	$2.602 * 10^{6}$
b_4	$5.463 * 10^{8}$
b_3	$5.581 * 10^{8}$
b_2	$2.828 * 10^{6}$
b_1	69.72
b_0	$8.45 * 10^{-6}$

The FOPI controller is approximated and verified through simulation with $\alpha = 0.98$ for the integral operator. The closed-loop step response of the system using approximated FOPI and actual FOPI are obtained and then compared as shown in Figure 37.

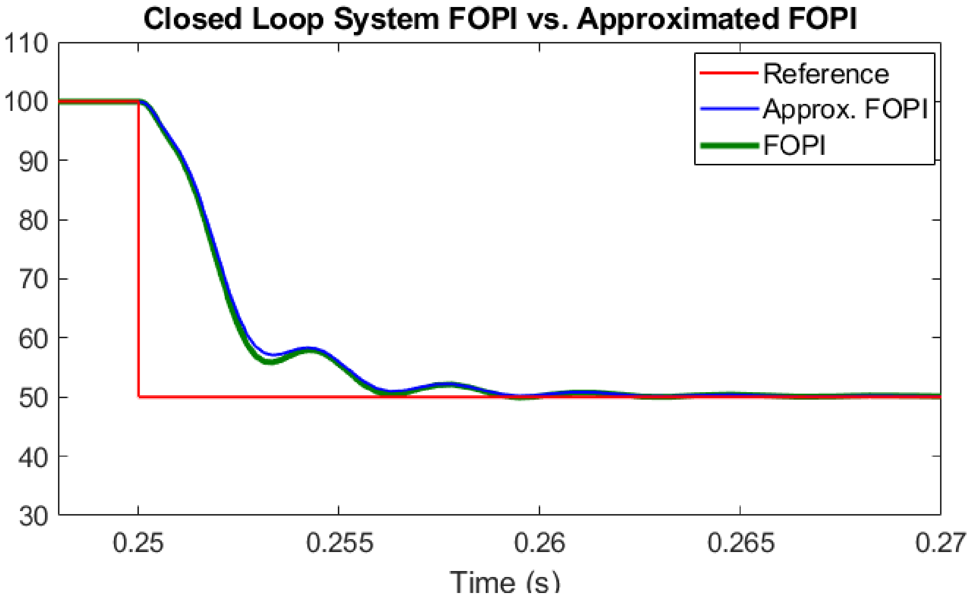

Figure 37: System step response using FOPI and approximated FOPI controllers

It can be seen from Figure 37 that the approximated system has almost the same response as the actual FOPI controller. This gives the ability to deal with the FOPI as an integer-order transfer function. Thus, the inverse Laplace of the controller can be obtained and analyzed, as well as it can be discretized and used in digital control. However, the used biquadratic approximation method has a limited frequency band, and it can be used for $0 < \alpha < 1$ which limits the FOPI tuning range.

4.4 Control-to-Output Current in Z-domain

Digital control provides an efficient integration between hardware and software. By converting from continuous time to discrete time, the digital signal can be used as an input to a computer. Thus, to make the proposed design practical, the continuous control system has to be converted into a discrete system to apply digital control. Given that the system operates at a switching frequency of $20kHz$ where the digital system would have close behavior to the continuous system. Therefore, digital control is highlighted to consider higher power rating systems that could utilize the same topology with lower switching frequency.

Several methods can be used to discretize the plant or the controller, such as backward difference methods, forward difference methods, bilinear or Tustin transformation, impulse-invariance method, step-invariance method, and pole-zero matched method. However, the Tustin method has a proper match between continuous-time and discrete-time domains. Therefore, the Tustin method is used to describe either the plant or the controller, where the discretization can be done using (4.18):

$$s = \frac{2}{T}(\frac{z-1}{z+1}) \tag{4.18}$$

The closed loop system is then discretized using (4.18), and the sampling time used is $\frac{1}{f_{sw}} = T = 0.00005\ s$. The resulted transfer functions in Z-domain are shown in Table

4.10 and

Table 4.11.

Table 4.10: Discretized systems transfer function

Discretized Transfer Function	Approximated Transfer Function
$G_c(z)$	$\frac{a_1 z + a_0}{b_1 z + b_0}$
$G_{cFOPI}(z)$	$\frac{a_6 z^6 + a_5 z^5 + a_4 z^4 + a_3 z^3 + a_2 z^2 + a_1 z + a_0}{b_6 z^6 + b_5 z^5 + b_4 z^4 + b_3 z^3 + b_2 z^2 + b_1 z + b_0}$
$G_p(z)$	$\frac{a_4 z^4 + a_3 z^3 + a_2 z^2 + a_1 z + a_0}{b_4 z^4 + b_3 z^3 + b_2 z^2 + b_1 z + b_0}$

Table 4.11: Discretized transfer function coefficients

Coefficient	$\boldsymbol{G_{cFOPI}(z)}$	$\boldsymbol{G_c(z)}$	$\boldsymbol{G_p(z)}$
$\boldsymbol{a_6}$	0.0001067	0	0
$\boldsymbol{a_5}$	-0.0004966	0	0
$\boldsymbol{a_4}$	0.000917	0	5.89
$\boldsymbol{a_3}$	-0.0008363	0	-0.3011
$\boldsymbol{a_2}$	0.000372	0	-11.77
$\boldsymbol{a_1}$	$-6.04 * 10^{-5}$	0.00041	0.5075
$\boldsymbol{a_0}$	$-2.401 * 10^{-6}$	-0.00039	6.089
$\boldsymbol{b_6}$	1	0	0
$\boldsymbol{b_5}$	-4.961	0	0
$\boldsymbol{b_4}$	9.817	0	1
$\boldsymbol{b_3}$	-9.656	0	-3.54
$\boldsymbol{b_2}$	4.677	0	4.728
$\boldsymbol{b_1}$	-0.8495	1	-2.827
$\boldsymbol{b_0}$	-0.02794	-1	0.6401

The closed-loop system is simulated in Simulink to analyze the effectiveness of the selected discretization method on the system behavior. Figure 39 and Figure 41 illustrate the step response of the closed-loop system in the Z-domain, representing the effectiveness of the bilinear transform (Tustin's method), showing a proper matching between discrete-time and continuous-time step response.

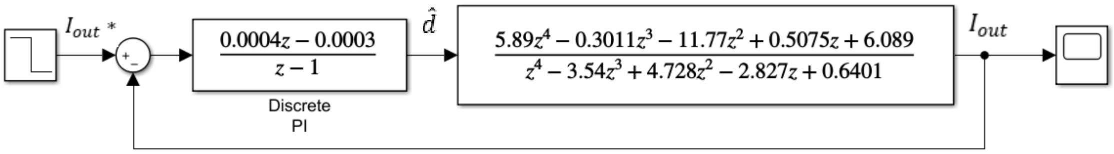

Figure 38: Closed loop discretized system using PI controller simulation blocks

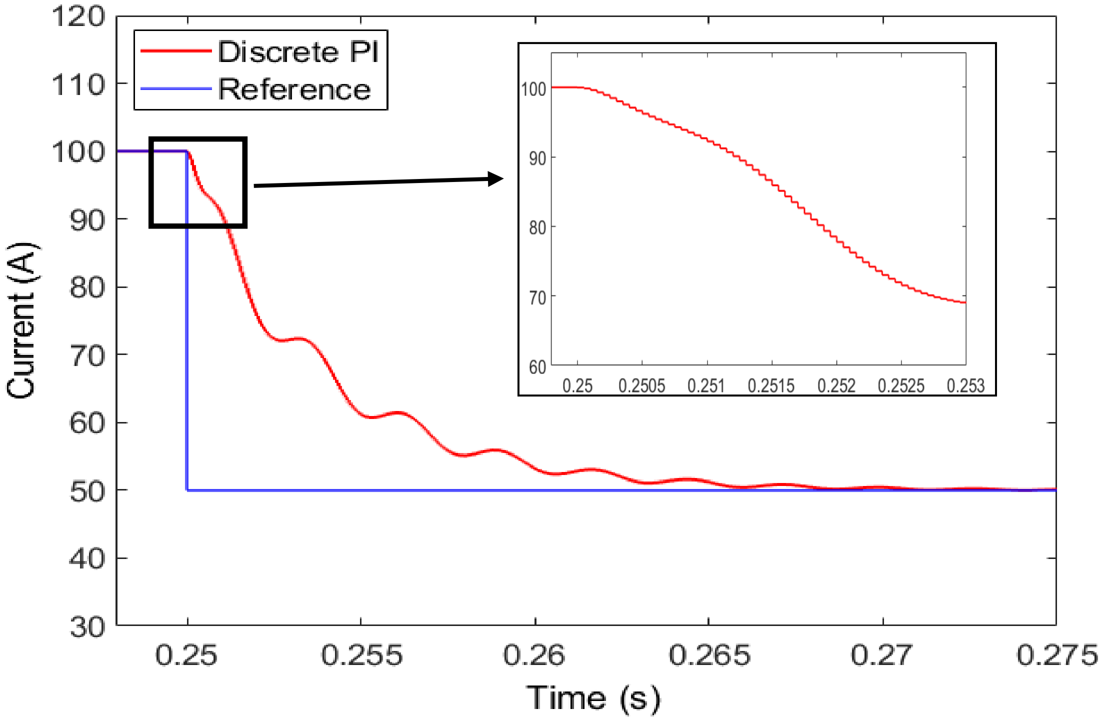

Figure 39: Step response of discretized system using conventional controller

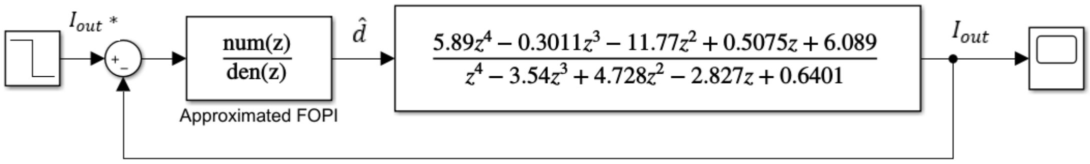

Figure 40: Closed loop discretized system using FOPI controller simulation blocks

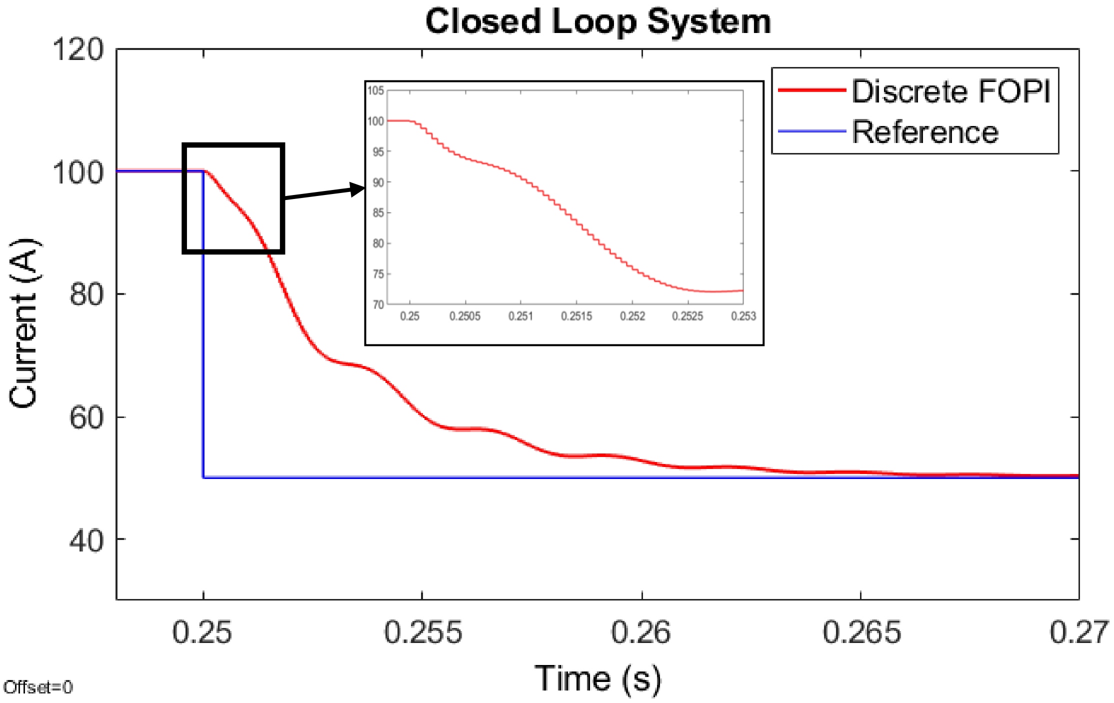

Figure 41: Step response of discretized system using FOPI controller

4.5 Equal Power Sharing in Modular Converters

To ensure reliable operation of the converter regardless of the parameter deviations, a proper closed-loop control needs to be designed that ensures equal power-sharing between the DC-DC converters. This can be achieved by considering some measures such as input current sharing (ICS), input voltage sharing (IVS), output current sharing (OCS), and output voltage sharing (OVS) [41]. ICS is usually considered in input parallel connections to ensure that all the converters share the same input current and distribute the power equally. On the other hand, IVS is considered when an input series connection is used. Since the same current passes throughout the connected converters, the input voltage of each converter should be the same to ensure that the power is distributed equally. However, on the output side, the same concept is applied. In parallel connections, OCS has to be considered, and equal voltage sharing has to be assured for the series output connection. There are several ways to control current and voltage sharing between the converters. In input parallel-connected systems, the ICS can be ensured by either designing an input current controller, which ensures OCS and OVS in IPOP and IPOS connections, or it can be done by designing a current or voltage controller at the output side where it leads to ensure ICS [41].

The control scheme designed for the proposed configuration is a constant current control that provides continuous charging while driving, as shown in Figure 42. The OVS and ICS are achieved when controlling the output current of each converter [41].

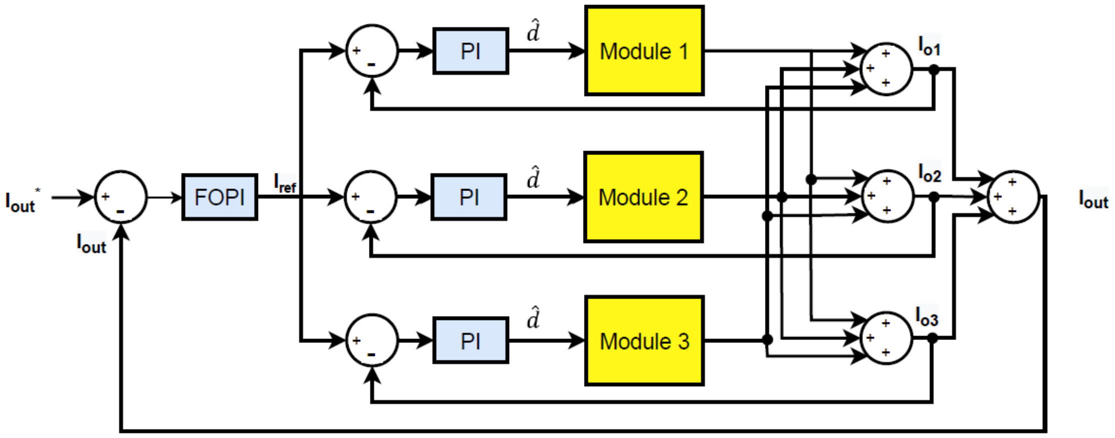

Figure 42: IPOS output current control block diagram.

Figure 42 shows the designed control scheme for the IPOS. It includes two loops, inner and outer loops. The main purpose of these loops is to ensure equal power-sharing between the converters in case of any variations are introduced to the system, such as parameters mismatch and duty cycle disturbance. The inner loops eliminate the mismatch effect by adjusting the converter's duty cycle, which forces the converter to output a certain current compared to the reference. However, the outer loop eliminates the duty ratio disturbance effect since it compensates for the disturbance by changing the other converters' duty ratios that force all the three converters to output the same current.

Three scenarios are simulated to verify the control scheme shown in Figure 42. The first scenario is simulated by removing all the inner loops, where Figure 43 shows that the output current of the converters is not the same, which shows the effect of the converters mismatch on sharing the power between the converters. However, the second scenario is simulated using inner loops that consider the output current of each converter separately without cross feedback and with a disturbance at t=0.25s. Figure 44 shows that the converters share the same output current. However, when the disturbance is introduced to the system, the converters' output currents are diverted, and the power is not equally shared. Afterward, the proposed scheme is then tested, and the result is illustrated in Figure 45. The same disturbance is introduced to the system. The control scheme used maintains the same output currents of the converters, ensuring equal power-sharing even if the disturbance is introduced to the system.

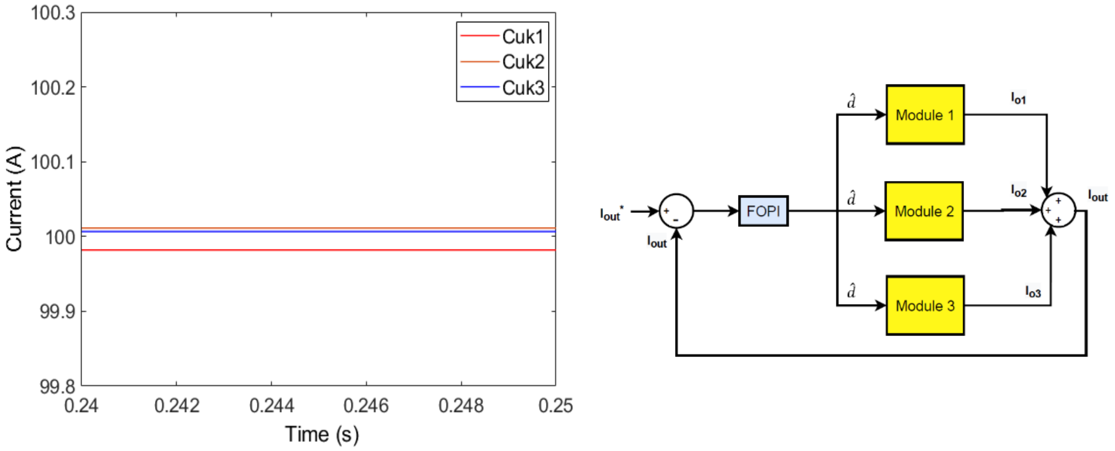

Figure 43: IPOS converters control using outer feedback loop only without inner loop

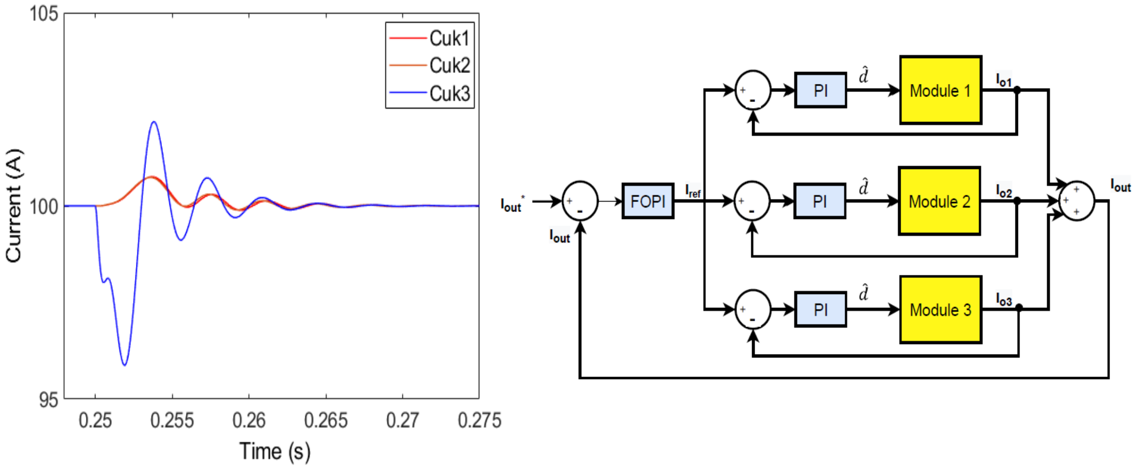

Figure 44: IPOS converters control with inner loops and no cross feedback

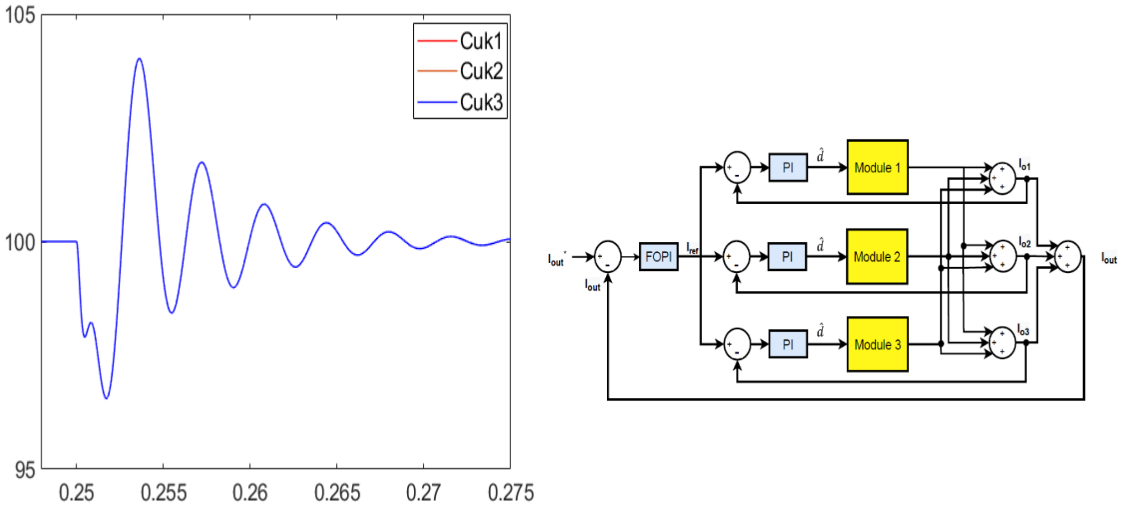

Figure 45: IPOS converters control with combined outer loop and inner loops with cross feedback

4.6 Maximum Power Point Tracking (MPPT) in Fuel Cell

Over the years, many FC equivalent circuits have been proposed, which vary in complexity and accuracy. The equivalent circuit is categorized into two types, dynamic models and passive models. The dynamic models represent the FC behavior under the output electric power state. However, the passive models determine the potential performance and degradation when the FC is on stand-by mode[87], [13]. The dynamic models of PEMFC are discussed in [86], [87],[88]. However, the simplified dynamic electric circuit model based on chemical reactions considering the main losses of the PEMFC shown below is considered in this study[13]:

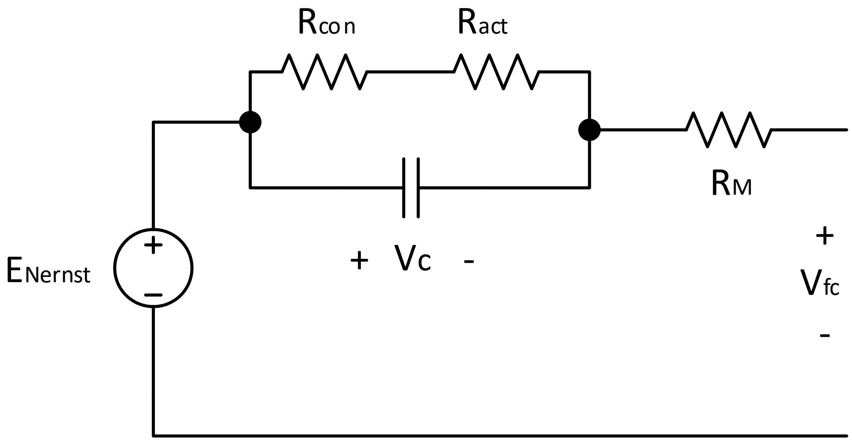

Figure 46. Fuel cell equivalent circuit

The equivalent circuit of the FC consists of the resistance membrane R_m, and two resistors in parallel with the capacitor represent the electron transport phenomena in the anode and cathode. These parameters can be calculated based on the FC chemical parameters. The performance of the FC varies based on the stack voltage v_{st} and the current drawn by the load I_{st}. Which directly influence the generated power by FC stack, where $P_{fc} = v_{st}I_{st}$. Stack voltage can be calculated as the product of the number of cells by the voltage of each cell. $v_{st} = nv_{fc}$. Each cell produces a certain amount of voltage, considering the effect of thermodynamics, kinetics, and ohmic resistance. Therefore, the output voltage of the FC is considered constant since the chemical reaction takes some time to cause a variation in the FC output voltage. FC has a nonlinear behavior where it operates at a nominal point where the maximum power is not extracted in heavy loads in normal conditions. A maximum power point tracking technique is used to obtain the maximum power of the FC. The maximum power point is extracted in order to assure stable and continuous operation of the FC. In fact, the FC behavior varies based on the chemical reaction and the electrical load connected to the cell. Furthermore, the stack connection plays a vital role in extracting the maximum power point. Figure 47 presents the power, current, and voltage characteristics of FC, showing the non-linear behavior of FC.

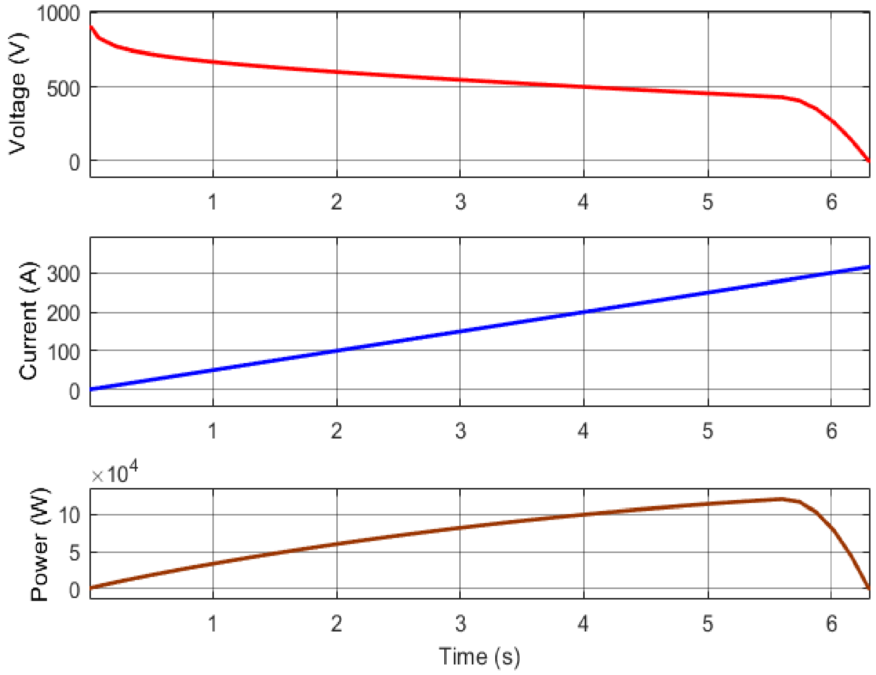

Figure 47. Voltage, current, and power curves of a fuel cell

In general, the FCs can be connected in parallel or in series to form an FC stack. Thus, based on the FCs arrangement, the Stack terminals are classified to be centralized or decentralized. Both designs are discussed in [89]. For the centralized stack shown in Figure 48 (b), the overall FC stack is connected in a single converter where the MPP is extracted and used in the system. On the other hand, the study in [89] showed that using the decentralized system with MPPT shown in Figure 48 (a) is more practical and increases the overall efficiency of the FC operation. The cost of using such a method is that multiple converters need to be connected and integrated with different controllers to achieve the required power, increasing the size and limiting the switching frequency that reflects on the converter elements sizing. As well as a smoothing capacitor is required at each input of the FCs to achieve higher performance.

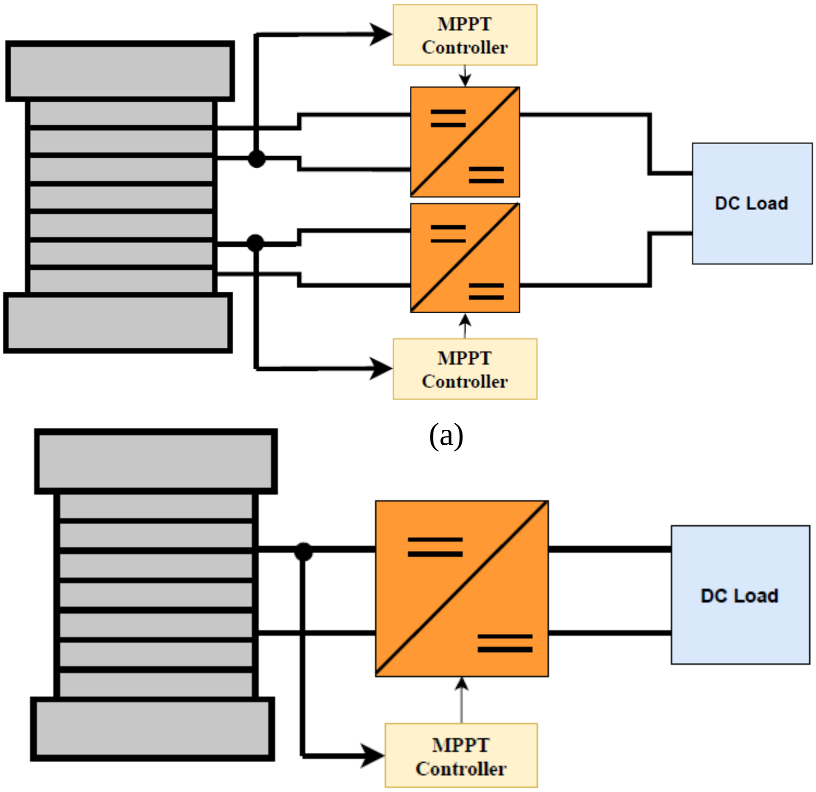

(a)

(b)

Figure 48: (a) Decentralized MPPT system (b) Centralized MPPT system

There are several methods to extract the maximum power point. Based on the V-I curve, the intersection point between the voltage and current of the FC where the maximum power occurs is used as the operating points of the FC [90]. The perturb and observe (P&O) method is done by introducing minor perturbations to cause power variation of the FC. In this method, the power oscillates around the maximum power point, but it never reaches the maximum power [91]. The incremental conductance (InC) method overcomes the disadvantage of the P&O in tracking the maximum power under fast changes. The direction in which the MPPT should move can be calculated using the relationship between $\frac{\Delta I}{\Delta V}$ and $\frac{-I}{V}$. This relation is derived from the fact that $\frac{\mathrm{d}P}{\mathrm{d}V}$ is negative when the MPPT is to the right of the MPP. However, when it is positive, that means the MPPT is to the left of the MPP [91]. This algorithm determines when the maximum power point is reached while the P&O will keep oscillating around the maximum point.

4.7 Overall System Design and Simulation

To verify the above-mentioned theory, MATLAB/Simulink is used to simulate the overall system using the PEMFC model available in Simulink with a maximum power of 120kW. Table 4.12 presents the simulated values of the designed elements used per converter:

Table 4.12: Simulated values of designed Cuk converter elements (per converter)

Parameters	**Specifications**
L_1	1 mH
L_2	0.5 mH
$C_1(P/S)$	180 μF
C_2	50 μF
R_o	3.2 Ω

To test the efficiency of the controller in balancing the power between the converters when dealing with elements uncertainties, the components for each module were modified with a small tolerance, as presented in Table 4.13:

Table 4.13: IPOS converters parameters

Parameters	**Cuk 1**	**Cuk 2**	**Cuk 3**
Rated Input Power ($\boldsymbol{P_i}$)		40k W	
Rated Output Power ($\boldsymbol{P_o}$)		40kW	
Input Voltage ($\boldsymbol{V_i}$)		430 V	
Output Voltage ($\boldsymbol{V_o}$)		333.3 V	
Input Current ($\boldsymbol{I_i}$)		93.3 A	
Output Current ($\boldsymbol{I_o}$)		108 A	
Input Inductor ($\boldsymbol{L_1}$)	0.9mH	1 mH	1.1mH
Output Inductor ($\boldsymbol{L_2}$)	1.1mH	1 mH	0.9mH
Input capacitors ($\boldsymbol{C_1}$ ($\boldsymbol{P/S}$))	164 μF	180 μF	198 μF
Output Capacitors ($\boldsymbol{C_2}$)	90 μF	100 μF	95 μF

The overall model is verified and examined using the output voltage and current to examine the power conversion of the designed system. Meanwhile, the output voltage and input current per converter are used to test the power balancing control. Also, input voltage and input current are used to see the MPPT method effect on the FC.

4.8 Simulation Results for Conventional Control to Output Current

The simulation is run for the designed three converters to illustrate the essential parameters mentioned earlier. The main variables in the closed-loop system operation are presented in the following figures.

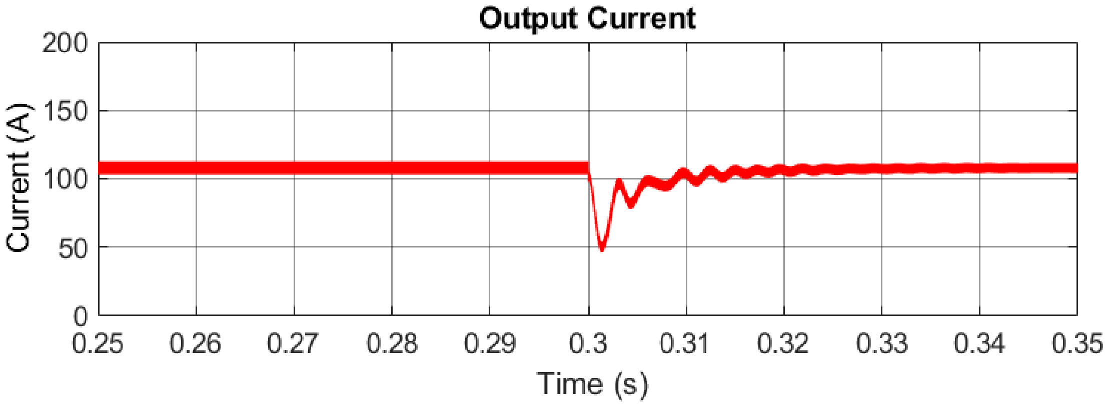

Figure 49: Overall system current, one converter removed at t=0.3s.

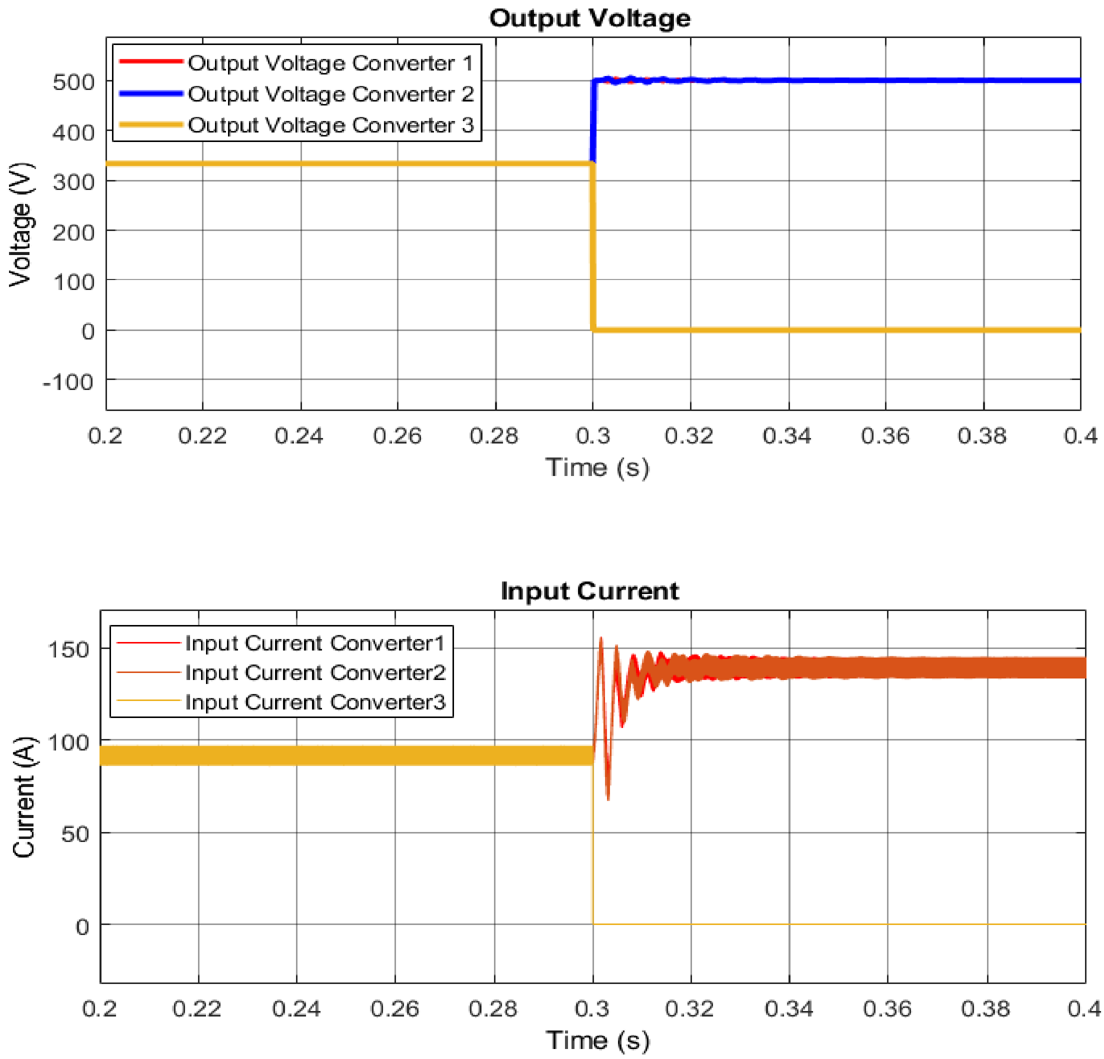

Figure 50: Input currents and output voltages sharing of the IPOS Cuk converters (ICS), (OVS), one converter removed at t=0.3s.

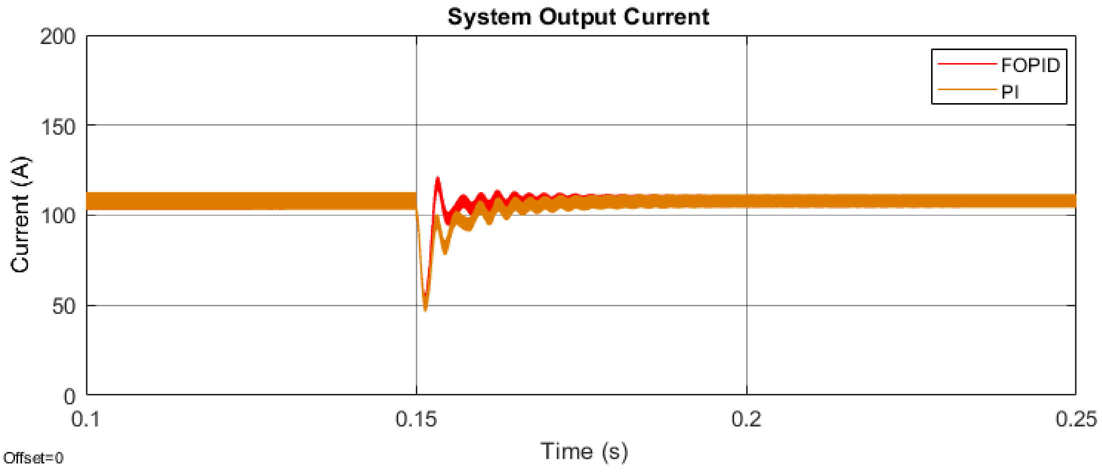

Figure 51: IPOS system using PI and FOPI controllers

Figure 49 and Figure 50 show the results of the simulated system using three IPOS isolated Cuk converters. Figure 49 shows that the amount of power delivered to the battery is constant even if one of the converters is faulty, where a simulated fault is introduced to the system at t=0.3s by bypassing one of the converters. Furthermore, Figure 50 shows the equal power-sharing among the three converters. The series connection at the output side maintains the output voltage constant, and the parallel connection at the input side ensures equal current sharing between the converters. Also, when the system is interrupted, it can be seen that the power is shared between the two running converters. In addition, the FOPI controller is then tested on the proposed topology using three input-parallel output-series Cuk converters. The system behavior is presented in Figure 51.

Chapter 5: DC-DC Converter Performance Assessment

In this chapter, the IPOS Cuk converter's performance is assessed. The gain of a single and three IPOS Cuk converter considering non-idealities with the variation of duty cycles is presented. In addition, the overall efficiency of the IPOS is illustrated with the variation of loading. Then, the sensitivity analysis presents the parasitic resistance effect on the overall gain. The converter power density of the proposed topology is presented, and the FC ripple current in the proposed system is evaluated.

5.1 Cuk Converter Gain Assessment

Using the obtained model in chapter 3 (using (3.9) (3.10)), the converter performance is compared against the ideal model by plotting their gain vs. duty cycle. The derived transfer relation is:

$$\frac{V_o}{V_{in}} = \frac{R(d - d^2)}{\beta_1 d^2 + \beta_2 d + \beta} \tag{5.1}$$

Where

$\beta_1 = R + r_{L1} + r_{L2} - r_{c1}$

$\beta_2 = r_s - r_d + r_{c1} - 2r_{L2} - 2R$

$\beta_3 = R + r_{L2} + r_d$

The parasitic resistances used are mentioned in Table 4.2. Figure 52 shows the gain vs. duty cycle obtained using a fixed load of 100Ω to assess the converter performance.

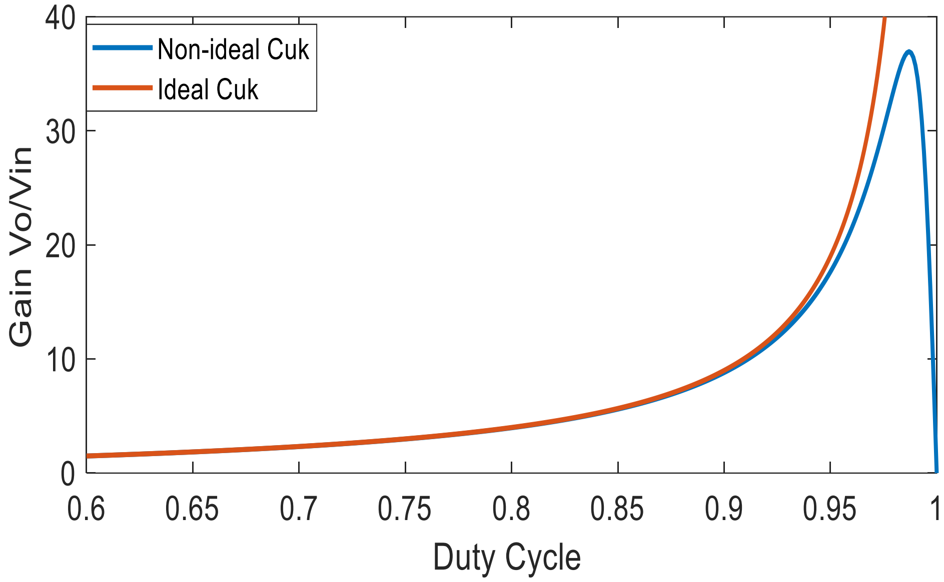

Figure 52: Gain Vs Duty Cycle for both ideal and non-ideal Cuk converter

Figure 52 illustrates the results of ideal and non-ideal Cuk converter gain. For the given parameters of the Cuk elements parasitic resistances, the maximum gain obtained using the derived models was ~39.

5.2 IPOS Cuk Converters Gain Assessment

The derived model is also used in assessing the overall system efficiency of the three IPOS isolated converters. However, for the non-ideal converters, the theoretical efficiency of the converter is obtained using the derived output voltage to input voltage relation. The overall gain of IPOS connection of three DC-DC converters operating at the same duty cycle results in the summation of each converter gain. The advantage of such a connection is that it introduces modularity to the system, reducing the gain requirements. The overall gain of the connected non-ideal model relation for the converters is expressed as follow:

$$\frac{V_o}{V_{in}} = G_1 + G_2 + G_3 \tag{5.2}$$

The efficiency can be approximated by dividing the non-ideal gains over the ideal gain [69], where such an estimate may result in an overestimated efficiency. The efficiency equation of the IPOS three converters is expressed in (5.3):

$$\eta = \frac{G_1 + G_2 + G_3}{3G_{ideal}} \tag{5.3}$$

Figure 53 shows the efficiency of the connected three Cuk converters. As mentioned earlier, the gain of the non-ideal converter deteriorates at high duty cycles. It is clear from Figure 53 that the overall system's efficiency goes below 90% when the duty ratio exceeds 0.95. This is because the equation used to assess the efficiency divides the non-ideal gain over the ideal gain, knowing that the ideal gain tends to infinity at high duty ratios. Moreover, when using multiple converters, the gain is three times higher than a single converter. Therefore, the overall system's efficiency is high and above 98%.

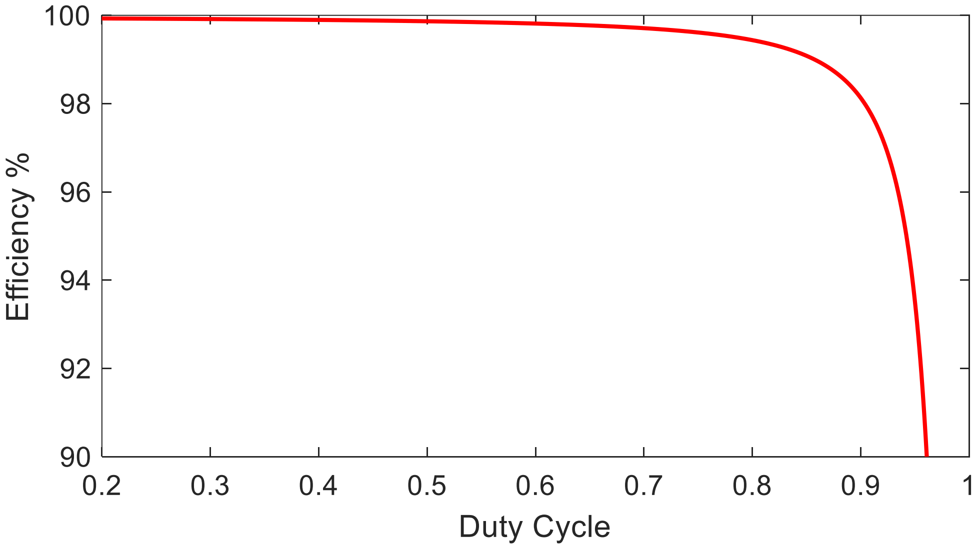

Figure 53: IPOS three Cuk converters efficiency

5.3 IPOS Cuk Converters Sensitivity Analysis

The effect of a small variation of the inductors parasitic resistance for the overall proposed system IPOS gain is elaborated using sensitivity analysis. Since the sensitivity analysis here is related to high-power applications with high current, the effect of parasitic resistance of the inductor has a the major effect on the overall gain; therefore, the following assumptions are made in sensitivity calculations:

1- Converter diodes, capacitors, HFT, and switch losses are neglected.

2- Major parasitic resistances variations are in inductors.

3- Each converter has the same parasitic resistance as the other converters r_L.

Sensitivity of a system Y to variation in input x is expressed as [92]:

$$S_x^Y = \frac{\delta Y/Y}{\delta x/x} = \frac{x}{y}\frac{\delta Y}{\delta x} \tag{5.4}$$

The derived model is modified to maintain the parasitic inductor resistances as the only non-idealities of the system r_{L1}, r_{L2}. The modified transfer model of the Cuk converter using the parasitic resistance of the inductors with respect to the load $r_{L1,2(pu)}$ is presented in (5.5):

$$\frac{V_o}{V_{in}} = \frac{D}{1-D}\frac{(1-D)}{(1-D)\left(r_{L2(pu)}+1\right) + r_{L1(pu)}\left(\frac{D^2}{1-D}\right)} \tag{5.5}$$

Then, using the modified transfer model with respect to parasitic resistance from (5.5), the IPOS connected converters gain is applied to (5.4) to obtain the sensitivity equation. The equations obtained with respect to $r_{L1(pu)}$ and $r_{L2(pu)}$ independently are:

$$S_{r_{L2(pu)}}^G = \frac{-r_{L1(pu)}(D^2)}{r_{L1(pu)}D^2 + (1-D)^2\left(r_{L2(pu)}+1\right)} \tag{5.6}$$

$$S^{G}_{r_{L2(pu)}} = \frac{(-r_{L2(pu)})(D-1)^2}{r_{L1(pu)}D^2 + (1-D)^2\left(r_{L2(pu)}+1\right)} \quad (5.7)$$

Figure 54 and Figure 55 present the sensitivity analysis for the variation in r_{L1} and r_{L2} of the three IPOS Cuk converters, given the assumption that the D=0.9 and both r_L values are 0.001 per unit with respect to the total load.

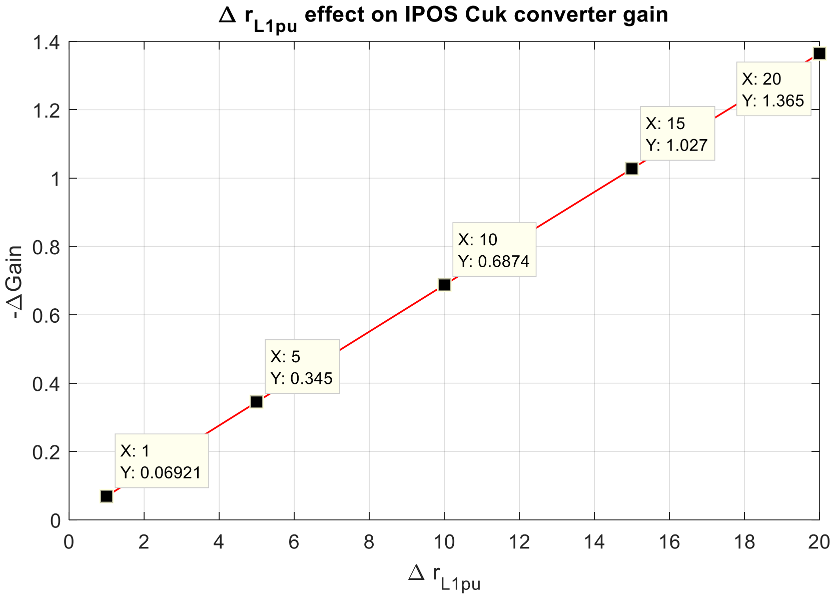

Figure 54: $\Delta r_{L1(pu)}$ effect on IPOS converters gain at D=0.9

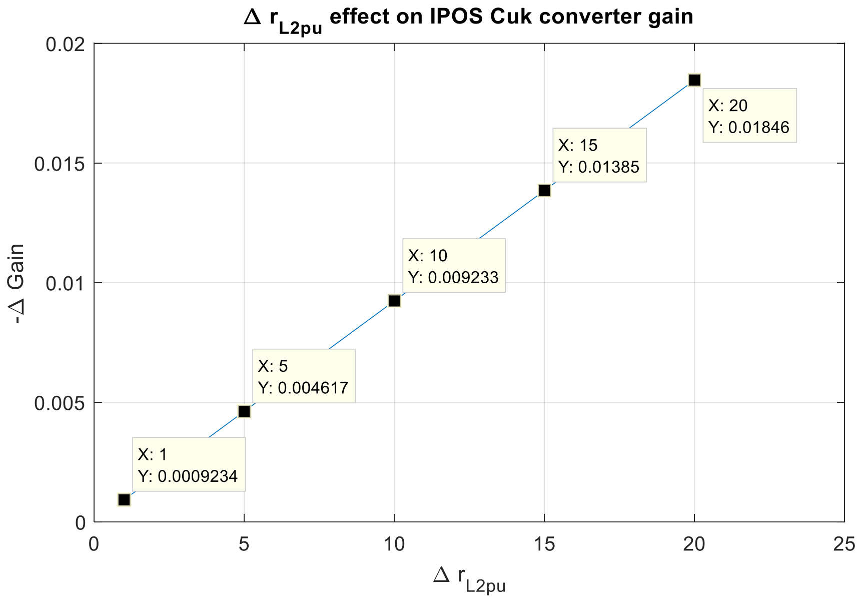

Figure 55: $\Delta r_{L2(pu)}$ effect on IPOS converters gain at D=0.9

From Figure 54 and Figure 55, the main interpretation is that r_{L1} has a significant effect on the gain of the converters, which is considered as one of the main keys of gain deterioration in high power applications. It is clear that the variation of r_{L1} is has more impact than r_{L2} on the gain change at the same per-unit values. When both have a 10% variation of the per-unit value, the gain drop due to r_{L1} is 0.69%. However for that due to r_{L2} is 0.009%.

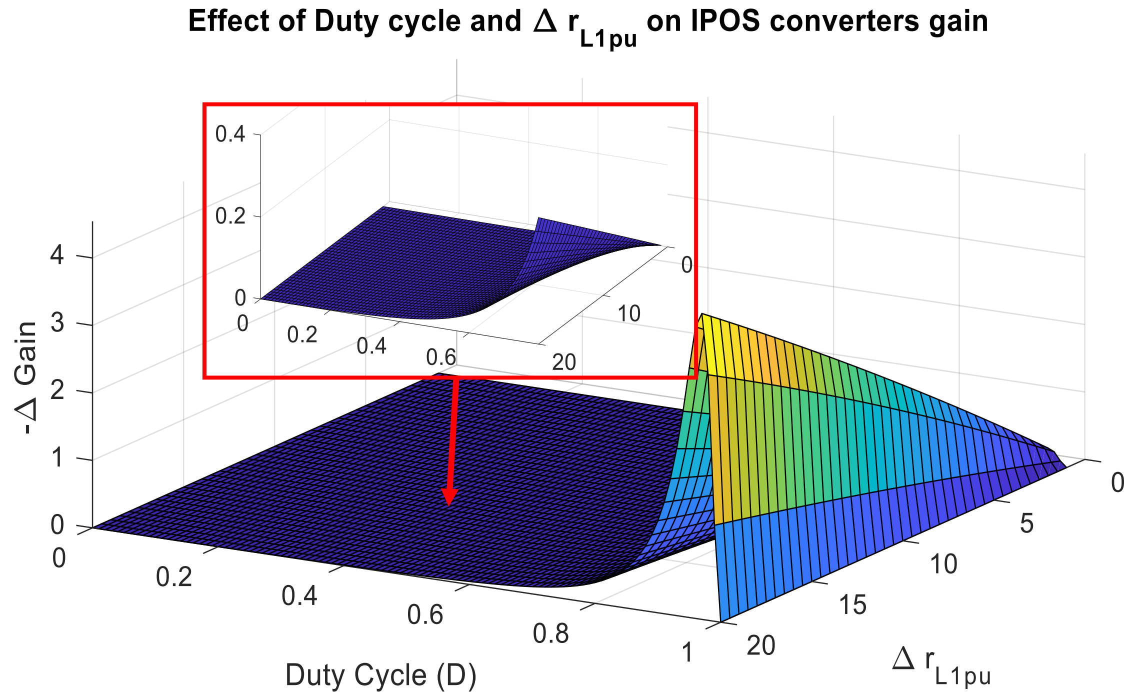

Figure 56: Effect of Duty cycle and $\Delta r_{L1(pu)}$ on the IPOS converters gain

The same variation of the parasitic resistance is applied to the converters with a wider duty cycle range. It can be seen that when the duty cycle increases, the gain drop increases. This is due to the increase of losses as D approaches unity, and when it reaches closer to one, the overall gain approaches zero. This is logical since the converters are operating at extreme duty cycles. Moreover, by comparing the efficiencies obtained at different duty cycles between 0.1 and 1 in the previous sections, the results show that gain drop increases as the duty cycle increases, affecting the overall system efficiency. This is due to the fact of the losses increase at higher duty cycles. However, for duty cycles lower than 0.8, the gain drop did not exceed 0.4 %.

5.4 IPOS Cuk Converter Efficiency

The converter efficiency is one of the performance indices considered in this study. Knowing that the electrical efficiency is the ratio of the output power P_{out} to the input power P_{in}. In FCEV, the FC determines the input power, and the power output is the power after being conditioned at the DC-DC converter considering converter losses. The efficiency of the converter can be expressed in (5.8):

$$\eta = \frac{P_{out}}{P_{in}} = \frac{P_{out}}{P_{out} + P_{loss}}\,.100\% \tag{5.8}$$

Many factors contribute to the converter losses, where the core losses of the HFT, semiconductor switching device, and diode have the highest contribution in converter losses.

Semiconductor switching device has switching and conduction losses. The switching losses occur due to the change of voltage and current waveforms since they have rising and falling slopes. Considering IGBT, the switching losses can be identified as follow:

1- IGBT turn-on energy losses $E_{sw,on}$

2- IGBT turn off energy losses $E_{sw,off}$

Considering the datasheet of IGBT and according to [93], switching losses of the IGBT can be expressed as follow:

$$P_{loss,sw} = \left(E_{sw,on} + E_{sw,off}\right).f_{sw} \tag{5.9}$$

$$P_{loss,sw} = (11.9 + 12.5) * 10^{-3} * 20 * 10^{3} = 488\,W$$

However, the conduction losses occur during conducting period. The power conduction loss can be calculated using the current switch $I_s$as follows:

$$P_{loss,cond} = R_s I_{srms}^2 D + V_{IGBT} I_{savg} \tag{5.10}$$

$$P_{loss,cond} = 0.0012 * 135^2 * 0.45 + 2 * 90 = 190\,W$$

Where R_s is the on state Due to the voltage drop across the diode, diode losses can be estimated:

$$P_{loss,diode} = V_{on}\ I_D \tag{5.11}$$

$$P_{loss,diode} = (1.8)(149) = 268\ W$$

Utilizing HFT introduces some losses at the core of the transformer. Using an HFT from HiMAG, with high efficiency, the transformer losses can be calculated according to the datasheet, which is 1% of the operating power:

$$P_{loss,tran} = 400\ W$$

Afterward, the total losses can be calculated:

$$P_{Loss} = P_{loss,IGBT} + P_{loss,Diode} + P_{loss,tran} = 1346\ W$$

$$P_{rated\ losses} = 3 * 1346 = 4.03\ kW$$

Using (5.8), the converter's efficiency vs. power is illustrated in Figure 57.

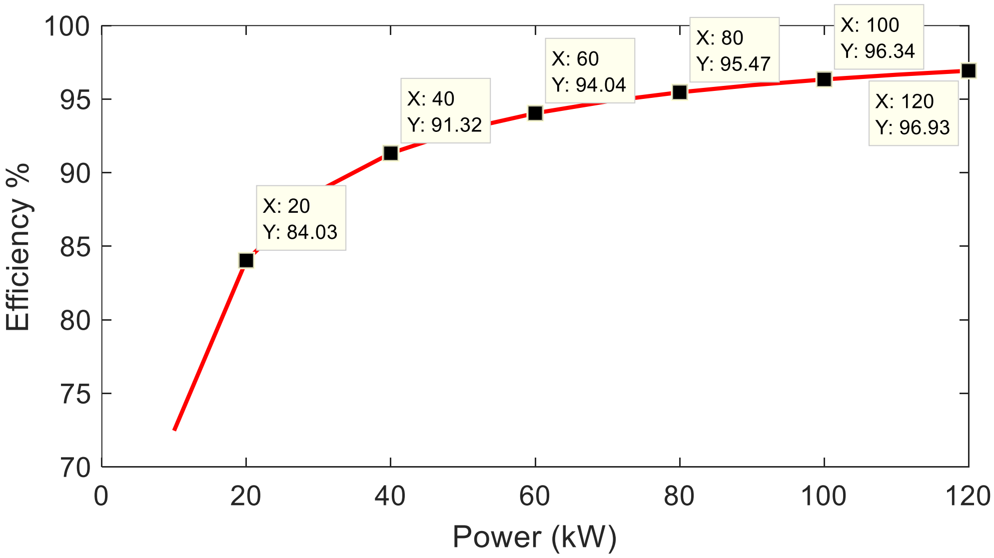

Figure 57: Efficiency vs. total system power of the presented FCEV converter

5.5 IPOS Cuk Converter Power Density

In contrast, the output power density characterizes the degree of compactness of the used converter. The power density of a converter is expressed as a function of the output power of the converter divided by the volume of the converter. In isolated converters, the main concern is about the volume of the HFT used in the converter. Furthermore, based on [94], the power density can be calculated using (5.12):

$$\rho = \frac{P_{out}}{Volume} \tag{5.12}$$

The volume of the semiconductor switches, heat sinks, passive elements, and HFT used gives the volume of the high power converter. The volume of the IGBT depends on the IGBT module volume $\left(Vol_{igbtMod}\right)$And the number of IGBT switches used in the topology(n_{Tsw}). Where the volume of the switches can be written as follow:

$$Vol_{switches} = n_{Tsw}\,.Vol_{igbtMod}$$

For the transformer volume calculations, a single-phase transformer is used. The main parameters that specify the transformer volume are the core volume (Vol_{core}) and winding volume $\left(Vol_{winding}\right)$, where they can be calculated based on some recommendations specified in [94].

To calculate the total volume of the converter, a high-frequency power transformer of (HiMAG) brand with a rated power of 100kW and switching frequency less than 50kHz has been considered. In addition, ABB power switches are used with a rated voltage of 1.2kV to 6.5kV and a rated current of 700A. Moreover, a Hammond inductor with power capacitor volume is considered, and a factor of 1.2 is multiplied with the total volume to consider heat sinks size. Thus, the total volume is:

$$Vol_{total} = \left(Vol_{IGBT} + Vol_{trans} + V_{passive\ elemnts}\right) * 1.2$$

$$V_{total} = (0.16 + 2 + 3.6) * 1.2 = 5.86\ L$$

Considering converter losses presented earlier and the large volume elements such as HFT, power switches, heat sinks, and passive elements, the power density of the IPOS three Cuk converters is obtained using (5.12). It can be seen that the proposed IPOS system achieves high efficiency with high power density. The system has an efficiency of 97% with a power density of $6.6kW/L$, which satisfies the high-power requirement of the FCEV power conditioning unit.

5.6 Input Current Ripple Content Effect on FC

The selection of the Cuk converter was made due to the advantage of having a low current ripple, which is considered one of the essential indices in FC applications. The FC produces low voltage with a high current where the current ripples are considered a crucial factor affecting the FC life span [95]. The input current ripple of the proposed system depends on the input voltage V_{in}, duty cycle D, switching frequency f, and inductance L_1 as expressed in (5.13), as well as the rms value of the ripple current can be obtained using the current peak I_p value as shown in (5.15):

$$\Delta i_{L1} = \frac{V_{in}\, D}{L_1 f} \tag{5.13}$$

$$\Delta i_L = \frac{i_{fc,ripple(p-p)}}{I_{fc}}.100\% \tag{5.14}$$

$$i_{ripple\; rms} = \frac{I_p}{\sqrt{3}} \tag{5.15}$$

In multimodule switching converters where the power supply and load are shared, the feature of current ripple cancelation is enabled [96]. This distributes the processed power equally between the modules, where it helps in performing ripple minimization. Reducing the ripples leads to minimizing the size of converter inductance and capacitance cost. Since the proposed system is considered as a symmetric multimodule system where the input-current is the sum of the three converters input currents, the current ripple minimization can be achieved by phase-shifting the switching function of each converter by an angle determined by [97]:

$$\phi_n = (n-1).\frac{360^o}{N} \tag{5.15}$$

Where N is the total number of phases and n is the module number. Knowing that when the number of modules increases, the reduction of the ripple content increases, which helps to minimize the LC filer requirement.

Such topology helps to optimize the size and cost, and as the number of modules increases, the ripple content is decreased significantly where the FC can operate as a smooth DC current source without ripples.

Equations (5.13) and (5.15) are used to elucidate the effect of changing switching frequency on the inductance size, therefore the ripple current rms. Also, the transient model is used to calculate the FC ripple current. Figure 58 shows the FC current with 0.1% ripples, and Figure 59 shows the ripple current rms value with different values of the input inductor.

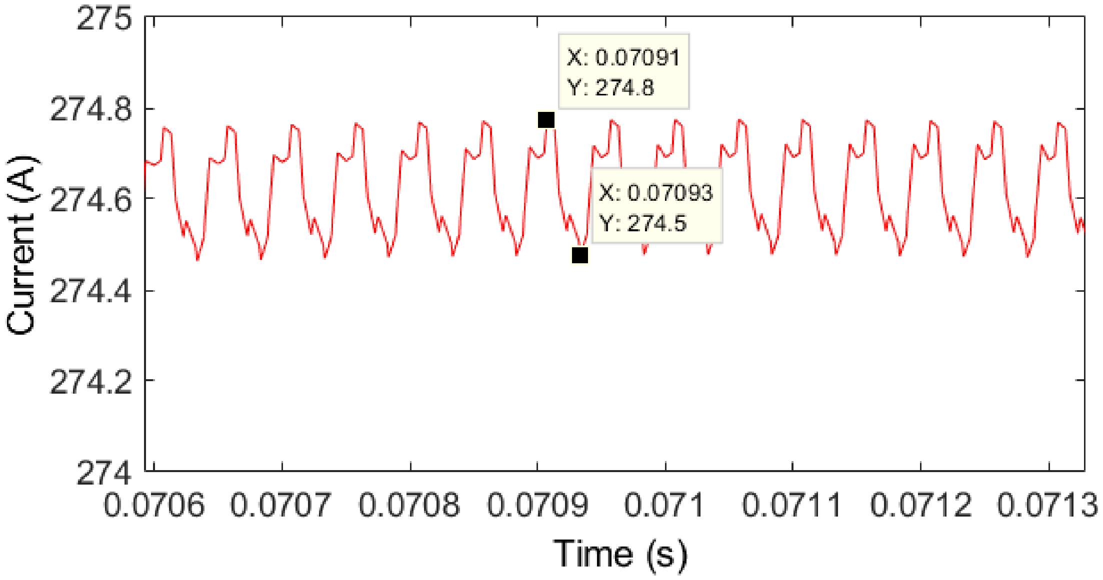

Figure 58: FC ripple current considering 120^o shift between the converters carriers

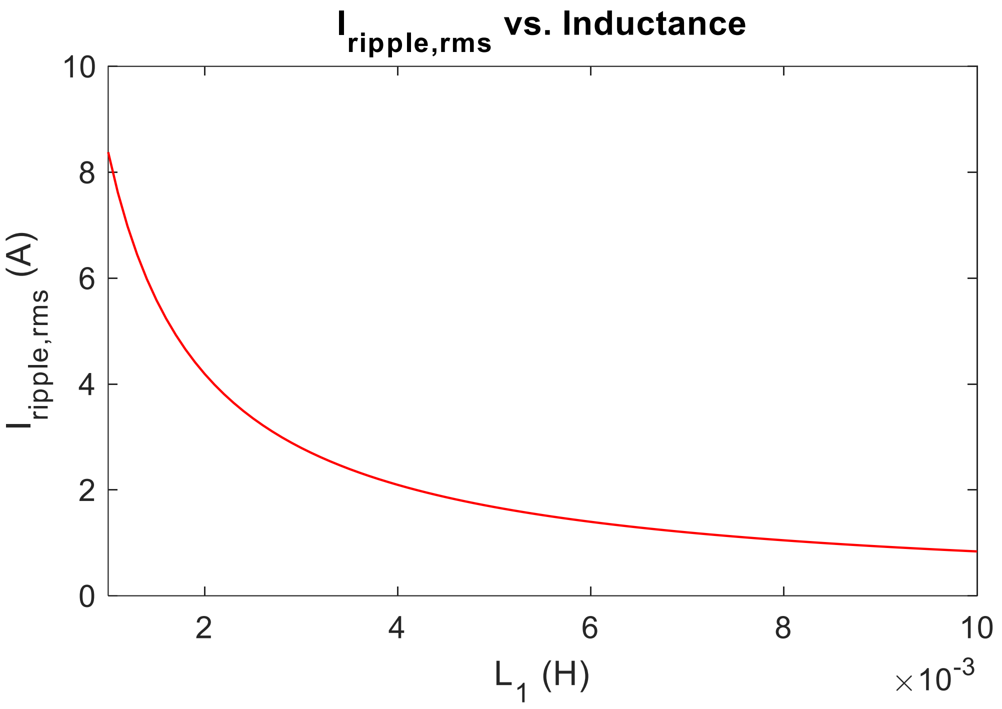

Figure 59: $I_{ripple,rms}$ Vs input inductance considring 120^o shift between the converters carriers

Chapter 6: Conclusion and Future Work

6.1 Conclusion

Highly efficient converters with high gain are considered an essential aspect of FCEV. This work has presented a modular topology that assures high gain and high efficiency for the overall power conditioning unit. To achieve such requirements, IPOS Cuk converters were used, the detailed theoretical model of the converter was derived considering parasitic elements to understand system behavior. An averaged mathematical model of the Cuk converter was obtained using state-space modeling. The obtained model was used to design system control, where all the designed controllers were obtained and tested through Matlab\Simulink. Furthermore, to enhance the overall system behavior and avoid the drawbacks of the conventional PI controller, a FOPI controller was introduced to the system to make the overall system robust against the plant variations. The overall system showed a faster response and less noise with the FOPI controller. Moreover, the digital control of the overall system was done on the derived model. An approximation method was used to convert the fractional-order system to an integer-order system to emulate the behavior of the fractional system. The approximated model and the conventional controllers were discretized and compared with each other. Afterward, the overall system was verified through simulation using MATLAB/Simulink. The overall system was examined using the IPOS converters integrated with MPPT and constant current controller to assure continuous power flow to charge the battery. The overall system extracted the maximum power of the FC, and equal power-sharing was ensured by achieving ICS and OVS between the converters through the controller. Moreover, the system's modularity was tested by eliminating one of the converters, the other two converters shared the load, and equal power-sharing was achieved successfully. Finally, the system was evaluated using different performance indices such as system efficiency, gain, sensitivity analysis, power density, and input current ripple content. The theoretical efficiency for the given high power system and was found to be greater than 95%. Moreover, the sensitivity analysis showed the effect of the parasitic resistances of the inductors r_L. It was found that the input inductors' resistance significantly affects the overall system gain than the output inductor. Also, it was found that higher sensitivities occur at higher duty cycles. The advantage of utilizing multimodule in decreasing the FC current ripples is discussed, showing some methods that could help in further reduction in the ripple content.

6.2 Future Work

The work in this thesis can be verified and tested practically using a scaled-down system. Several techniques can be integrated to increase system efficiency. For instance, implementing soft-switching techniques to reduce switching losses by investigating other topologies assures ZVS and ZCS compared to hard-switching and its associated losses. In addition, designing an overall energy management system could enhance the system and reduce the hydrogen fuel consumption by coordinating the battery charging by analyzing the battery's state of charge (SOC) and using the power produced by regenerative braking from the drive train. Furthermore, FOPI controller response can be enhanced by having proper gain tuning. Using optimization algorithms such as neural networks or genetic algorithms, optimum gains for FOPI can be obtained by defining system constraints such as corner frequency, allowable phase margin, and gain margin.

References

[1] A. Khaligh and Z. Li, “Battery, ultracapacitor, fuel cell, and hybrid energy storage systems for electric, hybrid electric, fuel cell, and plug-in hybrid electric vehicles: State of the art,” *IEEE Trans. Veh. Technol.*, vol. 59, no. 6, pp. 2806–2814, 2010, doi: 10.1109/TVT.2010.2047877.

[2] C. C. Chan, “The state of the art of electric, hybrid, and fuel cell vehicles,” *Proc. IEEE*, vol. 95, no. 4, pp. 704–718, 2007, doi: 10.1109/JPROC.2007.892489.

[3] M. Zandi, A. Payman, J. P. Martin, S. Pierfederici, B. Davat, and F. Meibody-Tabar, “Energy management of a fuel cell/supercapacitor/battery power source for electric vehicular applications,” *IEEE Trans. Veh. Technol.*, vol. 60, no. 2, pp. 433–443, 2011, doi: 10.1109/TVT.2010.2091433.

[4] “NASA - Cool Fuel Cells.” [Online]. Available: https://www.nasa.gov/vision/earth/technologies/18mar_fuelcell.html. [Accessed: 26-Sep-2021].

[5] Advanced Energy Economy, “Global and U.S. Markets By Revenue 2011-20 and Key Trends in Advanced Energy Growth,” 2021.

[6] B. Tanç, H. T. Arat, E. Baltacıoğlu, and K. Aydın, “Overview of the next quarter century vision of hydrogen fuel cell electric vehicles,” *Int. J. Hydrogen Energy*, vol. 44, no. 20, pp. 10120–10128, 2019, doi: 10.1016/j.ijhydene.2018.10.112.

[7] Y. Manoharan *et al.*, “Hydrogen fuel cell vehicles; Current status and future prospect,” *Appl. Sci.*, vol. 9, no. 11, 2019, doi: 10.3390/app9112296.

[8] “Cleaner urban transport with hydrogen buses | Horizon 2020.” [Online]. Available: https://ec.europa.eu/programmes/horizon2020/en/node/2574. [Accessed: 06-Oct-2021].

[9] “Global EV Outlook 2020 – Analysis - IEA.” [Online]. Available:

https://www.iea.org/reports/global-ev-outlook-2020. [Accessed: 27-Sep-2021].

[10] A. F. Burke, “Batteries and ultracapacitors for electric, hybrid, and fuel cell vehicles,” *Proc. IEEE*, vol. 95, no. 4, pp. 806–820, 2007, doi: 10.1109/JPROC.2007.892490.

[11] C. C. Chan, A. Bouscayrol, and K. Chen, “Electric, hybrid, and fuel-cell vehicles: Architectures and modeling,” *IEEE Trans. Veh. Technol.*, vol. 59, no. 2, pp. 589–598, 2010, doi: 10.1109/TVT.2009.2033605.

[12] “H2-Stations - H2Stations.org.” [Online]. Available: https://www.h2stations.org/. [Accessed: 26-Sep-2021].

[13] P. R. Pathapati, X. Xue, and J. Tang, “A new dynamic model for predicting transient phenomena in a PEM fuel cell system,” *Renew. Energy*, vol. 30, no. 1, pp. 1–22, 2005, doi: 10.1016/j.renene.2004.05.001.

[14] N. Marx, L. Boulon, F. Gustin, D. Hissel, and K. Agbossou, “A review of multi-stack and modular fuel cell systems: Interests, application areas and on-going research activities,” *International Journal of Hydrogen Energy*, vol. 39, no. 23. Elsevier Ltd, pp. 12101–12111, 04-Aug-2014, doi: 10.1016/j.ijhydene.2014.05.187.

[15] B. C. Brusso, “Electrochemistry and the development of the hydrogen fuel cell [history],” *IEEE Ind. Appl. Mag.*, vol. 27, no. 5, pp. 8–13, 2021, doi: 10.1109/MIAS.2021.3086965.

[16] N. Marx, D. Hissel, F. Gustin, L. Boulon, and K. Agbossou, “On the sizing and energy management of an hybrid multistack fuel cell – Battery system for automotive applications,” *Int. J. Hydrogen Energy*, vol. 42, no. 2, pp. 1518–1526, 2017, doi: 10.1016/j.ijhydene.2016.06.111.

[17] D. Candusso *et al.*, “Fuel cell operation under degraded working modes and study

of diode by-pass circuit dedicated to multi-stack association," *Energy Convers. Manag.*, vol. 49, no. 4, pp. 880–895, Apr. 2008, doi: 10.1016/j.enconman.2007.10.007.

[18] S. Mekhilef, R. Saidur, and A. Safari, "Comparative study of different fuel cell technologies," *Renew. Sustain. Energy Rev.*, vol. 16, no. 1, pp. 981–989, 2012, doi: 10.1016/j.rser.2011.09.020.

[19] J. T. Hawke, H. S. Krishnamoorthy, and P. N. Enjeti, "A family of new multiport power-sharing converter topologies for large grid-connected fuel cells," *IEEE J. Emerg. Sel. Top. Power Electron.*, vol. 2, no. 4, pp. 962–971, 2014, doi: 10.1109/JESTPE.2014.2348566.

[20] M. Abu Mallouh, E. Abdelhafez, M. Salah, M. Hamdan, B. Surgenor, and M. Youssef, "Model development and analysis of a mid-sized hybrid fuel cell/battery vehicle with a representative driving cycle," *J. Power Sources*, vol. 260, pp. 62–71, 2014, doi: 10.1016/j.jpowsour.2014.02.104.

[21] K. Ettihir, L. Boulon, and K. Agbossou, "Energy management strategy for a fuel cell hybrid vehicle based on maximum efficiency and maximum power identification," *IET Electr. Syst. Transp.*, vol. 6, no. 4, pp. 261–268, 2016, doi: 10.1049/iet-est.2015.0023.

[22] A. Emadi, K. Rajashekara, S. S. Williamson, and S. M. Lukic, "Topological overview of hybrid electric and fuel cell vehicular power system architectures and configurations," *IEEE Trans. Veh. Technol.*, vol. 54, no. 3, pp. 763–770, 2005, doi: 10.1109/TVT.2005.847445.

[23] A. Kolli, A. Gaillard, A. De Bernardinis, O. Bethoux, D. Hissel, and Z. Khatir, "A review on DC/DC converter architectures for power fuel cell applications," *Energy Convers. Manag.*, vol. 105, pp. 716–730, 2015, doi:

10.1016/j.enconman.2015.07.060.

[24] H. Wang, A. Gaillard, and D. Hissel, “A review of DC/DC converter-based electrochemical impedance spectroscopy for fuel cell electric vehicles,” *Renew. Energy*, vol. 141, pp. 124–138, 2019, doi: 10.1016/j.renene.2019.03.130.

[25] F. L. Tofoli, D. de C. Pereira, W. J. de Paula, and D. de S. Oliveira Júnior, “Survey on non-isolated high-voltage step-up dc-dc topologies based on the boost converter,” *IET Power Electron.*, vol. 8, no. 10, pp. 2044–2057, 2015, doi: 10.1049/iet-pel.2014.0605.

[26] B. W. Williams, “DC-to-DC converters with continuous input and output power,” *IEEE Trans. Power Electron.*, vol. 28, no. 5, pp. 2307–2316, 2013, doi: 10.1109/TPEL.2012.2213272.

[27] H. C. Liu and F. Li, “Novel High Step-Up DC-DC Converter with an Active Coupled-Inductor Network for a Sustainable Energy System,” *IEEE Trans. Power Electron.*, vol. 30, no. 12, pp. 6476–6482, 2015, doi: 10.1109/TPEL.2015.2429651.

[28] H. N. Tran, T.-T. Le, H. Jeong, S. Kim, and S. G. Choi, “A 300kHz, 63kW/L ZVT DC-DC Converter for 800V Fuel Cell Electric Vehicles,” *IEEE Trans. Power Electron.*, vol. 8993, no. c, pp. 1–1, 2021, doi: 10.1109/tpel.2021.3108815.

[29] B. Li, P. Wang, Z. Wang, X. Ma, and H. Bi, “A New Coupled-Inductor-Based High-Gain Interleaved DC-DC Converter with Sustained Soft Switching,” *IEEE Trans. Veh. Technol.*, vol. 70, no. 7, pp. 6527–6541, 2021, doi: 10.1109/TVT.2021.3083317.

[30] X. Hu, J. Wang, L. Li, and Y. Li, “A Three-Winding Coupled-Inductor DC-DC Converter Topology with High Voltage Gain and Reduced Switch Stress,” *IEEE Trans. Power Electron.*, vol. 33, no. 2, pp. 1453–1462, 2018, doi:

10.1109/TPEL.2017.2689806.

[31] X. Hu and C. Gong, “A high voltage gain DC-DC converter integrating coupled-inductor and diode-capacitor techniques,” *IEEE Trans. Power Electron.*, vol. 29, no. 2, pp. 789–800, 2014, doi: 10.1109/TPEL.2013.2257870.

[32] J. C. Wu, K. Der Wu, H. L. Jou, Z. H. Wu, and S. K. Chang, “Novel power electronic interface for grid-connected fuel cell power generation system,” *Energy Convers. Manag.*, vol. 71, pp. 227–234, 2013, doi: 10.1016/j.enconman.2013.03.038.

[33] K. C. Tseng and C. C. Huang, “High step-up high-efficiency interleaved converter with voltage multiplier module for renewable energy system,” *IEEE Trans. Ind. Electron.*, vol. 61, no. 3, pp. 1311–1319, 2014, doi: 10.1109/TIE.2013.2261036.

[34] M. Sagar Bhaskar *et al.*, “Survey of DC-DC Non-Isolated Topologies for Unidirectional Power Flow in Fuel Cell Vehicles,” *IEEE Access*, vol. 8, pp. 178130–178166, 2020, doi: 10.1109/access.2020.3027041.

[35] F. Mumtaz, N. Zaihar Yahaya, S. Tanzim Meraj, B. Singh, R. Kannan, and O. Ibrahim, “Review on non-isolated DC-DC converters and their control techniques for renewable energy applications,” *Ain Shams Eng. J.*, no. xxxx, 2021, doi: 10.1016/j.asej.2021.03.022.

[36] Y. Zhang *et al.*, “Wide Input-Voltage Range Boost Three-Level DC-DC Converter with Quasi-Z Source for Fuel Cell Vehicles,” *IEEE Trans. Power Electron.*, vol. 32, no. 9, pp. 6728–6738, 2017, doi: 10.1109/TPEL.2016.2625327.

[37] Y. Park, B. Jung, and S. Choi, “Nonisolated ZVZCS resonant PWM dc-dc converter for high step-up and high-power applications,” *IEEE Trans. Power Electron.*, vol. 27, no. 8, pp. 3568–3575, 2012, doi:

10.1109/TPEL.2012.2187342.

[38] A. Varshney, R. Kumar, D. Kuanr, and M. Gupta, “Soft-Switched Boost DC-DC Converter System for Electric Vehicles using An Auxiliary Resonant Circuit,” *Int. J. Emerg. Technol. Adv. Eng.*, vol. 4, no. 3, 2014.

[39] M. Delshad and N. rakian, “A New ZCS High Step-up DC-DC Converter,” *Int. Trans. Electr. Comput. Eng. Syst.*, vol. 1, no. 1, pp. 1–5, 2013, doi: 10.12691/ITECES-1-1-1.

[40] A. Bhattacharjee, S. Saha, D. Elangovan, and G. Arunkumar, “Design of Circuit for Battery Charging of Electric Vehicles,” *2017 Int. Conf. Energy, Commun. Data Anal. Soft Comput.*, pp. 330–337, 2017.

[41] M. ElMenshawy and A. Massoud, “Modular Isolated DC-DC Converters for Ultra-Fast EV Chargers: A Generalized Modeling and Control Approach,” *Energies*, vol. 13, no. 10, p. 2540, May 2020, doi: 10.3390/en13102540.

[42] R. Pittini, Z. Zhang, and M. A. E. Andersen, “Isolated full bridge boost DC-DC converter designed for bidirectional operation of fuel cells/electrolyzer cells in grid-tie applications,” *2013 15th Eur. Conf. Power Electron. Appl. EPE 2013*, 2013, doi: 10.1109/EPE.2013.6634433.

[43] U. R. Prasanna, A. K. Rathore, and S. K. Mazumder, “Novel zero-current-switching current-fed half-bridge isolated DC/DC converter for fuel-cell-based applications,” *IEEE Trans. Ind. Appl.*, vol. 49, no. 4, pp. 1658–1668, 2013, doi: 10.1109/TIA.2013.2257980.

[44] A. K. Rathore and U. R. Prasanna, “Analysis, design, and experimental results of novel snubberless bidirectional naturally clamped ZCS/ZVS current-fed half-bridge DC/DC converter for fuel cell vehicles,” *IEEE Trans. Ind. Electron.*, vol. 60, no. 10, pp. 4482–4491, 2013, doi: 10.1109/TIE.2012.2213563.

[45] D. D. Tran, H. N. Vu, S. Yu, and W. Choi, “A Novel Soft-Switching Full-Bridge Converter with a Combination of a Secondary Switch and a Nondissipative Snubber,” *IEEE Trans. Power Electron.*, vol. 33, no. 2, pp. 1440–1452, 2018, doi: 10.1109/TPEL.2017.2688580.

[46] U. R. Prasanna and A. K. Rathore, “Extended range ZVS active-clamped current-fed full-bridge isolated DC/DC converter for fuel cell applications: Analysis, design, and experimental results,” *IEEE Trans. Ind. Electron.*, vol. 60, no. 7, pp. 2661–2672, 2013, doi: 10.1109/TIE.2012.2194977.

[47] D. Tran, N. Vu, and W. Choi, “A Quasi-resonant ZVZCS phase-shifted full-bridge converter with an active clamp in the secondary side,” *Energies*, vol. 11, no. 11, pp. 1–21, 2018, doi: 10.3390/en11112868.

[48] J. Zhu, Q. Qian, S. Lu, and W. Sun, “Phase-Shift Triple Full-Bridge ZVZCS Converter with All Soft Switched Devices,” *J. POWER Electron.*, vol. 19, no. 6, pp. 1337–1350, 2019.

[49] L. C. Shih, Y. H. Liu, and H. J. Chiu, “A Novel Hybrid Mode Control for a Phase-Shift Full-Bridge Converter Featuring High Efficiency over a Full-Load Range,” *IEEE Trans. Power Electron.*, vol. 34, no. 3, pp. 2794–2804, Mar. 2019, doi: 10.1109/TPEL.2018.2838572.

[50] B. Bryant and M. K. Kazimierczuk, “Derivation of the Ćuk PWM DC-DC converter circuit topology,” *Proc. - IEEE Int. Symp. Circuits Syst.*, vol. 3, pp. 292–295, 2003, doi: 10.1109/iscas.2003.1205013.

[51] B. Bryant and M. K. Kazimierczuk, “Derivation of the Ćuk PWM DC-DC converter circuit topology,” *Proc. - IEEE Int. Symp. Circuits Syst.*, vol. 3, pp. 6–9, 2003, doi: 10.1109/iscas.2003.1205013.

[52] M. S. Bhaskar, S. Padmanaban, and F. Blaabjerg, “A multistage DC-DC step-up

self-balanced and magnetic component-free converter for photovoltaic applications: Hardware implementation," *Energies*, vol. 10, no. 5, 2017, doi: 10.3390/en10050719.

[53] C. Li *et al.*, "Design and implementation of a bidirectional isolated Ćuk converter for low-voltage and high-current automotive DC source applications," *IEEE Trans. Veh. Technol.*, vol. 63, no. 6, pp. 2567–2577, 2014, doi: 10.1109/TVT.2013.2294599.

[54] R. Pandey and B. Singh, "A Power-Factor-Corrected LLC Resonant Converter for Electric Vehicle Charger Using Cuk Converter," *IEEE Trans. Ind. Appl.*, vol. 55, no. 6, pp. 6278–6286, 2019, doi: 10.1109/TIA.2019.2934059.

[55] F. Evran and M. T. Aydemir, "Isolated high step-Up DC-DC converter with low voltage stress," *IEEE Trans. Power Electron.*, vol. 29, no. 7, pp. 3591–3603, 2014, doi: 10.1109/TPEL.2013.2282813.

[56] W. Chen, X. Ruan, H. Yan, and C. K. Tse, "DC/DC conversion systems consisting of multiple converter modules: Stability, control, and experimental verifications," *IEEE Trans. Power Electron.*, vol. 24, no. 6, pp. 1463–1474, 2009, doi: 10.1109/TPEL.2009.2012406.

[57] D. Sha, Y. Xu, J. Zhang, and Y. Yan, "Current-Fed Hybrid Dual Active Bridge DC-DC Converter for a Fuel Cell Power Conditioning System With Reduced Input Current Ripple," *IEEE Trans. Ind. Electron.*, vol. 64, no. 8, pp. 6628–6638, 2017, doi: 10.1109/TIE.2017.2698376.

[58] G. Xu, D. Sha, Y. Xu, and X. Liao, "Dual-Transformer-Based DAB Converter with Wide ZVS Range for Wide Voltage Conversion Gain Application," *IEEE Trans. Ind. Electron.*, vol. 65, no. 4, pp. 3306–3316, 2018, doi: 10.1109/TIE.2017.2756601.

[59] J. A. Ferreira, "The multilevel modular DC converter," *IEEE Trans. Power Electron.*, vol. 28, no. 10, pp. 4460–4465, 2013, doi: 10.1109/TPEL.2012.2237413.

[60] G. J. Kish, "On the emerging class of non-isolated modular multilevel DC-DC converters for DC and hybrid AC-DC systems," *IEEE Trans. Smart Grid*, vol. 10, no. 2, pp. 1762–1771, 2019, doi: 10.1109/TSG.2017.2777473.

[61] S. Debnath, J. Qin, B. Bahrani, M. Saeedifard, and P. Barbosa, "Operation, control, and applications of the modular multilevel converter: A review," *IEEE Trans. Power Electron.*, vol. 30, no. 1, pp. 37–53, 2015, doi: 10.1109/TPEL.2014.2309937.

[62] S. P. Engel, M. Stieneker, N. Soltau, S. Rabiee, H. Stagge, and R. W. De Doncker, "Comparison of the modular multilevel DC converter and the dual-active bridge converter for power conversion in HVDC and MVDC grids," *IEEE Trans. Power Electron.*, vol. 30, no. 1, pp. 124–137, 2015, doi: 10.1109/TPEL.2014.2310656.

[63] J. Yang, Z. He, H. Pang, and G. Tang, "The hybrid-cascaded DC-DC converters suitable for HVdc applications," *IEEE Trans. Power Electron.*, vol. 30, no. 10, pp. 5358–5363, 2015, doi: 10.1109/TPEL.2015.2420666.

[64] V. Karthikeyan and R. Gupta, "Distributed power flow control using cascaded multilevel isolated bidirectional DC–DC converter with multi-phase shift modulation," *IET Power Electron.*, vol. 12, no. 11, pp. 2996–3003, 2019, doi: 10.1049/iet-pel.2019.0077.

[65] X. Sha, D.; Guo, Z.; Luo, T.; Liao, "A General Control Strategy for Input-Series-Output-Series Modular DC-DC Converters," *IEEE Trans. Power Electron.*, vol. 29, no. 7, pp. 3766–3775, 2014.

[66] J. Cheng, J. Shi, and X. He, "A novel input-parallel output-parallel connected DC-

DC converter modules with automatic sharing of currents," *Conf. Proc. - 2012 IEEE 7th Int. Power Electron. Motion Control Conf. - ECCE Asia, IPEMC 2012*, vol. 3, pp. 1871–1876, 2012, doi: 10.1109/IPEMC.2012.6259123.

[67] Y. Lian, G. Adam, D. Holliday, and S. Finney, "Modular input-parallel output-series DC/DC converter control with fault detection and redundancy," *IET Gener. Transm. Distrib.*, vol. 10, no. 6, pp. 1361–1369, Apr. 2016, doi: 10.1049/iet-gtd.2015.0789.

[68] S. Chakraborty, H. N. Vu, M. M. Hasan, D. D. Tran, M. El Baghdadi, and O. Hegazy, "DC-DC converter topologies for electric vehicles, plug-in hybrid electric vehicles and fast charging stations: State of the art and future trends," *Energies*, vol. 12, no. 8, 2019, doi: 10.3390/en12081569.

[69] A. Alassi. and A. Massoud, "Modelling Of DC-DC Converters with Continuous Input Current For High Power PV Applications," *2016 IEEE Symp. Comput. Appl. Ind. Electron.*, pp. 171–176, 2016.

[70] S. Tiwari, Z. Rayeen, and O. Hanif, "Design and Analysis of Fractional Order PID Controller tuning via Genetic Algorithm for CUK Converter," *2018 13th Int. Conf. Ind. Inf. Syst. ICIIS 2018 - Proc.*, no. 978, pp. 436–441, 2018, doi: 10.1109/ICIINFS.2018.8721419.

[71] L. Kathi, A. Ayachit, D. K. Saini, A. Chadha, and M. K. Kazimierczuk, "Open-loop small-signal modeling of cuk DC-DC converter in CCM by circuit-averaging technique," *2018 IEEE Texas Power Energy Conf. TPEC 2018*, vol. 2018-Febru, pp. 1–6, 2018, doi: 10.1109/TPEC.2018.8312045.

[72] F. Haugen, "Comparing PI tuning methods in a real benchmark temperature control system," *Model. Identif. Control*, vol. 31, no. 3, pp. 79–91, 2010, doi: 10.4173/mic.2010.3.1.

[73] H. S. Khaldi and A. C. Ammari, “Fractional-order control of three level boost DC/DC converter used in hybrid energy storage system for electric vehicles,” *2015 6th Int. Renew. Energy Congr. IREC 2015*, 2015, doi: 10.1109/IREC.2015.7110930.

[74] C. Jung, “Power Up with 800-V Systems,” *IEEE Electrif. Mag.*, no. March, pp. 53–58, 2017.

[75] A. G. Soriano-sánchez, M. A. Rodríguez-licea, and F. J. Pérez-pinal, “Fractional-Order Approximation and Synthesis of a PID Controller for a Buck Converter,” pp. 1–17, 2020, doi: 10.3390/en13030629.

[76] R. El-khazali, “Fractional-order PI λ D μ controller design,” *Comput. Math. with Appl.*, vol. 66, no. 5, pp. 639–646, 2013, doi: 10.1016/j.camwa.2013.02.015.

[77] P. Warrier and P. Shah, “Fractional Order Control of Power Electronic Converters in Industrial Drives and Renewable Energy Systems: A Review,” *IEEE Access*, vol. 9, pp. 58982–59009, 2021, doi: 10.1109/ACCESS.2021.3073033.

[78] Z. Qi, J. Tang, J. Pei, and L. Shan, “Fractional Controller Design of a DC-DC Converter for PEMFC,” *IEEE Access*, vol. 8, pp. 120134–120144, 2020, doi: 10.1109/ACCESS.2020.3005439.

[79] N. Ullah, F. Nisar, and A. A. Alahmadi, “Closed Loop Control of Photo Voltaic Emulator Using Fractional Calculus,” *IEEE Access*, vol. 8, pp. 28880–28887, 2020, doi: 10.1109/ACCESS.2020.2971676.

[80] A. Tepljakov, E. Petlenkov, and J. Belikov, “Closed-loop identification of fractional-order models using FOMCON toolbox for MATLAB,” *Proc. Bienn. Balt. Electron. Conf. BEC*, vol. 2015-Novem, pp. 213–216, 2014, doi: 10.1109/BEC.2014.7320594.

[81] R. El-Khazali, I. M. Batiha, and S. Momani, “Approximation of Fractional-Order

Operators," *Springer Proc. Math. Stat.*, vol. 303, pp. 121–151, Jul. 2018, doi: 10.1007/978-981-15-0430-3_8.

[82] B. Vinagre, I. Podlubny, A. Hernandez, and V. Feliu, "Some approximations of fractional order operators used in control theory and applications," *Fract. Calc. Appl. Anal.*, vol. 3, no. 3, pp. 231–248, 2000.

[83] A. Oustaloup, F. Levron, B. Mathieu, and F. M. Nanot, "Frequency-band complex noninteger differentiator: Characterization and synthesis," *IEEE Trans. Circuits Syst. I Fundam. Theory Appl.*, vol. 47, no. 1, pp. 25–39, 2000, doi: 10.1109/81.817385.

[84] A. Yüce, F. N. Deniz, and N. Tan, "A New Integer Order Approximation Table for Fractional Order Derivative Operators," *IFAC-PapersOnLine*, vol. 50, no. 1, pp. 9736–9741, 2017, doi: 10.1016/j.ifacol.2017.08.2177.

[85] R. El-Khazali, "On the biquadratic approximation of fractional-order Laplacian operators," *Analog Integr. Circuits Signal Process.*, vol. 82, no. 3, pp. 503–517, 2015, doi: 10.1007/s10470-014-0432-8.

[86] K. J. Runtz and M. D. Lyster, "Fuel cell equivalent circuit models for passive mode testing and dynamic mode design," *Can. Conf. Electr. Comput. Eng.*, vol. 2005, no. May, pp. 794–797, 2005, doi: 10.1109/CCECE.2005.1557048.

[87] A. M. Dhirde, N. V. Dale, H. Salehfar, M. D. Mann, and T. H. Han, "Equivalent electric circuit modeling and performance analysis of a PEM fuel cell stack using impedance spectroscopy," *IEEE Trans. Energy Convers.*, vol. 25, no. 3, pp. 778–786, 2010, doi: 10.1109/TEC.2010.2049267.

[88] S. C. Page, A. H. Anbuky, S. P. Krumdieck, and J. Brouwer, "Test method and equivalent circuit modeling of a PEM fuel cell in a passive state," *IEEE Trans. Energy Convers.*, vol. 22, no. 3, pp. 764–773, 2007, doi:

10.1109/TEC.2007.895857.

[89] B. Somaiah and V. Agarwal, “Distributed Maximum Power Extraction From Fuel Cell Stack Arrays Using Dedicated Power Converters in Series and Parallel Configuration,” *IEEE Trans. Power Electron.*, vol. 31, no. 4, pp. 1442–1451, 2016.

[90] B. Somaiah and V. Agarwal, “Recursive estimation-based maximum power extraction technique for a fuel cell power source used in vehicular applications,” *IEEE Trans. Power Electron.*, vol. 28, no. 10, pp. 4636–4643, 2013, doi: 10.1109/TPEL.2012.2236688.

[91] T. Esram and P. L. Chapman, “Comparison of photovoltaic array maximum power point tracking techniques,” *IEEE Trans. Energy Convers.*, vol. 22, no. 2, pp. 439–449, 2007, doi: 10.1109/TEC.2006.874230.

[92] N. Denniston, A. M. Massoud, S. Ahmed, and P. N. Enjeti, “Multiple-module high-gain high-voltage DCDC transformers for offshore wind energy systems,” *IEEE Trans. Ind. Electron.*, vol. 58, no. 5, pp. 1877–1886, 2011, doi: 10.1109/TIE.2010.2053340.

[93] H. Hafezi and R. Faranda, “A new approach for power losses evaluation of IGBT/diode module,” *Electron.*, vol. 10, no. 3, pp. 1–21, 2021, doi: 10.3390/electronics10030280.

[94] R. Barrera-Cardenas and M. Molinas, “A simple procedure to evaluate the efficiency and power density of power conversion topologies for offshore wind turbines,” *Energy Procedia*, vol. 24, no. January, pp. 202–211, 2012, doi: 10.1016/j.egypro.2012.06.102.

[95] M. V. Naik and P. Samuel, “Analysis of ripple current, power losses and high efficiency of DC-DC converters for fuel cell power generating systems,” *Renew.*

Sustain. Energy Rev., vol. 59, pp. 1080–1088, 2016, doi: 10.1016/j.rser.2016.01.029.

[96] S. Baburajan, H. Wang, D. Kumar, Q. Wang, and F. Blaabjerg, “Dc-link current harmonic mitigation via phase-shifting of carrier waves in paralleled inverter systems,” *Energies*, vol. 14, no. 14, pp. 1–17, 2021, doi: 10.3390/en14144229.

[97] M. Schuck and R. C. N. Pilawa-Podgurski, “Ripple Minimization Through Harmonic Elimination in Asymmetric Interleaved Multiphase DC-DC Converters,” *IEEE Trans. Power Electron.*, vol. 30, no. 12, pp. 7202–7214, 2015, doi: 10.1109/TPEL.2015.2393812.

APPENDIX A: MATLAB CODE

```
Voltage:

Vi=430; Vo=360; d=Vo/(Vi+Vo); d1=1-d; L1=1000e-6;
L2=500e-6; C1=90e-6; C2=50e-6; rL1=0.0036;
rL2=0.0018; rc1=0.0035; rc2=0.0043; Ro=2.25; rD=0.05; rs=0.012;
RL=(Ro*rc2)/(Ro+rc2);
R11=(Ro)/(Ro+rc2);
A1 =[(-rs-rL1)/L1 -rs/L1 0 0;-rs/L2 -(rs+rc1+rL2+RL)/L2 1/L2 -R11/L2;
0 -1/C1 0 0;0 R11/C2 0 -1/((Ro+rc2)*(C2))];
A2 =[(-rL1-rc1-rD)/L1 -rD/L1 -1/L1 0;-rD/L2 -(rD+rL2+RL)/L2 0 -
R11/L2;1/C1 0 0 0;0 R11/C2 0 -1/((Ro+rc2)*(C2))];
B=[1/L1; 0; 0; 0];
C=[0 RL 0 R11];
A=(d*A1)+(d1*A2);
I=eye(4,4);
syms s
z= s*I-A;
zin=inv(z);
Ainv=inv(A);
x=-Ainv*B*Vi;
Bd=(A1-A2)*x;
G=C*zin*Bd;
Gs=simplify(G);
```

Current:

```
Vi=430; Vo=360;Io=111.1; Ro=2.25; d=Io/((Vi/Ro)+Io); d1=1-d;
L1=1000e-6;
L2=500e-6; C1=90e-6; C2=50e-6; rL1=0.0036;
rL2=0.0018; rc1=0.0035; rc2=0.0043; Ro=2.25; rD=0.05; rs=0.012;
RL=(Ro*rc2)/(Ro+rc2);
R11=(Ro)/(Ro+rc2);
A1 =[(-rs-rL1)/L1 -rs/L1 0 0;-rs/L2 -(rs+rc1+rL2+RL)/L2 1/L2 -R11/L2;
0 -1/C1 0 0;0 R11/C2 0 -1/((Ro+rc2)*(C2))];
A2 =[(-rL1-rc1-rD)/L1 -rD/L1 -1/L1 0;-rD/L2 -(rD+rL2+RL)/L2 0 -
R11/L2;1/C1 0 0 0;0 R11/C2 0 -1/((Ro+rc2)*(C2))];
B=[1/L1; 0; 0; 0];
C=[0 RL/Ro 0 R11/Ro];
A=(d*A1)+(d1*A2);
I=eye(4,4);
syms s
z= s*I-A;
zin=inv(z);
Ainv=inv(A);
x=-Ainv*B*Vi;
Bd=(A1-A2)*x;
G=C*zin*Bd;
Gs=simplify(G);
```

El khazali Approximation

```
% structures of order 2*n.
%
n=3;
w=1;
alf=0.2;
et=tan(alf*pi/4);
wc(1)=w;
```

```
ao=alf^alf+2*alf+1;
a2=alf^alf-2*alf+1;
a1=(a2-ao)*tan((2+alf)*pi/4);
if ( n > 1 )
% The solution of the following polynomial is used to generate
% a recursive formula to select the next center frequency for the
% next modular structure.
Y=roots([ao*a2*et a1*(a2-ao) (a1^2-a2^2-ao^2) a1*(a2-ao) ao*a2*et ]);
wx=(abs(max(Y)))
for k=2:n
wc(k)=(wx^(2*(k-1)))*wc(1)
end
% normalizing by the geometric mean;
wm=(prod(wc))^(1/n);
sysk=1;
for l=1:n;
N=[ao a1*wc(l)/wm a2*(wc(l)/wm)^2];
D=[a2 a1*wc(l)/wm ao*(wc(l)/wm)^2];
sysk=sysk*(tf(N,D));
end
[Numk,Denk]=tfdata(sysk);
else
Numk=[ao a1*w a2*w^2];
Denk=[a2 a1*w ao*w^2];
sysk=tf(Numk,Denk);
end
```

Sensitivity analysis Code

```
%%SA
syms u L1 L2 C1 C2 R Rc1 Rc2 RL1 RL2 Rd Rs Vs I1 I2 V1 V2 RL1pu RL2pu
A1 = [-(RL1+Rs)/L1 -Rs/L1 0 0;...
    -Rs/L2 -(Rc1+RL2+Rs+((Rc2*R)/(Rc2+R)))/L2 1/L2 ((Rc2/(Rc2+R))-
1)/L2;...
    0 -1/C1 0 0;...
    0 R/(R*C2+Rc2*C2) 0 -1/(C2*R+Rc2*C2)];
A2 = [(-RL1-Rd-Rc1)/L1 -Rd/L1 -1/L1 0;...
    -Rd/L2 -(RL2+Rd+((Rc2*R)/(Rc2+R)))/L2 0 ((Rc2/(Rc2+R))-1)/L2;...
    1/C1 0 0 0;...
    0 R/(R*C2+Rc2*C2) 0 -1/(C2*R+Rc2*C2)];
A = A1*u+A2*(1-u);
B = [1/L1;0;0;0];
C = [0 (R*Rc2)/(R+Rc2) 0 1-(Rc2/(Rc2+R))];
TR = -C*inv(A)*B;
TRS = subs(TR,[Rc1 Rc2 Rd Rs RL1 RL2],[0 0 0 0 R*RL1pu RL2pu*R]);
pretty(simplify(TRS))

%% For IPOS
GS = TRS+TRS+TRS;

SensR1S = (RL1pu/GS)*diff(GS,RL1pu);
pretty(simplify(SensR1S));
SensR2S = (RL2pu/GS)*diff(GS,RL2pu);
pretty(simplify(SensR2S));

%% Calculations:
rL1pu = 0.001; rL2pu = 0.001; D = 1;o=1;
ssw=[];
ssw2=[];
```

```
Dn=[];
b=1;
for w= 5:0.5:10
    b=1;
D = w*0.1;
Dn(o)=D;
% Series
BaseS1 = double(subs(SensR1S,[RL1pu RL2pu u],[rL1pu rL2pu D]));
BaseS2 = double(subs(SensR2S,[RL1pu RL2pu u],[rL1pu rL2pu D]));

for i = 1:0.5:20
    rL1puC(b) = rL1pu*(1+0.01*i);
     SSRL1(b) = double(subs(SensR1S,[RL1pu RL2pu u],[rL1puC(b) rL2pu
D])); %% Series RL1
    SSRL1R(b) = abs(SSRL1(b)-BaseS1)*100; %% Series RL1
    rL2puC(b) = rL2pu*(1+0.01*i);
     SSRL2(b) = double(subs(SensR2S,[RL1pu RL2pu u],[rL1pu rL2puC(b)
D])); %% Series RL2
    SSRL2R(b) = abs(SSRL2(b)-BaseS2)*100; %% Series RL2
    PChange(b) = i;
b=b+1;
end
ssw(o,:)=SSRL1R;
ssw2(o,:)=SSRL2R;
o=o+1;

end
```